Instrumentation and technical development for small animal micro-MRI studies at 7-Tesla

Minh Dung Hoang

Université Claude Bernard Lyon 1

Creatis LRMN

Instrumentation and technical development for small animal micro-MRI studies at 7-Tesla

Minh Dung HOANG

Directors: Dr. Latifa FAKRI-BOUCHET
Dr. Youssef ZAIM WADGHIRI

Bernard & Irene Schwartz Center for Biomedical Imaging
Department of Radiology
NEW YORK UNIVERSITY SCHOOL OF MEDICINE

Table of contents

Résumé

L'IRM offre de nombreux avantages qui en font un outil d'imagerie attractif en comparaison avec d'autres modalités d'imagerie préclinique complémentaires telles que l'imagerie optique, la micro-tomographie aux rayons X (µ-scanner ou µ-CT), la micro-Tomographie par Emission de Positons (µ-TEP), l'échographie ultrasonore ou la imagerie par photoluminescence et fluorescence. La nature tridimensionnelle de l'IRM sur une grande région d'intérêt en combinaison avec un contraste endogène tissulaire inégalé et qui est réalisable avec une résolution micrométrique en font un outil d'imagerie de haute importance en recherche biomédicale et plus particulièrement si l'on tient compte de la diversité des sources de contraste tissulaire possibles. Cependant, la principale limitation de l'IRM reste sa sensibilité relativement faible et sa productivité réduite à un seul examen à la fois.

L'objectif principal de ce travail de thèse a été le développement d'un ensemble de méthodologies en Imagerie par Résonance Magnétique (IRM), dédiées à des études sur des modèles expérimentaux.

Une grande partie de nos efforts a été consacrée aux travaux suivants:

- au développement et à l'optimisation d'instrumentations dédiées,
- à la mise en place de protocoles IRM efficaces,

L'ensemble de nos travaux a visé à surmonter tant les contraintes expérimentales rencontrées que celles liées a notre installation IRM. Particulièrement, l'amélioration d'images ex vivo et in vivo a été obtenu lors d'études précliniques utilisant des modèles animaux de la maladie d'Alzheimer.

Les résultats obtenus ont été atteints logiquement et progressivement à partir d'expérimentations ex vivo et in vivo. La première étape a été consacré à l'amélioration de la composante clé en amont de la chaîne d'acquisition: la sonde RMN, également appelée résonateur radiofréquence (RF).

Nous avons mené notre travail sur les trois aspects expérimentaux suivants:

- Conception et réalisation de sondes dédiées à l'imagerie in vivo de la souris tant pour l'étude du corps entier que pour l'IRM de la tête
- Développement et mise en œuvre de sondes et d'instrumentation permettant l'acquisition simultanée de plusieurs cerveaux de souris ex vivo afin d'augmenter la productivité et l'efficacité de notre scanner.
- Conception et réalisation d'un ensemble d'antennes spécialement adapté à l'imagerie directe de coupes de tissues histologiques de différentes tailles ainsi qu'a la mise au point des protocoles correspondants à la préparation des échantillons.

Dans le chapitre d'introduction (chapitre 1), nous décrivons l'ensemble des outils et protocoles de caractérisation des sondes RMN conçues et réalisées pour les besoins de nos études. Cette caractérisation systématique effectuée aussi pour les antennes RMN commerciales du laboratoire a permis d'établir une étude comparative de leurs performances.

Dans le chapitre 2, nous avons étudié des résonateurs RF homogènes avec une attention particulière pour les résonateurs de type cage d'oiseau. Après examen de leurs principaux avantages et des limites de chaque structure (passe-bas et passe-haut), nous détaillons les étapes pratiques nécessaires pour concevoir une antenne cage d'oiseau de type passe-haut dédiée à l'imagerie corps entier de souris. A titre d'exemple, nous présentons des séries d'images par IRM, illustrant l'excellente couverture RF et permettant l'identification (dans notre cas, de façon qualitative) des propriétés pharmacocinétiques d'agents de contraste nouvellement conçus.

Concernant, l'imagerie du cerveau de souris, notre objectif a été l'augmentation de la sensibilité de notre antenne en comparaison à une antenne commerciale en réduisant la structure géométrique afin de mieux confiner la sensibilité à la région d'intérêt. Ceci s'est traduit par une amélioration du facteur de remplissage permettant plus de 10% de gain en rapport signal-bruit (SNR) équivalent à une réduction de 20% du temps d'acquisition, sans pour détériorer l'homogénéité globale du champ RF couvrant la région du cerveau.

Le chapitre 3 met en valeur l'importance de l'IRM ex vivo, étape cruciale pour le test de nouveaux protocoles et le développement de séquences d'imagerie ainsi que pour

l'optimisation de leurs paramètres en vue de maximiser le signal et/ou le contraste. C'est aussi une importante étape d'aide à la validation des résultats de l'IRM in vivo en corrélation avec l'histologie pour compenser leur différence de résolution spatiale.

Cette dernière peut être améliorer par l'usage de l'IRM ex vivo en augmentant le nombre de répétitions de l'examen qui sont accumulées afin de compenser la perte de signal; ce qui a pour conséquence le rallongement de la durée d'acquisition. Ceci a eu pour conséquence pratique d'améliorer l'accès à l'IRM en mettant à profit les créneaux horaires "inutilisés" durant la nuit. Cette stratégie nous a mené à concevoir une structure d'antenne de volume plus grand pour permettre une couverture simultanée de plusieurs échantillons avec une sensibilité suffisante pour obtenir une résolution isotrope <100µm et une amélioration de la productivité.

La structure d'antenne proposée en association à un préamplificateur de faible figure de bruit dédiés pour l'IRM ex vivo ont permis une capacité d'acquisition simultanée de plus de huit cerveaux de souris fixés tout en offrant une excellente couverture RF homogène dans la région linéaire des bobines de gradients. La validation de l'ensemble de ces développements a été réalisée dans le cadre de la caractérisation d'agents de contraste nouvellement développés pour l'étude de la maladie d'Alzheimer.

Le chapitre 4 traite de la conception et la mise en œuvre d'un ensemble de structures originales d'antennes closes, adaptées à la forme planaire d'une coupe histologique tout en assurant le meilleur compromis entre l'homogénéité RF et le facteur de remplissage. Le gain résultant en sensibilité de ces structures a été évalué et comparé à celui d'une une antenne commerciale (tête de souris). Pour illustrer l'excellente corrélation obtenue entre les IRM ex vivo et les images histologiques, des exemples sont donnés à la fin de ce chapitre qui a fait l'objet d'une publication récente dans le journal "Magnetic Resonance in Medicine".

Abstract

The overarching goals of this work are to develop a set of magnetic resonance (MR) imaging methodologies to help study experimental models in the biomedical research. MRI offers a combination of attributes making it appealing as an imaging tool in biomedical research compared to other complementary preclinical imaging modalities such as optical imaging, micro-computed tomography, micro-Positron emission tomography or ultrasound bio-microscopy. The three-dimensional nature of MRI over a large region of interest and the unrivaled endogenous tissue contrast achievable in micrometric resolution make it a very important tool in biomedical research. This is particularly important with the expanding potentials of tissue contrast mechanism it can offer. However, one of the major limitations is its relative low sensitivity and slow throughput.

A large part of our efforts have been dedicated to improve the MRI instrumentation and protocols to overcome some of these limitations around the existing MRI scanner in order help better screen both in vivo and ex vivo transgenic mouse models, -the most studied animal model of human diseases. This was assessed in our work with a particular focus on experimental models of Alzheimer's disease.

The description of our work and results build logically and incrementally from in vivo to ex vivo experimental set up starting with tackling the improvement of the first component of the acquisition chain: the MRI probe, also termed radiofrequency (RF) resonator or coil. The scope of the work expands from probes enabling in vivo whole mouse body to head-only MRI as well as multiple ex vivo sample imaging in order to achieve higher throughput to dedicated instrumentation and set up for direct MR imaging of histology sections.

In the introductory chapter (Chapter 1), we describe the set of tools and protocol that enable the characterization of each MRI probe used in our study. The systematic characterization for both existing commercial MRI coils and the one we develop in-house during this work allow for direct comparison of their performance.

In chapter 2, we investigate the homogeneous RF resonators dedicated for in vivo studies with a particular focus on birdcage resonators. After examining the main advantages and

limitations between low and high pass structures, we introduce the practical steps required to design a high pass birdcage structure aimed at whole mouse body imaging. Examples of serial imaging illustrate the excellent RF coverage of the whole mouse body in order to screen qualitatively the pharmacokinetic properties of newly designed contrast agents. For mouse head imaging, we aimed to increase the coil sensitivity relative to an existing commercial coil by reducing the geometry structure to closely fit the region of interest. The resulting gain in filling factor achieved without compromising the overall homogeneity of the RF field covering the brain region lead to 10% gain in Signal-to-Noise Ratio (SNR) or an equivalent 20% reduction in imaging time.

Chapter 3 introduces the importance of ex vivo MRI as a crucial step for pulse sequence development, optimization of imaging parameters to maximize signal and/or image contrast as well as for the testing of newly designed protocols. This is also an important stage to help better validate in vivo MRI findings with histology by bridging the gap in co-registration between their differences in spatial resolution. Indeed, higher spatial resolution can be acquired with ex vivo scanning by accumulation of repeated motion free acquisitions over long unattended hours. We sought to expand the MRI access by taking advantage of "unused" overnight time slots. Our work led us to design larger structure to scan simultaneously multiple samples while insuring adequate MRI sensitivity to achieve less than 100-□m isotropic resolution and therefore increase the resulting throughput. Our proposed RF coil structure, sample set up and improved pre-amplification resulted in accommodating up to eight extracted fixed whole mouse brains while providing excellent homogeneous RF coverage within the linear region of the gradient coil. Examples shown illustrates the use of this new set up for screening large cohorts of samples to test newly designed Alzheimer's plaques targeted contrast agents during eight hour overnight MRI scans with an eight brain sample throughput.

Chapter 4 explores the design and use of a set of original closed coil structures that fits closely the planar shape of a histology slide insuring the best compromise between RF homogeneity, coverage and filling factor. The resulting gain in sensitivity of these structures are investigated and compared with a commercial whole head MRI. Examples

are shown in which superb co-registration between ex vivo and histology have been achieved.

Les travaux realizes dans cette these ont fait l'objet de 9 publications:

D. M. Hoang, E. B. Voura, C. Zhang, L. Fakri-Bouchet, and Y. Z. Wadghiri. *"Evaluation of coils for imaging histological slides: Signal-to-noise ratio and filling factor"*. **Magn Reson Med**, Jul 15 (**2013**).

Y. Z. Wadghiri, J. Li, J. Wang, **D. M. Hoang**, Y. Sun, H. Xu, et *al*.. *"Detection of amyloid plaques targeted by bifunctional USPIO in Alzheimer's disease transgenic mice using magnetic resonance microimaging"*. **PLoS One**, vol. 8, p. e57097, (**2013**).

A. Bertrand, U. Khan, **D. M. Hoang**, D. S. Novikov, P. Krishnamurthy, H. B. Rajamohamed Sait, B. W. Little, E. M. Sigurdsson EM, Y. Z. Wadghiri. *"Non-invasive, in vivo monitoring of neuronal transport impairment in a mouse model of tauopathy using MEMRI"*. **Neuroimage**, PMID: 22960250. Aug 31 (**2012**).

Y. Z. Wadghiri, **D. M. Hoang**, T. Wisniewski, E. M. Sigurdsson. *"In vivo Brain MR imaging of amyloid plaques in transgenic mice"*. **Amyloid Proteins, Methods in Molecular Biology Series 2nd edition**, vol.849:435-51. PMID: 22528108(**2012**)

S. Russell, R. Casey, **D. M. Hoang**, B. W. Little, P. D. Olmsted, D. S. Rumschitzki, Y. Z. Wadghiri, E. A. Fisher. *"Quantification of the Plasma Clearance Kinetics of a Gadolinium-Based Contrast Agent by Photoinduced Triplet Harvesting"*. **Anal Chem.** PMID: 22971115, Sep 18. (**2012**).

L. Fakri-Bouchet ; **D. M. Hoang** ; A. Kadjo ; T. Cong Truong ; Y. Zaim Wadghiri ; A. Briguet ; D. Graveron-Demilly. *"Sensibilité et limite de détection de micro capteurs RMN: Aspects méthodologiques"*. **Journal National de la recherche dans les IUT**, JCNR (**2012**).

J. Yang, Y. Z. Wadghiri, **D. M. Hoang**, W. Tsui, Y. Sun, E. Chung, Y. Li, A. Wang, M. de Leon, T. Wisniewski. *"Detection of Amyloid Plaques Targeted by USPIO-Aβ1-42 in Alzheimer's Disease Transgenic Mice using Magnetic Resonance Microimaging"*. **Neuroimage**, 55(4):1600-9. PMID: 21255656. (**2011**).

A. Bertrand, **D. M. Hoang**, U. Khan, Y. Z Wadghiri. *"From axonal transport to mitochondrial trafficking: What can we learn from Manganese-Enhanced MRI studies in mouse models of Alzheimer's disease?"*. **Current medical imaging reviews** 7(1):16-27. (**2011**).

L. Fakri-Bouchet, A. Kadjo, C. Rousset, P. Poulichet, **D. M. Hoang**, A. N. Fakri, Y. Z. Wadghiri, L. Rousseau, A. Briguet, R. Cespuglio, D. Graveron-Demilly. *"Réponse du tissu cérébral de modèle animal à une implantation chronique de Micro-capteurs RMN"*. **Journal National de la recherche dans les IUT**, JCNR (**2010**).

Chapter I: Important elements in coil design and characterization

Introduction

Current magnetic resonance (MR) imaging installations vary considerably in design and configuration in particular with the specifications of hardware assembly forming it. The complexity and combination of the technological solutions offered by MRI manufacturers ranges from the type and strength of the magnet that creates the polarizing magnetic field B_0 to the control of the hardware interfaced to it. Despite the large variety of choices and solutions available, every system includes several essential components.

As part of the active components acting as a source in an MRI system, the static magnetic field (usually referred as B_0) is needed to create a net nuclear spin magnetization. It is complemented by two additional types of secondary varying magnetic fields commonly termed gradients and radiofrequency (RF) components. Both of these additional sources of magnetic fields are controlled spatially and/or in time in order to manipulate the net nuclear spin magnetization.

The gradients component refers to three dimensional (3D) field gradients that are superimposed to B_0. These gradient fields are induced by three separate power supplies driving electric currents to a set of electromagnetic coil windings to induce and control spatial variations of the net nuclear spin magnetization.

On the other hand, the RF transmitter (T_x) chain consists of frequency synthesizers, attenuators, and RF amplifiers to generate RF excitation current pulses to one or more transmitter antenna (also termed RF coil). The induced varying electromagnetic field (commonly termed B_1 in contrast to B_0) applied to the subject is of 3 dimension (3D) nature and only the component perpendicular to B_0 is effective to tip the nuclear spin magnetization into the desired orientation following a sequence of appropriately timed pulses.

On the receiving side, the resulting magnetization can then undergo a free precession and induce a weak observable RF signal in one or more receiver (R_x) RF coils placed ideally closely to the subject. A pre-amplifier amplifies the received MR signal for further signal adjustment, filtering and processing before digitization at the end of the receiver chain to

be subsequently processed by the scanner's host computer. A more detailed description of each element of the acquisition chain will be described later in this chapter.

It is important to note the dual role that an RF coil plays in an MRI installation both during the RF excitation and the signal reception while being at the interface between the subject or sample examined and the rest of the instrumentation. Its main function is to transform the electric energy into RF electromagnetic energy to excite the molecules in the subject. Inversely, the coil also converts the magnetic energy stored by the subject into an electrical signal that can be subsequently processed by other elements of the acquisition chain.

In this current thesis, a large part of our efforts have been focused at the instrumentation level of the MR system equipping our small animal MRI facility operated as a research service core. Importantly, the characterization of existing RF coils as well as the design of new structures have been the central part of our work. Our objective aimed principally at overcoming the sensitivity and throughput limitations associated with each project described in this work. The variety of new RF coils designed in this thesis was driven by the experimental needs for every study while addressing the associated practical constraints imposed by the nature of each dedicated setup.

In this chapter, we first examine the basic elements forming the acquisition chain followed by a detailed description of the principles of coaxial cable lines highlighting their critical role in effectively transmitting the MR signal. As an essential element of the reception, the RF coil, its role as well as its principal attributes are also examined in details. Importantly, the attributes that predominantly dictate the overall performance of the coil are studied. We describe in details how each attribute can be practically characterized and also outline the methods and tools we have used for their characterization and optimization during the course of our study.

I. Basic elements in the MR Acquisition chain

The MRI system is composed of highly complex components combining high and low power modules that must be applied in a timely fashion to acquire an MR signal. These modules range from high power current transformers or RF amplifiers in the transmitter side to low power preamp for the RF signal in the receiver chain. Importantly, the RF coil plays a central role in bridging the transmission and receiving parts of the MR system. During the excitation, from several tenths to a couple of hundred volts are applied to this last element of the transmission chain in order to induce enough RF energy to polarize the net nuclear magnetization to the transverse orientation within the part of the small animal subject examined.

Conversely, the same structure at the forefront of the receiver chain, experiences a very low signal within the microvolt to millivolt range that is induced by the tissue examined during the detection phase of the experiment. This signal is then amplified and further processed at various stages of the receiver chain before digitization. The main components of the receiver chain are summarized in Figure I-1.

Figure I-1: *Schematic of a general MRI signal acquisition chain*

I.1. The pre-amplification stage

The MR signal strength available within a coil is dependent on the sample size, the nature of the sample, the coil size and performance as well as how it is coupled with the subject. The wide range of the signal variation encountered during each experiment can vary from microvolts down (μV) to levels as low as nanovolts (nV) nearing the noise floor. In the latter case, any source of noise (cable noise, environmental noise) can impact the signal quality and lead to irreversible downstream consequences on the quality of the acquisition. Hence, it is crucial to amplify the high frequency signal generated in the RF coil at the most upstream point possible of the Rx chain to render the acquisition more immune to perturbation induced by environmental and experimental fluctuations. In common practice, the initial amplification is performed using a low-noise analog pre-

amplifier (pre-amp) with a fixed high-gain located at the vicinity of the magnet bore. For dedicated setup and coils, the pre-amp can be built-in as part of the RF resonator. In small animal MRI systems the pre-amp gain usually ranges from 20dB to 30dB depending on the MR installation and the type of experiment commonly acquired.

I.2. The Attenuator stage

The fixed gain of the preamp can in turn amplify the signal variations previously described to levels that may go over the signal threshold permissible at the input of the Analog-to-Digital converter (ADC). Accordingly, a set of attenuator with gain adjustable by the operator must be inserted in order to fit the acquired signal within the acceptable input range and prevent error overflow. This will also enable an optimized conversion by benefiting from the best dynamic range defined as the ratio between the largest and the smallest signal observable. The attenuator has a variable gain that can be adjusted to level down or amplify the signal for an accurate sampling of the ADC.

I.3. Analog to Digital Converter

The ADC stage has the role of converting the acquired analog signal into digital information that can be processed by the host computer and subsequently translated to an interpretable result (image, spectrum, etc.). The quality of the ADC is achieved by a trade off between the rate at which the signal can be sampled and the number of finite sampling steps utilized to quantizes the signal amplitude and distinguish small voltage variations.
The sampling rate defines the number of samples per unit of time and is usually termed in the MRI field as the bandwidth (BW) or spectral width (SW) ranging from few kilohertz to several megahertz.
On the other hand, the accuracy in sampling the amplitude variations is defined by the dynamic range (DR) of the ADC. In other terms, the DR reflects the ability of the ADC to discern reliably small input signal fluctuations in presence of large amplitudes by minimizing error quantization. The DR is practically measured by the numbers of steps used during each measurement as a ratio of the largest possible output (full-scale voltage) to the smallest possible detectable signal. It is commonly defined by the bit resolution *N*

of the ADC where 256 levels correspond to an 8-bit resolution (256 levels=2^8) and can be formulated mathematically in decibel unit (dB) as follow:

$$DR=20 \log_{10} 2^N \approx 6.02\ N.$$

Common modern scanners are equipped with ADC providing DRs ranging from 12-bit (4096=2^{16}, ~96dB) to 20-bit (1,048,576=2^{20}, ~120dB) depending on the sampling acquisition rate requirements spanning from 10kHz to 5MHz. For example, experiments with large amplitude variations yet requiring accurate measurements of small signal fluctuations (the least significant bit or quantum voltage) will result in operating the ADC at the highest bit-resolution (20-bit) but at the expense of a slow sampling rate (BW=10kHz). Conversely, imaging experiment imposing the ADC to operate at high sampling speed such as echo-planar imaging will result in signal acquisition with less DR accuracy. It must be noted that the size of the sample and the spatial resolution of the images are both important factors that extend the dynamic range of the signal intensity requiring higher bit-resolution.

I.4. The acquisition chain of our MRI system

.The small animal MRI system in which this whole study was performed is comprised of a 7-Tesla (7-T) superconducting magnet with a 200-mm horizontal bore (Magnex Scientific, Yarnton, UK) interfaced to a Biospec Advance II console (Bruker Biospin MRI, Ettlingen, Germany). The installation is equipped with an actively shielded gradient coil (Bruker BGA-9S; 90-mm inner diameter, 750-mT/m gradient strength, 100-µs rise time). The acquisition chain in this system can be summarized into several main stages as follow:

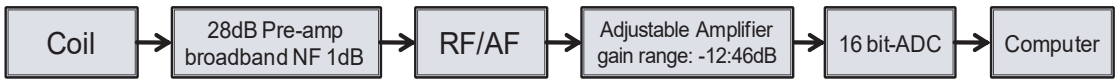

Figure I-2: *General schematic of the acquisition chain equipping the small animal 7-Tesla Bruker Biospec MRI system at the New York University School of Medicine.*

where the RF/AF stage is a radio-to-audio frequency converter in which the 300-MHz radiofrequency input signal acquired by the 7-T spectrometer is demodulated relative to the input frequency from the frequency synthesizer and down-converted into an audio frequency range (from 1000Hz to few hundred kHz) as a quadrature signal (with real

and imaginary component) that can be operated more effectively by the ADC with a wider dynamic range (DR).

I.5. Definition of noise figure

Each element of the chain will contribute some noise level to the transmitted MRI signal and affects the quality of the resulting images. The contribution of noise can be defined by the noise factor F of each element as follow:

$$\boldsymbol{F = \frac{SNR_{in}}{SNR_{out}}} \qquad \text{(I-1)}$$

SNR_{in} and SNR_{out} are respectively the input and output SNR ratios. For standardization purposes, the notion of noise figure NF is defined as:

$$\boldsymbol{NF = 10\log_{10}\left(\frac{SNR_{in}}{SNR_{out}}\right) = SNR_{in,dB} - SNR_{out,dB}} \qquad \text{(I-2)}$$

where $SNR_{in,dB}$ and $SNR_{out,dB}$ are defined in decibels (dB) and the noise figure NF represents the noise factor quantified in dB.

Among the various elements of the acquisition chain, the built-in pre-amp is the only stage where the users may have the opportunity to alter the hardware configuration based on the projected experimental needs. Specifically, limiting the experiments to proton (^{1}H) nuclei would enable the use of narrow band pre-amps known for their improved noise figure compared to their standard broadband counterpart. The latter are installed by default by manufacturers to enable the wide use of the scanner in various setup conditions and for multi-nuclei needs. In practice, the difference in NF characteristics between a broadband and a narrowband pre-amp commercially available can be greater than two to five-fold in dB ratio. The expected effective gain in SNR from NF improvements will be described in details and also demonstrated by experimental measurements in chapter III.

I.6. RF signal transmission - the importance of the coaxial cable length

The coaxial cable plays an important part in the acquisition chain by enabling the connection of one module to another and by acting as a transmission line for the radiofrequency signal. Its central role in transmitting the RF signal is described in details

in the next paragraph with a historical perspective. The optimal conditions of the coaxial length to maximize the signal transmission are also examined through intuitive illustrations using the standing wave phenomenon as well as using equation formalism.

I.6.1 The invention of coaxial cable

In a general case of a direct current (DC) or low frequency alternating current (AC), a conductive line is commonly used to transmit the signal from one point to another with very negligible losses. However, in the RF domain (spectrum ranging from few MHz to 1GHz) electromagnetic currents alternate direction millions or billions of times per second (in the case of MR, it's hundreds of millions); the energy tends to radiate off as radio waves, causing power dissipation. To prevent this detrimental radiation, a second layer of conductive material is used to surround the conductive core along its length. Oliver Heaviside, a self-taught English electrical engineer, mathematician, and physicist was first to invent this type of cable, called "coaxial cable", in 1880. He concluded that wrapping an insular casing around a transmission line both increases the "clarity" of the signal and improves the durability of the cable. In 1930, Herman Andrew Affel patented the first recognizable coaxial cable on behalf of AT&T's Bell Telephone Laboratories. This version of coax was the first to feature two transmission wires sharing the same axis, allowing for wider frequency range [1].

I.6.2 The phenomenon of stationary wave (standing wave)

In addition to dissipative radiation, reflection is another cause of energy loss in RF signal transmission. This loss, analogous to a mechanical transmission, can be easily illustrated using a string undergoing an oscillating wave pattern (Figure I-3 to I-5) under a stationary regime (standing wave) as follow:

At one end of a string with a certain tension, a vibration with a force F is induced:

Figure I-3: *Causing a vibration by applying a force at one end of the string*

This vibration will create a transverse wave traveling along the length of the string:

Figure I-4: *Transverse wave traveling along the string*

If the two extremities of the string are tied, the wave will travel from the first end along the string to the other end where it will be reflected backward and inverted. The continuation of the oscillation pattern will lead to a combination of incoming and reflection waves crossing each other in either a constructive or destructive manner. A judicious choice of the oscillating frequency based on the length of the traveling path (L) could lead to stationary waves if L is at least equal to half of the wavelength $\lambda/2$ or its multiple $n\times\lambda/2$ leading to a perfect reflection (See Figure I-5). Upon becoming a standing wave, the patterns won't travel along the string, but will stay in the same place with the waves oscillating around stationary nodes. In this case, specific points x of the path will undergo minimal vibration at $x=n\times\lambda/2$ while others will experience maximal amplitude at $x=(2n+1)\times\lambda/4$.

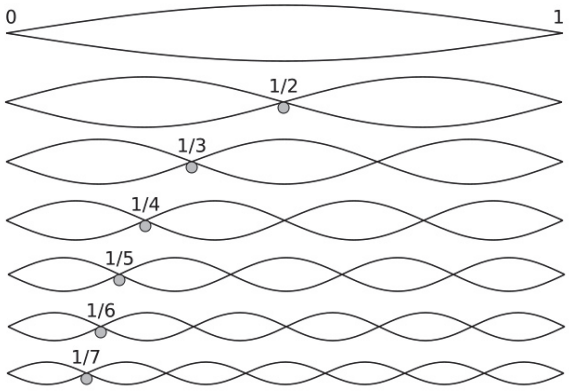

Figure I-5: *Example of standing wave patterns on a vibrating string that occurs at certain specific frequencies when the traveling path is at least equal to half or a multiple ($n\times\lambda/2$) of the wavelength. The effect is a series of zero-nodes (no displacement) and anti-nodes (maximum displacement) at fixed points along the transmission line.*

Under specific wavelength-based regime conditions, this effect can be practically utilized to minimize or maximize the effect of the amplitude of the oscillations by conveniently choosing the point of measurement within the path of the traveling wave. Conversely, in

MRI we are faced with the opposite problem in which the operating frequency is fixed and imposed by the static magnetic field strength of the MR instrument and by the gyromagnetic factor of the nuclei studied. In this case, the length of the coaxial transmission line must be chosen so that the input electrical signal is maximized at the end of the chain before feeding the pre-amplification stage. For instance, in order to create a pure traveling wave at the Larmor frequency of interest, the length (x) of the coaxial transmission line must be chosen to be an odd multiple of the λ/4 as follow:
x =(2n+1)×λ/4. Failure to accommodate these conditions would generate partial reflection leading to attenuation and distortion of the signal.

I.6.3 Calculation of coaxial cable length

Knowing that the traveling speed of a wave only depends on the characteristic of the medium in which the wave travels in, we have:

$$\boldsymbol{V = f \times \lambda} \qquad \textbf{(I-3)}$$

Where V is the velocity factor (speed of waves in the cable); this factor depends only on the dielectric constant k of the cable material:

$$\boldsymbol{V = \frac{1}{\sqrt{k}}} \qquad \textbf{(I-4)}$$

The velocity of the cable is given by the manufacturer in relation to the speed of light – usually termed v which can be transcribed as follow:

$$\boldsymbol{C \times v = f \times \lambda} \qquad \textbf{(I-5)}$$

where C is the speed of light in free space. The wavelength can then be easily calculated by:

$$\boldsymbol{\lambda = \frac{C \times v}{f}} \qquad \textbf{(I-6)}$$

Since we aim to achieve a traveling wave regime, the coaxial cable must have a length L of 2n+1 times of quarter the wavelength of the transmitted signal as follow:

$$\boldsymbol{L = (2n+1) \times \frac{\lambda}{4} = (2n+1) \times \frac{C \times v}{4f}} \qquad \textbf{(I-7)}$$

Under the same basis, we will see later that there may be a need to construct "half-wavelength" coaxial cables to inverse the phase of the signal. In this case, the length of the cable must adhere to the following condition:

$$\boldsymbol{L = (2n + 1)\times\frac{\lambda}{2} = (2n + 1)\times\frac{C\times v}{2f}} \qquad \textbf{(I-8)}$$

II. Coil performance and attributes (characteristics)

As previously outlined, MRI coils are commonly operated as bidirectional transducers converting the electric energy into electromagnetic energy and vice-versa. Hence, depending on the coil design, the experimental setup, the requirements and the constraints of the study, each coil may either be utilized in transmit-only (T_x-only), in receive-only (R_x-only) or on dual T_x/R_x mode.

In clinical settings, the evaluation of a coil performance is vital as part of the MRI safety procedure in order to reliably estimate the amount of dissipated radiofrequency energy that a subject will be exposed to. The rate at which the energy is absorbed by the body when exposed to RF is globally measured by the specific absorption rate (SAR) [2-6]. In this case, SAR represents a global measure of the transmission characteristics of a coil by evaluating the average amount of power absorbed per mass of tissue (expressed in watt per kilogram: W/kg) over the region covered by the RF coil. The measured value will depend heavily on the type of RF resonator used as well as the nature, geometry and proximity of the tissue exposed to the RF energy. Thus, transmission tests must be made with each specific type of MRI coil acting as the RF source and at the intended anatomical position of use. Furthermore, the measurement is made under the assumption of a uniform radiation and dissipation known not to be the case.

A more accurate evaluation would require the assessment of the coil performance spatially through a precise mapping of the RF field emitted throughout the imaged sample. The performance is defined as the rotating field magnitude B_1^+ per RF voltage applied to the coil input based on the following expression:

$$\frac{\boldsymbol{B_1^+}}{\boldsymbol{V}} = \frac{\boldsymbol{\alpha/\gamma\tau}}{\boldsymbol{V}} \qquad \text{(I-9)}$$

where α is the flip angle, γ is the gyromagnetic ratio, τ is the pulse length applied.

The magnitude of B_1^+ can be mapped experimentally by applying rectangular RF pulses to generate a 90^o flip angle of the magnetization with applied voltage amplitude measured at the input of the coil using a defined pulse length τ (a practical value of τ would amount to ~2.56 ms in clinical settings and ~20-µs for small animal coils) [7, 8]. As noted previously, the performance outlined above focuses on the transmission capabilities of the coil and its effect on the sample imaged. Conversely, the performance of the coil can be evaluated when used as a detector which we will define here as the coil sensitivity. These two notions can be interrelated by the principle of reciprocity in resonators operating in dual T_x/R_x mode. However, the sensitivity in R_x-only probes must be characterized based on a different approach that will be described subsequently.

II.1. Coil Sensitivity

The sensitivity of an MR experiment is dependent on many factors with some similar to those affecting the T_x-only mode such as but not limited to the size and the nature of sample being imaged, the operating frequency corresponding to the Larmor frequency of the magnetic field strength it is aimed to operate with as well as the hardware characteristics of the acquisition chain, the ambient temperature and the quality of the experimental calibration (static magnetic field homogeneity, coil tuning and matching). It is therefore very challenging to objectively define or directly measure in absolute terms the sensitivity of a MR coil under varying experimental conditions especially *in vivo*.

Instead, the sensitivity of a dedicated coil aimed at specific anatomical region or organ can be experimentally defined relative to a coil of reference that could be utilized under any condition or setup. In clinical settings, whole volume coils are usually built-in within the magnet bore by MRI scanner manufacturers. This eases the evaluation of the sensitivity of any coil relative to the same whole volume coil used as a reference. Unfortunately this is not a common practice in small animal scanners. Instead, the performance of any coil can be characterized relative to a commercial coil commonly utilized in any imaging facility.

Several factors guide the design of a coil including the filling factor η, the quality factor Q and the homogeneity of the RF field in which all of these aspects will be described subsequently in details. As a general formalism and for practical reasons, the RF sensitivity of a coil has been formulated into a sensitivity factor SRF dependent on both η and Q [9-11]. Using the same sample acquired under identical experimental conditions and with the assumption that the interaction of the coil with the sample is uniform, this dependence can be simplified into the η×Q product as follow [9, 11]:

$$\boldsymbol{S_{RF} = K \times \sqrt{\eta \times Q}} \qquad \textbf{(I-10)}$$

In this expression the constant K assumes that the following parameters are unchanged according to our experimental setup: the Larmor frequency ω_0, the magnetic permeability of free space μ_0, the ambient and sample temperature T_{eq} as well as the volume V_S of the sample.

II.1.1 Quality factor

As it is known in physics, an oscillator will not oscillate forever. The energy of the oscillation dissipates into the surrounding environment, causing a gradual loss of the oscillating amplitude until the oscillator comes to rest. The rate of energy loss of the oscillator reflects its interaction with the environment and its corresponding characteristics.

Analogous to the mechanical resistance experienced by a spring immersed in oil where the oscillating energy is absorbed faster than in air, resonant electric circuits undergo similar dissipated energy. The energy dampening occurs not only within its own resistive components but also when subjected to a load with the surrounding environment it is interacting with. This loss can be characterized by the quality factor (Q factor), a measure of the contribution of power losses. The Q factor can be measured by calculating the ratio between the resonance frequency and the bandwidth at half of maximum energy (-3dB) as illustrated in figure I-6 and defined as follow [11]:

$$\boldsymbol{Q = \frac{f_0}{\Delta f}} \qquad \textbf{(I-11)}$$

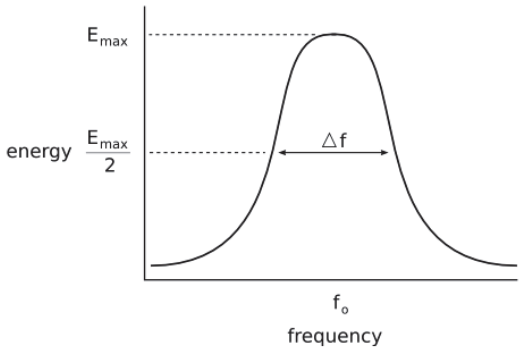

Figure I-6: *Q factor is defined by the ratio between the center frequency and the bandwidth at half of the maximum energy. Q reflects the ability of the coil to restore magnetic energy then converting it to electric energy and also the energy loss induced by both the resistive components within the circuit and also the interaction with the surrounding environment acting as a load.*

The increase of the Q factor will translate into a narrower bandwidth of the circuit and a sharper peak, which reflects a more selective resonant circuit at its center frequency. The Q factor of a MR coil partly indicates its sensitivity and its electrical losses. The Q factor unloaded (Q_U) of a circuit depends on several factors, in the case of an MR coil:

$$\boldsymbol{Q_U = \frac{L\omega}{r}} \qquad \textbf{(I-12)}$$

- *r* is the resistance of the components (the higher the resistance, the lower the Q factor)
- L the inductance of the circuit (represent the capacity to transform electric energy into magnetic energy).
- $\omega = 2\pi f$ is the angular velocity at the resonance frequency *f*.

In presence of sample loading in which the coil is experiencing an interaction with the subject examined, the corresponding Q factor loaded (Q_L) is defined as follow:

$$\boldsymbol{Q_L = \frac{L\omega}{R}} \qquad \textbf{(I-13)}$$

- *R* represents the total thermal resistance including the resistance *r* of the circuit, the sample noise.

II.1.2 Filling factor

The filling factor is a measure of the geometrical matching between the RF coil and the sample being studied. It is defined as the ratio of the magnetic field energy stored inside the sample volume to the total magnetic energy stored by the RF coil [9]. Traditionally this has been expressed as a ratio of the volume of the sample to the volume of the coil assuming a homogeneous coil RF field [10]. In practical terms it represents the fraction of the coil detection volume filled with the sample which translates into fitting the coil closely to the sample of interest to achieve a high filling factor:

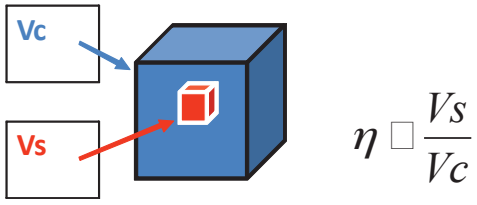

Figure I-7: *The filling factor is a measure of the geometrical matching between the RF coil and the sample being studied. In practical terms it is simplified as the ratio between the volume of the sample and the volume of the coil*

where V_S is the volume of the sample, V_C is volume of the coil and η is the filling factor. In the ideal case, the filling factor is maximized when the volume of the coil is totally occupied by the sample.

The role of the filling factor in improving the sensitivity of the scan and the quality of the resulting images can be described under the following assumptions:

The sample is a volume composed of molecules containing the studied nuclei (predominantly proton imaging in clinical and biomedical research) with a defined concentration C where each nucleus has a micro-magnetic momentum m_n.

When considering an elementary volume dv of the sample, the corresponding magnetic momentum can be formulated as follow:

$$\overrightarrow{dm} = C * \overrightarrow{m_n} * dv \qquad \text{(I-14)}$$

The resulting total magnetic momentum of the whole sample can then be expressed:

$$\overrightarrow{M} = \iiint_V C * \overrightarrow{m_n} * dv \qquad \text{(I-15)}$$

which translates practically by larger sample volume generating greater magnetic momentum $\overrightarrow{M}$.

When considering a coil with a defined size, its capacity to transform electric energy to magnetic energy is fixed. This energy is only partially used to excite the volume of the sample covered by the RF magnetic field. Larger sample volumes of the same nature fitted within the probe will enable greater magnetic energy to be stored and in turn re-transformed to electric signal by the principle of reciprocity. The resulting filling factor η or ratio between the energy that could be detected from the sample and the energy generated by the coil will be solely dependent on the nature and volume of the sample. In practice, fitting the largest possible size of a homogenous sample within an existing coil would translate into a higher η.

Conversely, in presence of a confined sample volume the filling factor would be improved by choosing the smallest coil available yet large enough to accommodate the sample.

In RF coil design, the choice of the probe is primarily dictated by the constraints of the experimental setup. The volume and the shape of the coil are based on fitting closely to the contour of the sample in order to scan under the best sensitivity conditions by achieving the highest possible filling factor [11] while insuring a homogeneous RF coverage.

II.2. RF Coil Homogeneity

During transmission, an RF coil should ideally produce a uniform magnetic-flux density over the region of interest. If the magnitude of the transmitted alternating magnetic field B_1 is not homogeneous, the resulting flip angle of the magnetization will end up varying throughout the region studied leading to unequal coverage and by reciprocity non-uniform signal reception. It is therefore crucial to characterize the three-dimensional B_1 homogeneity of an RF coil in order to circumvent the effective volume that would enable homogenous coverage over the area of interest.

To this effect, the homogeneous volume of an RF coil is commonly defined as the region in which the RF field fluctuation remain within an acceptable margin of deviation from its geometric center usually aligned with the center of the static magnetic field B_0. The

acceptable threshold of the deviation from the center of the coil is usually empirically defined by manufacturers and practically ranges between 10% to 12%. This arbitrary threshold can be re-evaluated by users based on the experimental constraints and needs of the study and the sensitivity to B1 imperfections of the imaging method used.

Various types of RF field mapping approaches can be considered when characterizing an RF coil which span from discrete field plotting techniques [12, 13] and computer simulations [14, 15] to MRI-based imaging protocols in combination with dedicated phantoms [16-23] The main advantage of discrete mapping strategies is the ability to perform the measurements using simple instrumentation easily accessible while requiring minimal space. In this case, the RF field distribution can only be physically sampled under unloaded conditions using a pick up coil [12, 13].

Similarly, computers simulations may be the least demanding method in resources and offer the distinct advantage to enabling easy iterative readjustment of the RF structure studied especially during the conceptual and design phase. However, with RF simulations it is very difficult to fully recapitulate real experimental conditions.

Alternatively, MRI-based RF field mapping are the only methods that can map the effective RF distribution under loading conditions. This latter approach is still an active research topic within the MRI research community. Ongoing efforts are currently fueled by the need for faster and more accurate B_1 mapping methods especially under *in vivo* conditions to predict RF behavior in tissues and predict the heating patterns that may occur under high speed scans leading to increased RF duty cycles in combination with parallel imaging schemes [24, 25] This has been further reinforced by the expansion of ultrahigh field human MRI scanners that are more prone to these imperfections and heating effects [26-29]. Indeed, conventional MR probes acts as 'resonators" that store magnetic and electric energy that is subsequently irradiated in the subject or tissue examined. This leads to the effective transmission of the RF field in the near-field region within a quarter of a wavelength ($\lambda/4$). According to the previously described equation (I-6), the near-field region would extend to 20 cm for 1.5-T, 10 cm for 3-T and only 4 cm for 7-T into the tissue imaged limiting significantly the effective homogenous area of examination..

However, this is not a concern in our studies since our experiments are limited to murine imaging and *ex vivo* samples that are within the near-field region of interest. Consequently, the RF field mapping in our case is less critical and can be qualitatively evaluated based on the variation of the signal intensity throughout an image set relative to the geometric center of the coil. In this case, the 3D mapping dataset is acquired from a homogenous phantom filling the whole volume of the coil. A judicious choice of the pulse sequence combining accuracy and speed as well as the loading nature of the phantom are among the important factor to consider in this process to account for the variable nature and loading effect of the samples examined as well as to replicate the broad range of experimental conditions. In this study, we implemented a simple protocol to evaluate qualitatively the overall homogeneity of a coil via a normalized signal intensity-based 3D map relative to the center of the coil acquired from a doped water-filled homogenous phantom (see Appendix section).

II.3. The quadrature detection: an effective way to improve both the coil sensitivity and homogeneity

The principle of the quadrature detection is based on taking into account the contribution of individual signals detected from either two different coils or from two distinct modes of the same coil to be accumulated after an appropriate phase shifting that results into an SNR enhancement. Under optimal condition enabling 90 degrees rephasing, the signal gain by accumulation can reach up to two fold. Conversely, if the noises from the two signals are fully uncorrelated, their accumulation will result into a $\sqrt{2}$ noise level increase. The overall averaging would lead in theory to an increase in SNR of the final signal up to $\sqrt{2}$ fold [30]. In this work, we will focus on the circular polarization mode (CP mode) which is a particular case of the quadrature detection. Specifically, the benefits of the CP mode will be examined in details on birdcage coils where it is the most widely utilized structure thanks to both the gain in SNR as well as the improvement in the RF homogeneity that can be achieved. We will describe in details in Chapter 2, the practical methods we utilized to characterize the effect of the CP mode on the two main attributes: sensitivity and homogeneity.

III. Tools and methods for coil characterization

In this section, we describe the various instruments and set up that we have used during the course of our studies in order to help characterize all of the MRI resonators either purchased from vendors or designed in-house.

III.1. Network Analyzer

The evolution of complex electrical circuits and components operating at high frequency RF especially in telecommunication has rapidly led to the use and development of dedicated instruments enabling the accurate measurement of the transmission, reflection and impedance characteristics of these elements in order to improve their characterization and design. To this effect various systems (oscilloscopes, signal sweep generators, impedance hybrid bridges, frequency synthesizer, etc..) are combined in order to establish a dedicated setup to enable a comprehensive analysis. This has naturally led to the design of a single instrument termed vector network analyzer that measures both amplitude and phase properties. This instrument, also commonly referred as network analyzer (NA) is equipped with its own screen and can extract and visualize rapidly a complete set of parameters (transmission, reflection and impedance etc..) into a single two-dimensional representation. NA are principally used to characterize two-port components such as amplifiers and filters, but they can be used on array networks with an arbitrary number of ports such as in the case of array of coils used in parallel imaging. The electrical characterization of linear components under matched loads is assessed by injecting electrical signals under various steady state stimuli. The set of parameters that can be extracted are part of the elements of a scattering matrix usually referred as S-parameters. These parameters describe the way in which the insertion of a component or a network into a transmission line affects the traveling currents and voltages after causing a discontinuity. This is analogous to a traveling wave experiencing impedance differing from the overall line's characteristic.

In the MRI field and most particularly in RF coil design, the network analyzer plays a fundamental role in helping for the design and characterization of RF coils. Specifically, the NA enables the identification of the resonant modes but also measures the level of isolation between channels in quadrature or between Tx and Rx channels during decoupling. It also allows the evaluation of the extent of signal reflection and

associated losses via the quality factor Q. Each one of these attributes will be examined and described in details in the coming chapters as they are employed.

Importantly, some of these measurements can be assessed either by directly interfacing the MRI probe to the NA or by the inclusion of a dedicated small coil in order to better control spatially the point where the RF signal is investigated. These small loops, commonly termed "pick-up" coils are important homemade tools that facilitate the characterization of RF probes in various conditions irrespective of the matching/tuning circuit. Their in-house design is dictated by the size of the MRI probe studied as well as the nature of the measurement. As an example, they enable the easy identification of the frequency modes as well as to accurately evaluate either the reflection or the isolation of the RF signal. A description of their principle and design will be detailed in the subsequent paragraphs.

III.1.1 Pick-up coils

In electromagnetism, an electric current circulating within a wire loop generates an external magnetic field (Figure I-8) with magnitude and patterns that can be described by the Biot-Savart law expressed by equation (I-16).

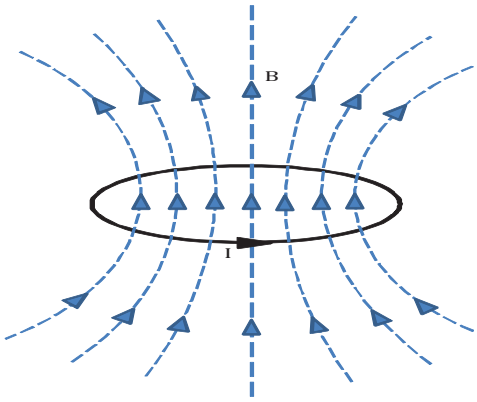

Figure I-8: *Magnetic field generated by a current loop*

$$\boldsymbol{B} = \frac{\boldsymbol{\mu_0 I}}{\boldsymbol{4\pi}} \int_{\boldsymbol{C}} \frac{\boldsymbol{Idl} \times \boldsymbol{r}}{|\boldsymbol{r}|^{\boldsymbol{3}}} \qquad \textbf{(I-16)}$$

where r is the full displacement vector from the wire element to the point at which the field is being computed and μ_0 is a constant $4\pi\times10^{-7}\mathrm{T.m/A}$ representing the magnetic counterpart of the Coulomb force constant k. While k reflects how much

electric field is produced by a given amount of charge, μ_0 relates the current to the magnetic field.

By reciprocity, placing a wired loop under a time-varying magnetic field will induce electromotive force (EMF) across the loop following Faraday's law of induction. This principle can be extended to two coil directly coupled coils with their respective self-inductance leading to a mutual inductance M. In the case of resonant inductive coupling where two coils tuned to resonate at the same frequency and are placed in proximity to each other, the RF energy within their resonance can be more efficiently transferred if appropriately coupled. On the other hand, placing a pick-up coil near an MRI resonator will capture most of the near field energy (well within the 1/4 wavelength distance) predominantly within the resonance frequencies as exemplified below.

a) Single loop pick-up coil

For the design of a single loop pick-up coil [11, 31], the circular wire is usually connected in one side to the inner conductor of a coaxial cable while and on the other end to the outer conductor of the coaxial cable (ground shielding part) illustrated by the example in Figure I-9.

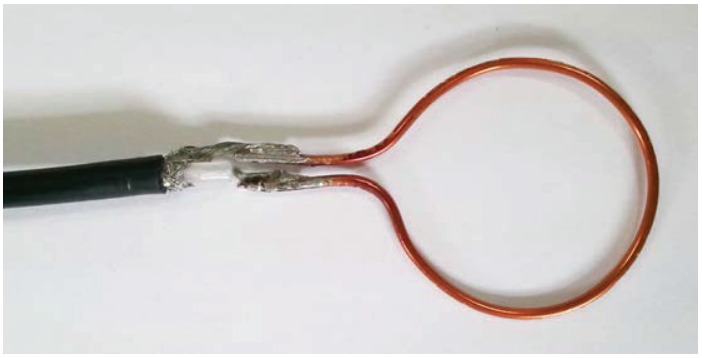

Figure I-9: *A single pick-up coil is composed of a wire loop in which one end is connected to the conducting core of the coaxial cable and the other end is connected to ground layer.*

With the help of a network analyzer, we can generate an RF signal with a broad frequency range within the pick-up coil acting as a RF radiating source and from which we can measure the loading effect that the loop coil will be experiencing from the surrounding environment. Part of the RF electromagnetic field energy radiated from the

coil may be absorbed by the sample impedance depending on its conductive nature. Interestingly, the coil would be considered unloaded when placed in air acting as a very good insulator due to its very high impedance. In this case, the radiating RF power of the unloaded pick-up coil will be in most part fully reflected back to the coaxial cable. It must be noted that the extent of power reflection will depend on the air content where its equivalent impedance (near infinite) may be altered with humidity and in presence of conductive particles. The amount of RF reflected energy can be easily monitored via the equivalent reflection coefficient $\boldsymbol{\Gamma}$ (in dB) using the network analyzer by comparing the outgoing S_{out} radiated by the coil and the reflected S_{refl} signals within the coaxial cable as follow:

$$\boldsymbol{\Gamma = 10 \log_{10}\left(\frac{S_{refl}}{S_{out}}\right)} \qquad \text{(I-17)}$$

A fully reflected RF signal such as in air will lead to a 0dB reflection coefficient $\boldsymbol{\Gamma}$ within a broad frequency spectrum depicted by the flat line in Figure I-10.a. When surrounded by a more conductive material (such as tissue or water), the power generated by the NA will be partially absorbed by the sample load that has an equivalent impedance, causing a reduction in power reflection. This is illustrated in Figure I-10.b by the reflection profile of a human tissue (in this case a human thumb) within a frequency spectrum ranging from 250MHz to 350MHz. It is important to note that the reflected power of tissue measured here within this 100MHz interval is continuous and ranges approximately between -5dB and -10dB.

In contrast, the insertion of the radiating pick-up coil within an MRI resonator leads to a selective and greater absorption of power within a set of defined frequency ranges corresponding to the various resonant frequencies that the RF probe has been tuned for. As an example, the drop in reflection coefficient depicted in Figure I-10.c corresponds to a Birdcage resonator in which the homogeneous mode is tuned to 310MHz. We can see that the reflection coefficient drops considerably by a near -15dB compared to the baseline demonstrating the intended selective nature of the MRI probe to permeate RF absorption from an RF source at a discrete frequency band. In this case, the load (here the MRI resonator) will have a significant drop in impedance at the resonance frequency compared to the high impedance of the baseline. This example shows the most important

attribute that dictates the sensitivity of an MRI coil: its ability to selectively permeate the absorption of a source of magnetic energy and transform it into electric current at a distinct frequency. While the depth of the pic shown here corresponds to the least amount of power reflection, the width of the pic resonance represent the ability to selectively focus the absorption of the broad RF power within a narrow frequency band while reducing the dissipated loss outside this frequency range. Notably, this approach can be utilized is an analogous way to define the quality factor that we previously described in paragraph II-1.1. . In this case, it is assumed that the loop size is small enough to exert a negligible self-inductance which corresponds to a very high self-resonant frequency far away from the resonance frequency of the MRI probe. This would prevent the pick-up coil from interfering with the electrical properties of the receiving resonator. In practice, this translates into insuring that the size ratio between both coils is important enough to render the mutual inductance negligible yet enabling measurable RF power.

a. 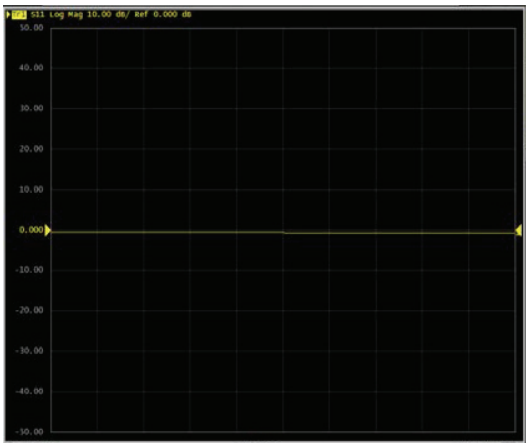

b. 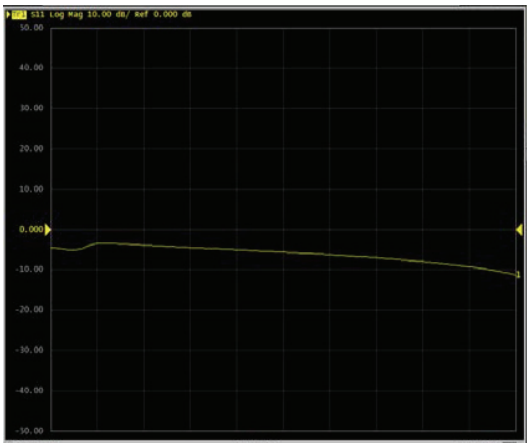

c. 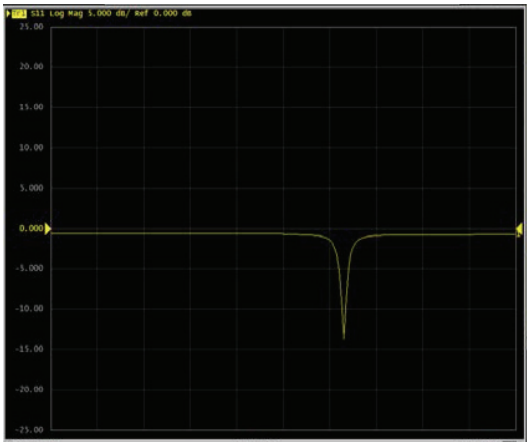

Figure I-10: *Using the network analyzer, the figure depicts the frequency dependence of the reflection coefficient profile of the pick-up coil under various loading.* a). Under unloaded condition when the coil is placed in air, the RF power is fully reflected corresponding to (Γ=0dB). a) When loading a coil with a conducive tissue sample (here human thumb), we can observe a continuous attenuation throughout the frequency spectrum with attenuation of the reflection as high as Γ=-10dB. c) When coupling the pick-up coil with an MRI resonator, the attenuation is much greater ($\Gamma\sim$-15dB) while frequency selective and corresponding to the tuned resonance of the probe.

b) Dual-loop pick-up coil

Dual-loop pick-up coils [11] can also be useful in MRI probe design and conception as they provide a much greater sensitivity in identifying resonance modes of birdcage coils as well as directly measuring the Q-factor of a resonator separately from the matching and tuning stage. In the following paragraph, we will describe in details this important tool.

This type of coil is composed of two identical single pick-up coils that must be ideally fully decoupled (easily obtained a decoupling factor of more -30dB). One of the loops is used to transmit (Tx) the signal while the other is utilized for the detection (Rx). As an example, the dual-loop coils we designed and used extensively during the course of this work using a planar alignment that can be seen in Figure I-11.

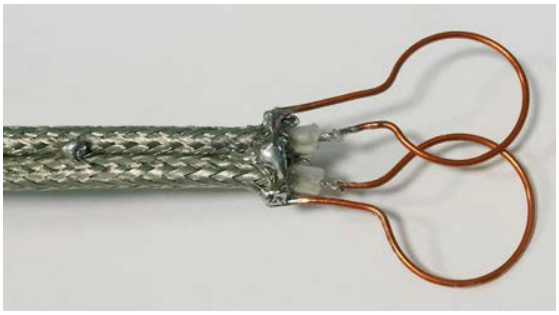

Figure I-11: *Example of dual-loop pick-up coil composed of 2 wire loops overlapping each other. In this case, the geometrical decoupling is based on a planar alignment. The distance between the centers of two perfectly circular loops should be approximately equal to the ninth of the diameter of each loop in order to achieve optimal decoupling. The geometrical imperfections resulting from the coil design require achieving empirically the most favorable decoupling with the help of the network analyzer.*

The dual-coil setup relies on the fact that both coils are fully isolated from each other in the absence of any interaction with the surrounding environment. In this case, despite transmitting high RF power in one coil, the receiving pick-up side will be immune to any signal detection. However, when the dual probe is inserted within a MRI resonator, both loops will be interacting individually with the host leading to indirect mutual coupling.

By placing this dual-loop pick-up coil close to the MRI probe, the transmitting loop will generate a magnetic field at a broad range of frequencies through the help of the network analyzer. At the resonant frequency of the probe, the magnetic field emanating by the Tx coil will induce a current within the MRI resonator which in turn will radiate a secondary magnetic flux subsequently absorbed by the Rx loop. This detection can be visualized on the network analyzer by an upward peak illustrated by the example in figure I-12. This upward peak becomes handy where most of the NAs nowadays are designed with a internal function that allows to show instantaneously the value of the Q factor (an example will be given in paragraph III-1.2.b&c)

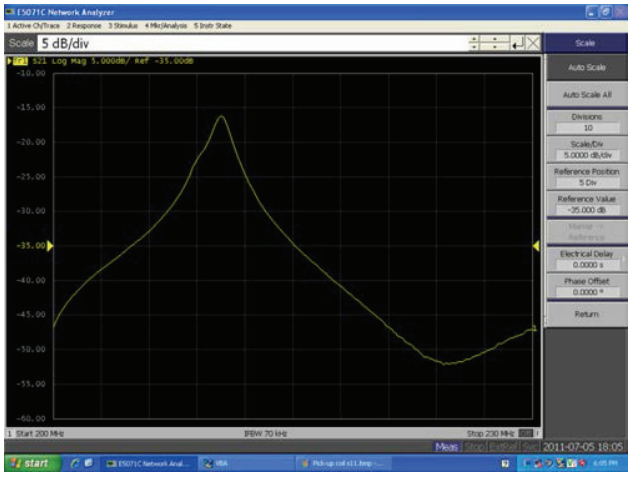

Figure I-12: *The coil resonant frequency is detected by a by a dual-loop pick-up coil as an upward peak visualized by the network analyzer.*

In practice, the isolation between two identical loops can be done by geometric decoupling via either orthogonal orientation or planar alignment with partial overlapping. The latter is the most commonly utilized solution for both its ease of use and construction especially during the adjustment of the geometrical decoupling stage. As an example, the planar alignment we designed and used extensively during the course of this work can be seen in Figure I-11.

The basic principle of this setup can find its explanation in electromagnetism from the same single loop shown previously. In one hand, a circulating current across a single loop coil generates a magnetic field around it that we have previously described by equation I-16 and illustrated in figure I-8. If we place an identical loop without any current that is adjacent to the radiating loop, the magnetic field line from the latter will induce an EMF within the receiving coil thanks to the magnetic flux crossing its surface making both loops mutually coupled. Optimal coupling is achieved when the magnetic flux is maximized in the receiving coil. Conversely, the same identical loops can be fully decoupled if we insure that the net flux through the receiving coil is equal zero despite their overlapping. This would be geometrically possible if we can insure that the magnetic field lines are parallel to the surface of the receiving loop.

Intuitively, one rightly expects that placing two single loop adjacent to each other or together would cause a coupling with a mutual induction that we presently intend to minimize. However, a careful geometric positioning between both overlapping coils

would enable optimal decoupling such that the distance between their centers is approximately 0.9 times their diameter [32]. This distance for achieving a near-perfect isolation could vary slightly depending upon factors such as the shape, material and thickness of the loops as well the conductivity of the surrounding environment. In practice, all of these factors including the geometrical imperfections illustrated by the example we designed and shown in Figure I-12, can be compensated by empirically identifying the optimal positioning with the help of the network analyzer.

III.1.2 Comparison of the different methods for measuring the Q factor

a) Direct measurement from the coil resonant peak: Single port method

In the most straightforward way, we can easily measure the Q factor of an MRI coil by connecting the resonator directly to a single port of the network analyzer in which the matching/tuning circuit is accounted for. This can be done by characterizing the reflection coefficient (*f*) profile of the MRI probe depicted in the example of figure I-13 showing the peak of resonance.

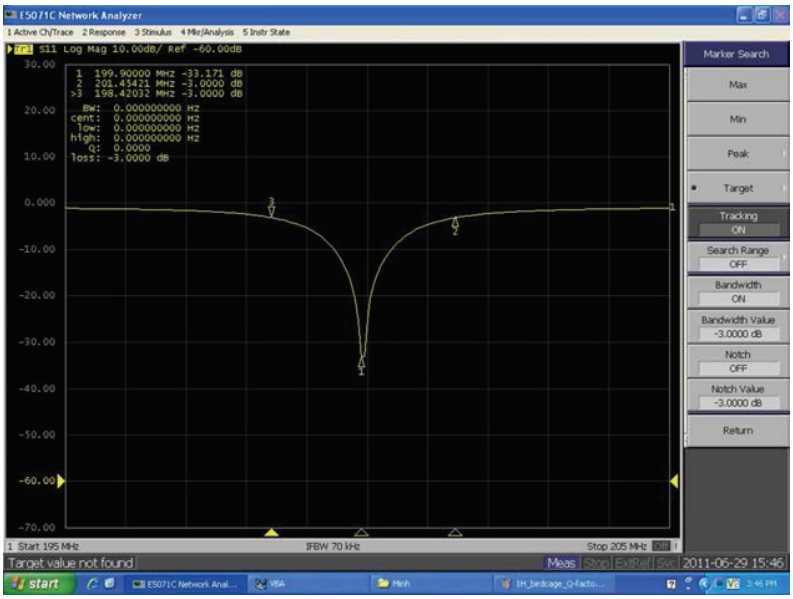

Figure I-13: *Measurement of Q factor by directly plugging the coil to the network analyzer and using the scattering parameter as descriptors defining input and output relations in terms of incident and reflected normalized power waves.*

At the resonant frequency, the coil will absorb most of the power generated by the NA. This causes a loss of reflected signal represented by a downward peak. By measuring the bandwidth Δf at -3dB, we can determine the Q factor as follow:

$$\boldsymbol{Q = (1 + k)\frac{f_0}{\Delta f}} \quad \textbf{(I-18)}$$

where k is the coupling coefficient representing the ratio of power dissipated in the external circuit to the power dissipated in the resonator [33].

When the coil is tuned and matched (in our case at 50Ω in order to optimize power transmission), the power dissipated in the network analyzer and in the coil itself are equal; thus the coupling coefficient k will be 1 and the Q factor will become:

$$Q = 2\frac{f_0}{\Delta f} \quad \textbf{(I-19)}$$

In the example shown in figure I-13, we have the center frequency at 199.9MHz, the bandwidth range at -3dB is: 201.5 – 198.4 which equate to 3.1MHz. As a result, we have the Q factor:

$$\boldsymbol{Q = 2\frac{199.9}{3.1} = 131.8} \quad \textbf{(I-20)}$$

b) Measurement using the single pick-up loop

Another method to measure the Q factor of a coil can employ the single pick-up coil described previously. In this case, two ports of the network analyzer are utilized to connect in each the pick-up loop and the MRI resonator each acting as either the source of magnetic field or the receiver (or vice-versa).

In this case, the measurement will examine the effective transmission of the RF power between both coils illustrated by the reversed peak seen in figure I-14. Importantly, this method is sensitive to the placement of the pick-up coil within the RF magnetic field of the transmitter (or receiver). Hence, during the measurement one must insure enough magnetic flux by approaching the pick-up in proximity of the probe while minimally interfering with its resonance. It must be noted that the measured Q factor (Q=126.13) shown in the example below was from the same coil used previously reveal a subtle difference between both methods.

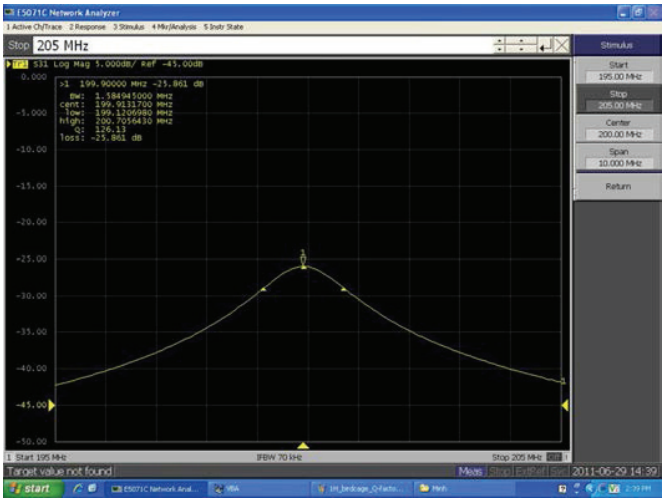

Figure I-14: *Measurement of Q factor of the same coil using a single pick-up coil; in this example, the Q factor measured was 126.13*

c) Measurement using the dual loop pick-up coil

Similar to the single pick-up coil method, the current arrangement utilizes two ports but without the need to connect the MRI probe. This is the only approach that provides the ability to characterize the MRI probe with and without its tuning/matching circuit. This can be very valuable for indentifying the contribution of each stage in the resulting characteristics of the resonator. Similar to the pick-up coil setup, this method measure the effective transmitted power resulting also in an upward peak at the resonant frequency of the MRI probe. The measured Q factor of the same MRI probe amounted to 125.4.

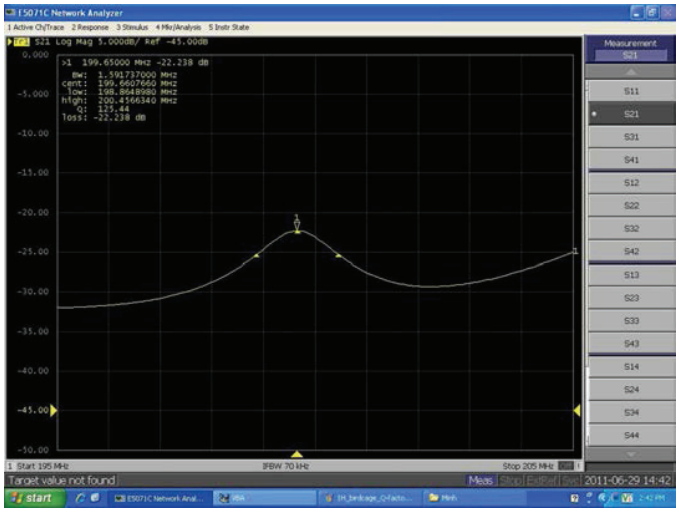

Figure I-15: *Measurement of Q factor using dual loop Pick-up coil. In this case, the Q factor of the same coil was 125.4*

By comparing these three methods of measurement, our results showed that the single port method gives us a slightly better Q factor than the values evaluated by the two other dual port-based methods. This noticeable difference may reveal the contribution of the inherent characteristics of the pick-up coil including the self-inductance and the resistive losses that translate into a subtle weakening of the Q factor. However, this subtle difference can be accounted for when different MRI resonators are characterized under the same conditions.

III.1.3 Improving the quality factor through capacitive redistribution [34]

As noted previously the Q factor is an important indicator of the sensitivity of a coil. When unloaded, Q_U is a measure of the losses within the resonant circuit under the best conditions by excluding the sample effects. Equally important, Q_L in presence of a sample acting as load accounts for the total losses induced within the circuit but also by the high conductivity nature of the biological tissues. The use of the best performing components (platinum-based low resistance conductor, small resistance and high-Q capacitors etc.) would enable marginal improvement of the unloaded Q_U yet prohibitively expensive. Alternatively, various strategies have been suggested to improve the loading effect of the sample on the Q_L of the RF structure coils. These improvements are mainly based on achieving a greater electrical balance of the structures through better symmetries. These improvements are principally aimed at reducing electrical hot spots via capacitive distribution throughout the resonator to balance the tuning [34] as well as achieving greater symmetrical attack to balance the matching [35].

The example below illustrates the benefits that can be achieved by a balanced scheme [35] starting from a capacitive matching circuit shown in figure I-16. For the sake of simplicity, we will consider that the sample is grounded and the hottest electrical point of the circuit is located in the part where the signal is injected (depicted by here V_+). In this case, the difference in potential between the sample and the coil is at its highest level in V_+.

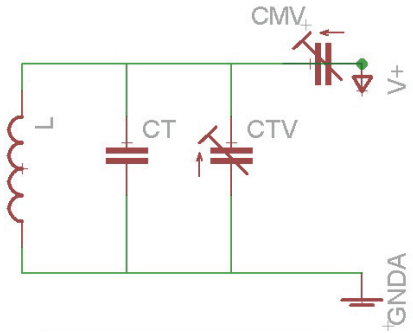

Figure I-16: *Electrical schematic of a classical coil*

This great spread will create a significant electrical unbalance throughout the coil that is directly experienced by the conductive sample illustrated in figure I-17.

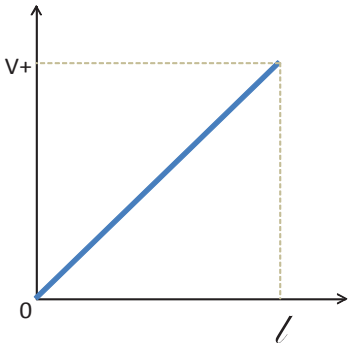

Figure I-17: *Voltage distribution along an unbalanced coil where l is the position along the coil wire. In one extremity the hot point depicted by V+ while the ground is on the other side of the wire*

where "*l*" is the length of the coil (from the GND side to V+ side). This difference in voltage may induce noticeable losses that could be modeled by the incorporation of equivalent circuit between the coil and the sample illustrated by figure I-18:

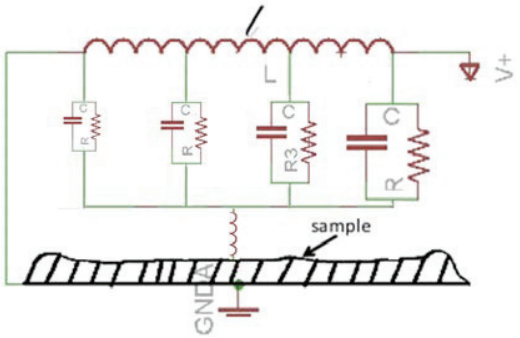

Figure I-18: *Electrical equivalent circuit of the MRI coil in presence of a conductive biological tissue. The lossy distributed capacitance and resistive losses induced by the conductive sample along the coil are greater in area with increased voltage. Importantly, eddy currents are also induced within the sample due to the varying current that translates into a counter self-inductance opposing the source of induction.*

These parasitic capacitors interfere with the coil altering its resonance to a lower frequency shift and inducing greater resistive and magnetic losses, which are all effects measurable by the Q_L. It is during this step that the coil requires a recalibration through a re-tuning of its resonance and a readjustment of its matching which in turn impacts on the effective sensitivity of the coil. The balanced matching scheme suggested by Murphy-Boesch and Koretsky [35] is illustrated in figure I-19.

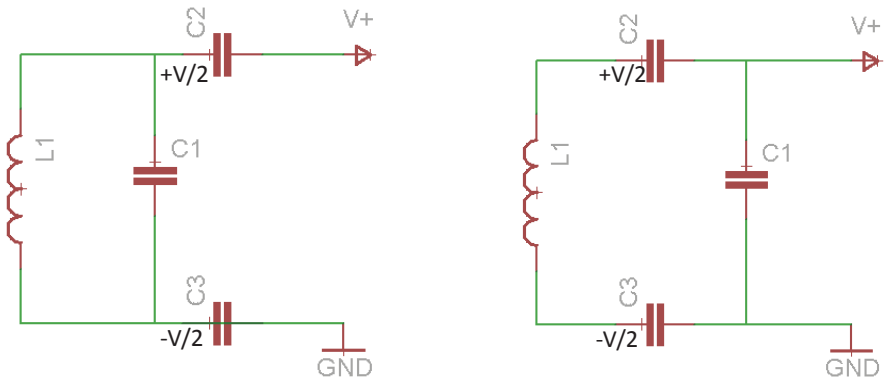

Figure I-19: *Distribution of matching capacitors*

The authors aimed at minimizing the influence of the coil-to-ground capacitive leaks using a balanced tuning circuit containing matching capacitors of equal size on both sides of the coil, as indicated in figure I-19. Since the matching capacitors are in series, their values must be approximately twice as large as the single matching capacitor of the standard circuit in figure I-18. This distribution of matching helped divide the voltage difference between the coil wire and the sample by a factor of 2 (se figure I-120) thereby reducing the lossy capacitance by a factor of 2.

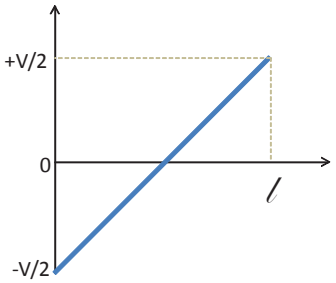

Figure I-20: *Voltage distribution along a balanced coil through a balanced, series-matched coil circuit. It should be noted that the hot spot has now halved compared to a conventional circuit*

In addition to the matching distribution, Decorps *et al.,* [34] has suggested a similar strategy but this time in the middle of the inductively coupled coil to distribute the tuning capacitors summarized by the equivalent circuit in figure I-21:

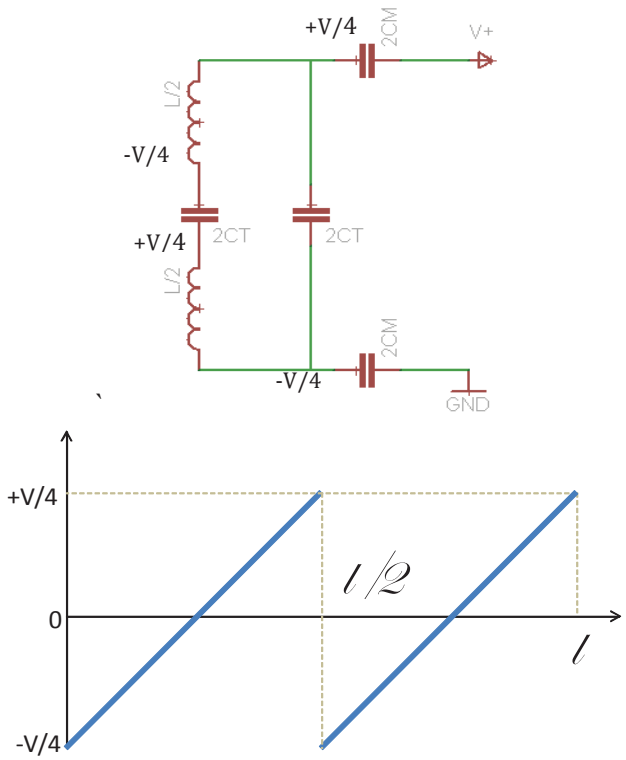

Figure I-21: *The capacitive coupled MRI resonator can be further balanced by combining the distribution of the tuning capacitors where the voltages at the coil leads in each side are nearly symmetrical are expected to be reduced significantly with respect to the ground. The voltage distribution along the series-tuned balanced circuit leads to a 4x voltage reduction along the wire compared to a conventional circuit.*

This reduction in voltage difference achieved by series tuning the coil can be a very effective method to reduce the dielectric heating of conductive samples

More capacitors on the coil could be tested to examine possible improvement of the quality factor. However, the number of capacitors could be limited depending on the shape and dimension of the coil. Additionally, the small nature of our sample can be affected by the position of the capacitors that can at times compromise the quality of the MRI images.

IV. Conclusion

In this chapter, we summarized several theoretical principles and concepts in coil characterization. We also described our in-house developed tool for our practical use. The

characterization is done systematically for all coils (if possible) that were used in this study.

References

[1] A. H. Affel, "Comcentric Conducting System," 1930.

[2] L. M. Angelone, A. Potthast, F. Segonne, S. Iwaki, J. W. Belliveau, and G. Bonmassar, "Metallic electrodes and leads in simultaneous EEG-MRI: specific absorption rate (SAR) simulation studies," *Bioelectromagnetics,* vol. 25, pp. 285-95, May 2004.

[3] K. B. Baker, J. A. Tkach, J. A. Nyenhuis, M. Phillips, F. G. Shellock, J. Gonzalez-Martinez*, et al.*, "Evaluation of specific absorption rate as a dosimeter of MRI-related implant heating," *J Magn Reson Imaging,* vol. 20, pp. 315-20, Aug 2004.

[4] J. W. Hand, Y. Li, E. L. Thomas, M. A. Rutherford, and J. V. Hajnal, "Prediction of specific absorption rate in mother and fetus associated with MRI examinations during pregnancy," *Magn Reson Med,* vol. 55, pp. 883-93, Apr 2006.

[5] J. P. Stralka and P. A. Bottomley, "A prototype RF dosimeter for independent measurement of the average specific absorption rate (SAR) during MRI," *J Magn Reson Imaging,* vol. 26, pp. 1296-302, Nov 2007.

[6] N. Makris, L. Angelone, S. Tulloch, S. Sorg, J. Kaiser, D. Kennedy*, et al.*, "MRI-based anatomical model of the human head for specific absorption rate mapping," *Med Biol Eng Comput,* vol. 46, pp. 1239-51, Dec 2008.

[7] C. M. Collins and M. B. Smith, "Signal-to-noise ratio and absorbed power as functions of main magnetic field strength, and definition of "90 degrees " RF pulse for the head in the birdcage coil," *Magn Reson Med,* vol. 45, pp. 684-91, Apr 2001.

[8] F. D. Doty, G. Entzminger, J. Kulkarni, K. Pamarthy, and J. P. Staab, "Radio frequency coil technology for small-animal MRI," *Nmr in Biomedicine,* vol. 20, pp. 304-325, May 2007.

[9] L. Darrasse and J. C. Ginefri, "Perspectives with cryogenic RF probes in biomedical MRI," *Biochimie,* vol. 85, pp. 915-937, 2003.

[10] D. I. Hoult and R. E. Richard, "The Signal-to-Noise Ratio of the Nuclear Magnetic Resonant Experiment," *Journal of magnetic resonance,* vol. 24, pp. 71-85, 1983.

[11] J. l. Mispelter, M. Lupu, and A. Briguet, *NMR probeheads for biophysical and biomedical experiments : theoretical principles & practical guidelines*. London; Hackensack, NJ: Imperial College Press; Distributed by World Scientific, 2006.

[12] F. Romeo and D. I. Hoult, "Magnet field profiling: analysis and correcting coil design," *Magn Reson Med,* vol. 1, pp. 44-65, Mar 1984.

[13] L. Fakri-Bouchet, L. Ch, and A. Briguet, "Measurements of the radiofrequency field in magnetic resonance coils," *Measurement Science and Technology,* vol. 9, p. 1641, 1998.

[14] S. Li, Q. X. Yang, and M. B. Smith, "RF coil optimization: evaluation of B1 field homogeneity using field histograms and finite element calculations," *Magn Reson Imaging,* vol. 12, pp. 1079-87, 1994.

[15] C. Guclu, G. Kashmar, A. Hacinliyan, and O. Nalcioglu, "An FEM approach for the characterization of the RF field homogeneity at high field," *Magn Reson Med,* vol. 37, pp. 76-83, Jan 1997.

[16] J. Murphyboesch, G. J. So, and T. L. James, "Precision Mapping of the B1 Field Using the Rotating-Frame Experiment," *Journal of Magnetic Resonance,* vol. 73, pp. 293-303, Jun 15 1987.
[17] S. Akoka, F. Franconi, F. Seguin, and A. Le Pape, "Radiofrequency map of an NMR coil by imaging," *Magn Reson Imaging,* vol. 11, pp. 437-41, 1993.
[18] E. K. Insko and L. Bolinger, "Mapping of the Radiofrequency Field," *Journal of Magnetic Resonance Series A,* vol. 103, pp. 82-85, Jun 1 1993.
[19] M. Alecci, C. M. Collins, M. B. Smith, and P. Jezzard, "Radio frequency magnetic field mapping of a 3 Tesla birdcage coil: experimental and theoretical dependence on sample properties," *Magn Reson Med,* vol. 46, pp. 379-85, Aug 2001.
[20] C. H. Cunningham, J. M. Pauly, and K. S. Nayak, "Saturated double-angle method for rapid B1+ mapping," *Magn Reson Med,* vol. 55, pp. 1326-33, Jun 2006.
[21] N. G. Dowell and P. S. Tofts, "Fast, accurate, and precise mapping of the RF field in vivo using the 180 degrees signal null," *Magnetic Resonance in Medicine,* vol. 58, pp. 622-630, Sep 2007.
[22] D. X. Wang, S. Zuehlsdorff, and A. C. Larson, "Rapid 3D radiofrequency field mapping using catalyzed double-angle method," *Nmr in Biomedicine,* vol. 22, pp. 882-890, Oct 2009.
[23] Y. L. V. Chang, "Rapid B1 mapping using orthogonal, equal-amplitude radio-frequency pulses," *Magnetic Resonance in Medicine,* vol. 67, pp. 718-723, Mar 2012.
[24] B. K. Li, F. Liu, and S. Crozier, "Focused, eight-element transceive phased array coil for parallel magnetic resonance imaging of the chest--theoretical considerations," *Magn Reson Med,* vol. 53, pp. 1251-7, Jun 2005.
[25] F. Ke, N. A. Hollingsworth, M. P. McDougall, and S. M. Wright, "A 64-channel transmitter for investigating parallel transmit MRI," *IEEE Trans Biomed Eng,* vol. 59, pp. 2152-60, Aug 2012.
[26] C. Wang and G. X. Shen, "B1 field, SAR, and SNR comparisons for birdcage, TEM, and microstrip coils at 7T," *J Magn Reson Imaging,* vol. 24, pp. 439-43, Aug 2006.
[27] A. Lutti, J. Stadler, O. Josephs, C. Windischberger, O. Speck, J. Bernarding*, et al.*, "Robust and fast whole brain mapping of the RF transmit field B1 at 7T," *PLoS One,* vol. 7, p. e32379, 2012.
[28] P. F. Van de Moortele, C. Akgun, G. Adriany, S. Moeller, J. Ritter, C. M. Collins*, et al.*, "B(1) destructive interferences and spatial phase patterns at 7 T with a head transceiver array coil," *Magn Reson Med,* vol. 54, pp. 1503-18, Dec 2005.
[29] X. Zhang, P. F. Van de Moortele, S. Schmitter, and B. He, "Complex B1 mapping and electrical properties imaging of the human brain using a 16-channel transceiver coil at 7T," *Magn Reson Med,* vol. 69, pp. 1285-96, May 2013.
[30] D. I. Hoult, C. N. Chen, and V. J. Sank, "Quadrature Detection Coils - a Further Square-Root-2 Improvement in Sensitivity," *Magnetic Resonance in Medicine,* vol. 1, pp. 171-171, 1984.
[31] D. I. Hoult, "The NMR receiver: a description and analysis of design," *Progr. NMR Spectrosc,* vol. 12, pp. 41–77, 1978.

[32] B. Roemer and A. W. Eldeistein, "NMR Imaging with multiple surface coils," 1989.
[33] D. Kajfez and E. J. Hwan, "Q-factor measurement with network analyzer," *IEEE Trans. Microwave Theory Tech.,* vol. MTT-32, pp. 666-670, 1984.
[34] M. Decorps, P. Blondet, H. Reutenauer, J. P. Albrand, and C. Remy, "An inductively coupled, series-tuned NMR probe," *Journal of Magnetic Resonance (1969),* vol. 65, pp. 100-109, 10/15/ 1985.
[35] J. Murphy-Boesch and P. A. Korestsky, "An in vivo NMR Probe Circuit for Improved Sensitivity," *J. Magn. Reson.,* vol. 54, p. 526, 1983.

Chapter II: The Birdcage coil

Introduction

The birdcage coil is the most used structure in MR and more particularly in 3D MRI because of its capacity to provide a large homogenous B1 field coverage at high frequencies. The concept of the birdcage was introduced by Hayes in 1985 [1] and appeared as a great improvement in MR probe designs. This structure can be used as a transmit coil or a transmit/receive coil, and can be easily improved (homogeneity and sensitivity) by using the quadrature mode [2].

In this chapter, the basic principles of the birdcage coil's design will be presented. To characterize the coil's homogeneity [3, 4], a simple dedicated color-mapping macro was developed in-house to be used with ImageJ software (described in the previous chapter).

To take advantage of the filling factor, several coils were developed to fit different samples and also to improve throughput of ex vivo scans (chapter 3).

I. High-pass birdcage and low-pass birdcage coils

I.1. Basic principles

The inducting element of the birdcage coil is composed of multiple parallel conductive segments that are parallel to the Z-axis, or the length of the coil. These parallel conductive segments are referred to as the rungs. These rungs interconnect a pair of conductive loop segments (rings) that make the structure look like a birdcage [1]:

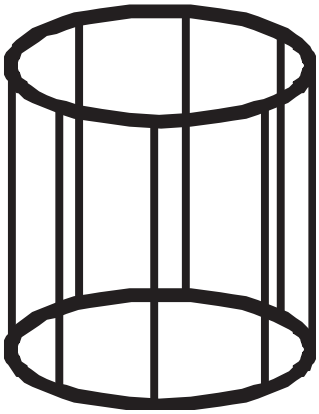

Figure II-1: *Inducting element of a birdcage coil*

In this study, we will focus on the two main types of the birdcage structure, high-pass and low-pass birdcage coils:

- High-pass birdcage: the capacitors are distributed on the two rings – in between adjacent rungs
- Low-pass birdcage: the capacitors are distributed at the mid-point of the rungs

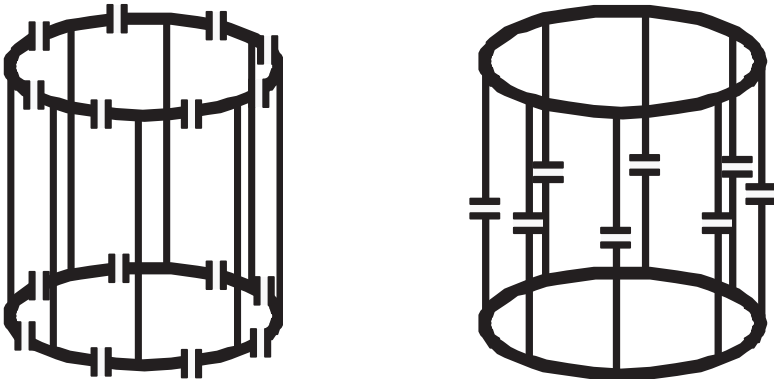

(a) (b)

Figure II-2: *Schematic of high-pass (a) and low-pass birdcage (b) coils.*

Essentially, the birdcage coil is a linear network of identical filter cells (figure II-3) connected together in a way that the last filter cell is identical to the first (figure II-4):

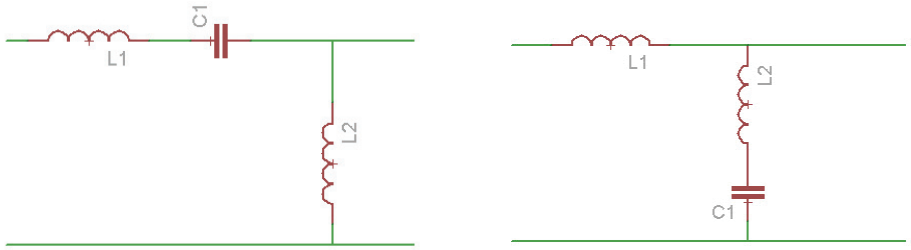

(a) (b)

Figure II-3: *Individual filter cell of birdcage coil: a) High-pass filter cell, b) Low-pass filter cell*

When excited by a current source, "waves" will propagate along the network. At particular frequencies, the waves combine constructively to create stationary states, corresponding to the resonant modes of the coil. In order to define the modes of the birdcage coil, we will use the method of equivalent circuit analysis [5]. Below is an example of an equivalent electrical circuit of a segment of a high-pass birdcage coil:

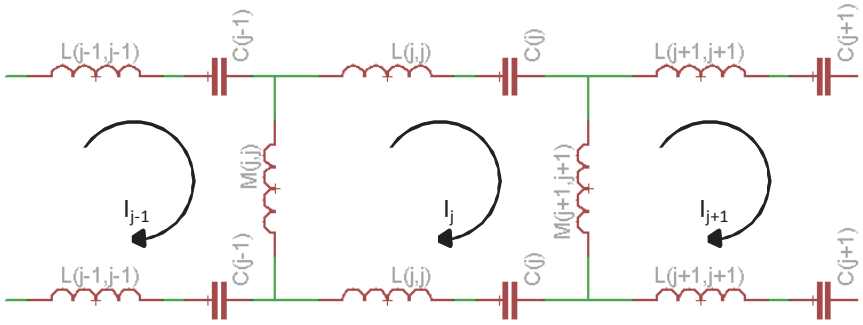

Figure II-4: *Equivalent electric circuit of segments of high-pass birdcage [5]*

In this figure, $M_{(j,j)}$ denotes the self-inductance of the jth rung, $C_{(j)}$ denotes the capacitance of the capacitor connected between the jth and $(j+1)^{th}$ rungs, and $L_{(j,j)}$ denotes the self-inductance of the conductors used to connect the capacitor.

To simplify the analysis, we assume $C_1 = C_2 = \cdots = C$, $L_1 = L_2 = \cdots = L$, and $M_{11} = M_{22} = \cdots = M$. Assume that the birdcage coil has N parallel rungs. In accordance with Kirchhoff's voltage law, for the loop consisting of the j^{th} and $(j+1)^{th}$ rungs and the jth capacitors, we have:

$$-i\omega M\left(I_j - I_{j-1}\right) - i\omega M\left(I_j - I_{j+1}\right) - 2i\omega L I_j + \frac{2i}{\omega C} I_j = 0$$

$$\mathbf{(j = 1, 2, \dots, N)} \qquad \text{(II-1)}$$

Where I_j denotes the current in this loop. This equation can be written as:

$$M\left(I_{j+1} + I_{j-1}\right) + 2\left(\frac{1}{\omega^2 C} - L - M\right) I_j = 0$$

$$\mathbf{(j = 1, 2, \dots, N)} \qquad \text{(II-2)}$$

Because of cylindrical symmetry, the current I_j must satisfy the periodic condition $I_{j+N} = I_j$. Therefore, the N linearly independent solutions (or modes) of equation (II-2) have the forms:

$$\left(I_j\right)_m = \begin{cases} \cos\frac{2\pi mj}{N} & m = 0,1,2, \dots, \frac{N}{2} \\ \sin\frac{2\pi mj}{N} & m = 0,1,2, \dots, \frac{N}{2} - 1 \end{cases} \qquad \text{(II-3)}$$

Where $\left(I_j\right)_m$ denotes the value of I_j in the m^{th} solution. The current in the j^{th} rung is then given by:

$$\left(\mathbf{I_j}\right)_m - \left(\mathbf{I_{j-1}}\right)_m = \begin{cases} \mathbf{-2\sin\frac{\pi m}{N}\sin\frac{2\pi m\left(j-\frac{1}{2}\right)}{N}} & \mathbf{m = 0, 1, 2, \dots, \frac{N}{2}} \\ \mathbf{2\sin\frac{\pi m}{N}\cos\frac{2\pi m\left(j-\frac{1}{2}\right)}{N}} & \mathbf{m = 0, 1, 2, \dots, \frac{N}{2} - 1} \end{cases}$$

(II-4)

To determine the characteristic (resonant) frequency for each solution, we substitute equation (II-3) into (II-2) and obtain

$$\mathbf{M\cos\frac{2\pi m}{N} + \left(\frac{1}{\omega^2 C} - L - M\right) = 0} \qquad \text{(II-5)}$$

From which we find [5]:

$$\mathbf{\omega_m = \left[C\left(L + 2M\sin^2\frac{\pi m}{N}\right)\right]^{-1/2}} \qquad \mathbf{m = 0, 1, 2, \dots, \frac{N}{2}} \qquad \text{(II-6)}$$

The highest resonant frequency occurs for the mode $m = 0$, from equation (II-3) and (II-4), we see that this mode has a constant current in the end-rings and no current in the rungs. This is often referred to as end-ring resonance, whose resonance is $\omega_m = \frac{1}{\sqrt{LC}}$. The second highest frequency with $m = 1$ is capable of producing uniform magnetic field and, thus, is useful for MRI [5]:

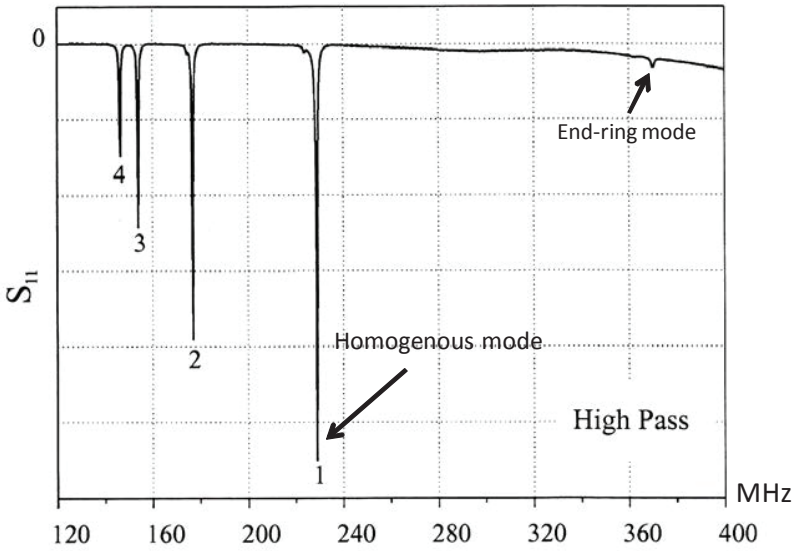

Figure II-5: *Example of resonant modes of a high-pass birdcage coil (8 rungs) [6]*

Applying the same method to the low-pass birdcage, we have the equivalent electrical circuit of a segment of a low-pass birdcage coil:

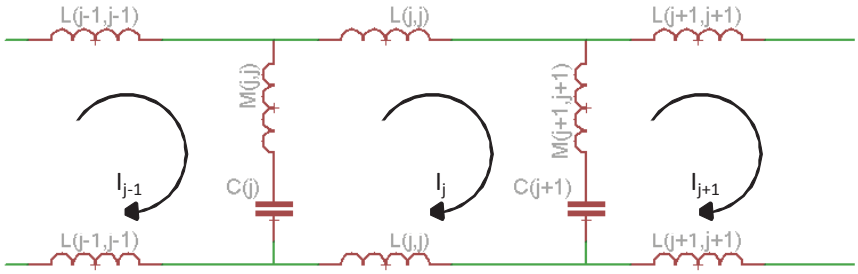

Figure II-6: *equivalent circuit of a segment of a low-pass birdcage coil [5]*

If we assume $C_1 = C_2 = \cdots = C$, $L_1 = L_2 = \cdots = L$, and $M_{11} = M_{22} = \cdots = M$. We obtain:

$$\left(\frac{1}{\omega^2 C} - M\right)\left(I_{j+1} + I_{j-1}\right) - 2\left(\frac{1}{\omega^2 C} - L - M\right) I_j = 0 \qquad (j = 1,2,\ldots,N) \qquad \text{(II-7)}$$

Its solutions are also given in equation (II.3) and the corresponding resonant frequencies are found as [5]:

$$\mathrm{F}\omega_m = \left[C\left(M + L/2\sin^2\frac{\pi m}{N}\right)\right]^{-1/2} \qquad m = 0, 1, 2, \ldots, \frac{N}{2} \qquad \text{(II-8)}$$

For a low-pass birdcage, the homogenous mode has the second lowest resonant frequency corresponding to $m = 1$ [5].

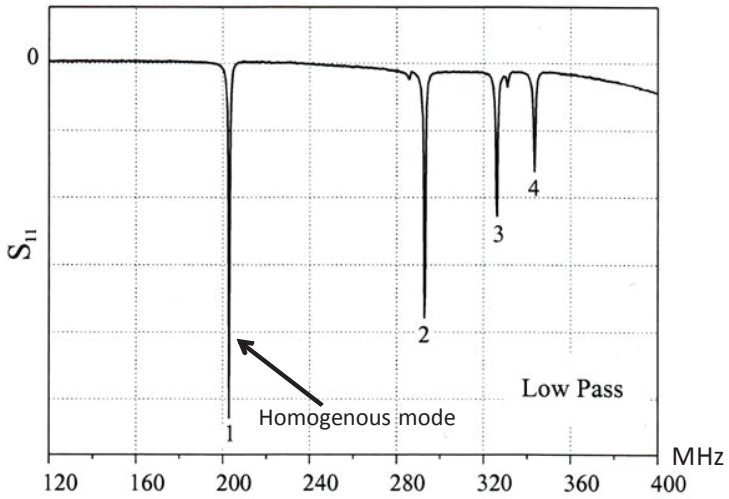

Figure II-7: *Example of resonant modes of a low-pass birdcage (8 rungs)[6]*

I.2. Pros and cons of each structure

Each structure described previously has its own advantages and inconveniences. In order to choose which structure to use in a particular case, we list here pros and cons of each structure:

Structure	High-pass birdcage	Low-pass birdcage
Pros	- The capacitors are distributed on the rings, far away from the center of the coil where the sample is normally positioned. No field distortions created by the capacitors. - The number of capacitors is double the number of the rungs. As described in the previous chapter, the more capacitors distributed on the coil, the less of electrical losses will be caused by the sample. - The homogenous mode has the second highest frequency. For the same size of coil, the capacitors have higher value compare to the low-pass birdcage. This allows designing larger coils or coils for higher field strength to be made.	- The number of capacitors is equal to the number of the rungs, therefore, if a filter cell is inhomogeneous compare to the rest of the coil, there's only one capacitor to be changed. This structure is easier to adjust the homogeneity
Cons	- The number of the capacitors helps to reduce the electrical losses but make the coil more difficult to adjust the homogeneity. When a filter cell is inhomogeneous, both of the capacitors need to be changed.	- The capacitors are distributed at the mid-point of the rungs, even though the capacitors used are non-magnetic, the field distortions are unavoidable. These distortions might create unwanted effect on the images. - The number of capacitors is equal to the number of the rungs. Compare to the high-pass structure, there are fewer of capacitors distributed on the coil, thus, there will be more of electrical losses created by the sample - The homogenous mode has the second lowest frequency. With large coils, the resonant frequency will be limited by self-resonance of the coil, therefore the dimension of the coil is limited or the field strength must be lower.

On the whole, the high-pass birdcage coil appears to have more advantages compared to the low-pass birdcage coil. But in the case of a small coil (mouse or rat head coil), the limit in dimension of the low-pass birdcage is not an inconvenience. For the problems due to field distortion caused by the capacitors, we can apply the following solution:

Instead of positioning the capacitors at the mid-point of the rungs, the capacitors will be positioned at each end of the rungs [7]:

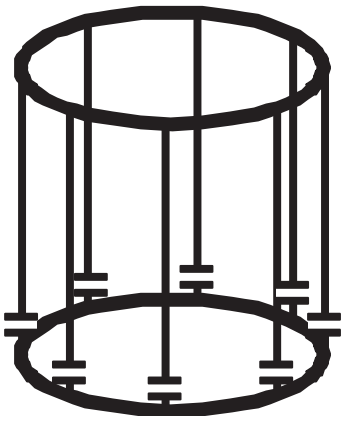

Figure II-8: *Placing the capacitor at one end of the rungs to avoid field distortions in the middle of the coil*

A solution has also been proposed to resolve the problem due to electrical loss is to distribute a capacitor at each end of the rung [6]. This solution reduces the electrical loss problem but makes it more difficult to adjust homogeneity. Thus, in designing the most suitable coil, we have to take into account the advantages and disadvantages of each solution.

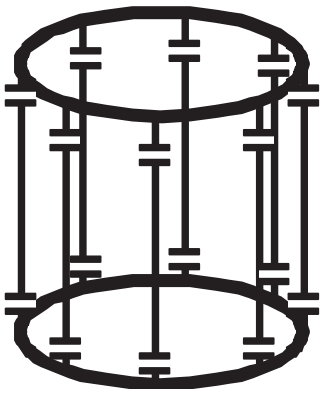

Figure II-9: *Placing two capacitors at each end of the rungs to avoid field distortions in the middle of the coil and reduce*

electrical losses [6]. But increasing the number of capacitors makes homogeneity adjustment more difficult

As demonstrated previously, the more rungs we have on the coils, the more resonant modes the coil has. The number of rungs decides the field profile of each mode (especially the homogenous mode).

II. Practical design of a birdcage coil (example of a low-pass birdcage)

As discussed previously, the low-pass birdcage structure has advantages for a small dimension coil. With our MRI system for small animals, especially for mice, the low-pass birdcage is our first choice for making homogenous volume coils for it lower number of capacitors, therefore, is of lower-cost and easier to adjust the homogeneity.

II.1. Resonant modes

For practical reasons, the coils were made using a cylindrical plastic support such as syringes, syringe holders, or polycarbonate tubes. In addition, the coil was made using copper strip (easy to measure width, length and be fixed on the coil support). Because the dimensions of the coils for small animal MRI are small, we chose to have 8 rungs on the coil:

- 4 rungs: the field is not homogenous enough
- 16 rungs: The space between the rungs becomes too narrow making the placement of the capacitors difficult and might create cross talk between the rungs. The increase in number of rungs leads to the use of more capacitors, increasing the cost in coil construction. The inductance of the coil is also increased; therefore, the value of the capacitors must be decreased considerably to make the coil resonate at the desired frequency. The smaller the value of the capacitors, the more difficult it is to adjust the homogeneity of the coil (caused by the imperfection of the capacitors during construction).
- 8 rungs: the space between the rungs is reasonable [7]. The field profile is also easy to adjust since we have a fewer number of capacitors.

Because the inductance of the coil is unknown, we first chose capacitors with random values so that the coil could resonate at random frequencies. Using a pick-up coil, we can observe the resonant modes of the coil with a Network Analyzer:

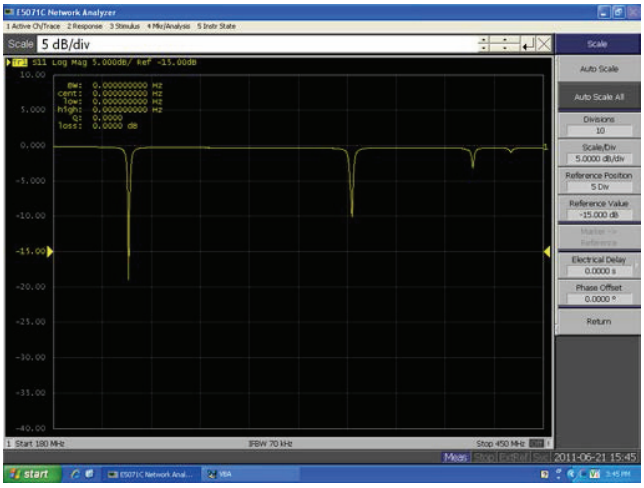

Figure II-10: *Low-pass birdcage modes using linear pick-up coil*

Figure II-11: *Low-pass birdcage modes using dual loop pick-up coil*

From the figures above, we can observe that the homogenous mode has the frequency at X MHz. For 7T, the coil must have the frequency for the homogenous mode around 300MHz, more precisely 301.17MHz for our system. Without the tuning and matching circuit, we would like to have the resonant frequency for the homogenous mode higher than the Lamor frequency of the system, about 310MHz to 330MHz because by adding tuning and matching capacitors to the coil's circuit, the frequency will shift to a lower value. Using equation II.8, we have:

$$\mathbf{2\pi X = \left[C_1\left(M + L/2\sin^2\frac{\pi m}{N}\right)\right]^{-1/2}} \qquad \mathbf{m = 1, N = 8} \qquad (\text{II-9})$$

And:

$$2\pi\times310\times10^{6}=\left[C_2\left(M+L/2\sin^2\frac{\pi m}{N}\right)\right]^{-1/2}\qquad m=1,N=8 \qquad \text{(II-10)}$$

From (II.9) and (II.10), we deduce:

$$\mathbf{C_1\left(M+L/2\sin^2\frac{\pi m}{N}\right)=\frac{1}{4\pi^2\times X^2}}\qquad \mathbf{m=1,N=8} \qquad \text{(II-11)}$$

$$\mathbf{C_2\left(M+L/2\sin^2\frac{\pi m}{N}\right)=\frac{1}{4\pi^2\times310^2\times10^{12}}}\qquad \mathbf{m=1,N=8} \qquad \text{(II-12)}$$

Dividing (II-12) to (II-11), we have:

$$\mathbf{\frac{C_2}{C_1}=\frac{X^2}{310^2}} \qquad \text{(II-13)}$$

$$\mathbf{C_2=\frac{C_1\times X^2}{310^2}} \qquad \text{(II-14)}$$

Usually, C_2 obtained is not a standard value; we can replace it with a standard one closer to its value. After replacing the capacitors, we will use the Network Analyzer and pickup coil to make sure the resonant frequency of the homogenous mode is close to the desired value.

II.2. Remote tuning and matching

Once the coil is made, it can be tuned and matched using different methods such as inductive coupling: in this case, the coil must be pre-tuned to 301MHz (replacing C2 with another value). And using a loop as shown in the following figure to transmit and pick-up signal:

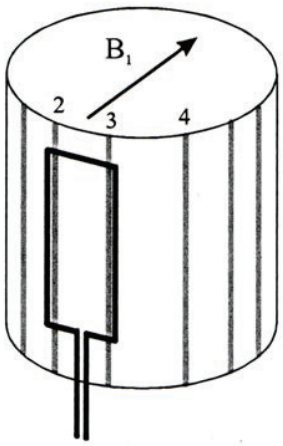

Figure II-12: *Birdcage coil with Inductive coupling [6]*

In this case, the tuning of the coil is difficult because for different samples, the frequency of the coil will shift to different values (depending on the loading of the sample); therefore, to optimize the MRI signal, the coil must be pre-tuned differently for each sample.

To make the tuning and matching of the coil easier, we prefer using capacitive coupling and for practical reasons, the method of remote tuning and matching was used for all of our coils.

The remote tuning and matching can be described by the following equivalent electrical circuit:

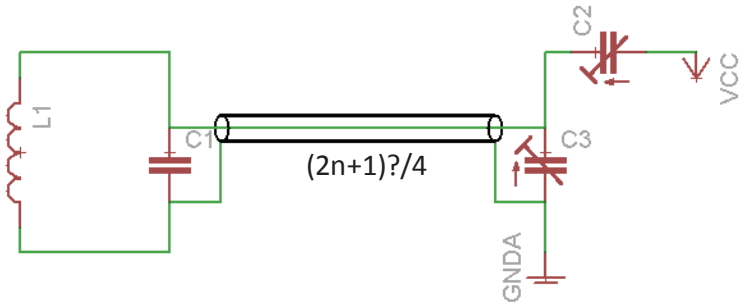

Figure II-13: *Equivalent electrical circuit of the remote tuning and matching network*

The coaxial cable used to connect the coil and the remote tuning and matching unit must be a quarter wavelength cable (as short as possible to avoid losses) to optimize signal transmission (described in previous chapter).

Using this coupling method, the coil doesn't need to be pre-tuned at the exact Lamor frequency for each sample. It only needs to be pre-tuned at a frequency higher than the Lamor frequency of the system (about 310MHz for 7T). Using the variable capacitors of the remote tuning and matching unit, the coil can then be tuned and matched at the desired frequency once the sample is placed in the coil and centered in the MRI system. This method introduces more losses compared to the inductive coupling method (caused by the quarter wavelength cable) and the inductance of the coaxial cable also must be accounted for (another reason to have the length of the cable as short as possible) but the tuning and matching of the coil are considerably easier. The remote tuning and matching unit can also be interchanged between different coils, thus reducing costs.

II.3. Birdcage coil with balanced signal feeding

A traditional birdcage coil with only one point to transmit and receive signal has a brightening effect on the attacking point (hot spot) (figure II-15 a). One solution to reduce this effect is to redistribute higher capacitance to the rung on the opposite side of the coil. This adjustment may take several attempts to have a good range of capacitors to balance the signal intensity.

Another solution for this problem is to use a distributed signal feeding instead of an attack on only one point, the transmit signal will also be distributed on the opposite side of the coil. We need to take into account that the opposite side of the feeding point will be 180^{o} different in phase in homogenous mode [6]. Therefore the transmit signal on this side must be 180^{o} (the current is in the inverted direction) different compared to the feeding point [8]. To satisfy this condition, we can connect these two points using a half wavelength coaxial cable ($\lambda/2$), because the transmit signal will travel through the $\lambda/2$ from the feeding point and at the end of the cable the phase difference will be 180^{o} and match with the phase of the second point (figure II-14).

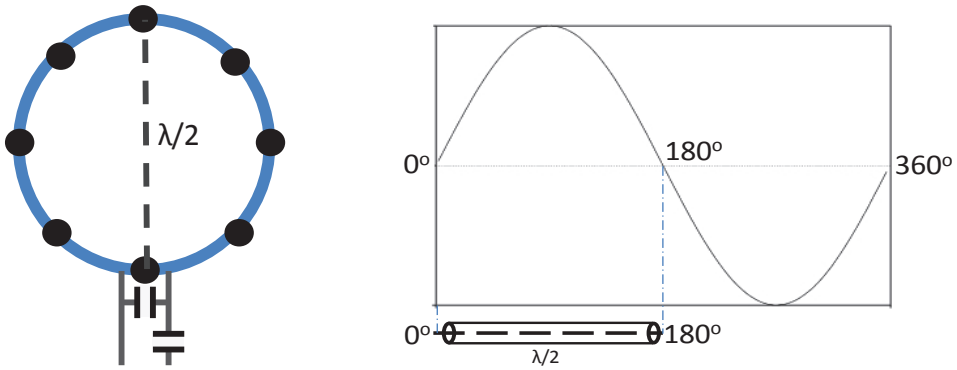

(a) (b)

Figure II-14: *a) Balanced attack with λ/2 coaxial cable. b) Phase difference at 2 ends of a λ/2 coaxial cable.*

This distribution of signal feeding shows a clear improvement in getting a balanced signal and reducing the hot spot effect (figure II-15 b). This is not only a low cost solution in financial terms but also reduces time and effort consumed to redistribute the capacitors.

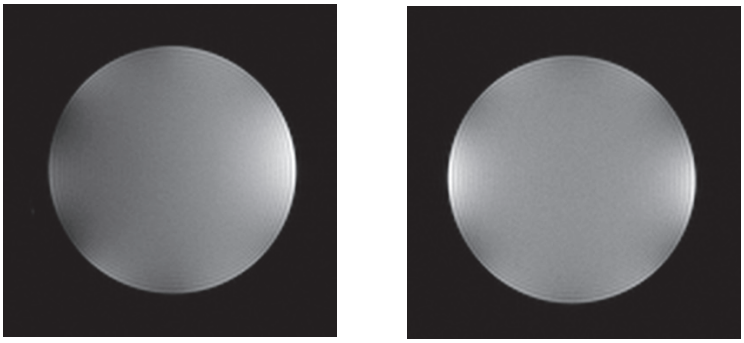

(a) (b)

Figure II-15: *a) Image from Gd-DTPA phantom of a birdcage with one point attack and unbalanced signal intensity. b) Image from Gd-DTPA of a birdcage with distributed attack shows a clear improvement in homogeneity and reducing the hot spot effect.*

II.4. Circular polarization effect

The ease of employing the circular polarization effect on a birdcage coil to gain homogeneity and improve the signal to noise ratio is another advantage of this structure [2]. For a traditional linear birdcage (high-pass in this example), the magnetic vector (blue arrow in the figure II-18) at instant t=0 will be divided to 2 smaller components

which turn in opposite directions. Because of this, the transmitted power will be divided by 2, therefore making the coil less efficient in its transmitting mode [6].

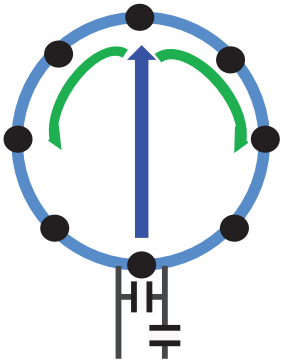

Figure II-16: *The magnetic vector of a traditional linear birdcage is divided by 2 and makes the coil less efficient during the transmitting mode*

In circular polarization mode, the power will be transmitted to the coil through 2 points (2 tuning and matching networks needed):

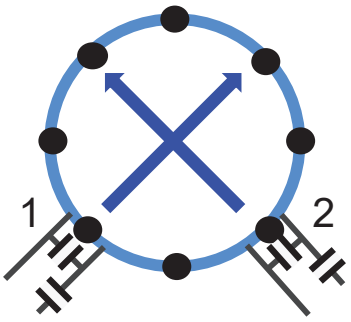

Figure II-17: *2 tuning and matching networks needed for the birdcage coil to work in circular polarization mode*

In this case, at time 0, the phase of the signal feeding point on the channel 1 is 0^{o} and the one on the channel 2 is 90^{o}. To force the magnetic vectors of each channel to turn in the same direction and also to reduce the hot spot effect, the method of distributed signal feeding can be used for each channel. There will be two $\lambda/2$ coaxial cables to connect the signal feeding point of each channel to its opposite side of the coil [7].

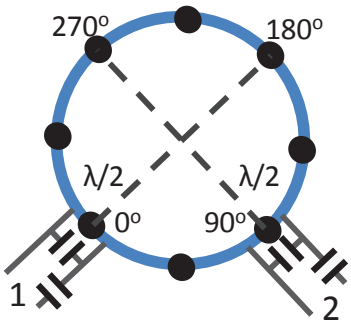

Figure II-18: *two λ/2 coaxial cables were used to balance the attack of each channel and also to force the magnetic vector to turn in one direction (0^o -> 90^o -> 180^o -> 270^o).*

Now that the two magnetic vectors will turn in the same direction and the phase difference is 90^o, if we call the magnetic vector generated by channel 1 is $\vec{a}$ and channel 2 is $\vec{b}$, and if all the capacitors are perfectly equal and perfectly positioned on the coil, we would have: $\vec{a} = \vec{b}$. We can now calculate the total magnetic vector created by 2 channels as follows:

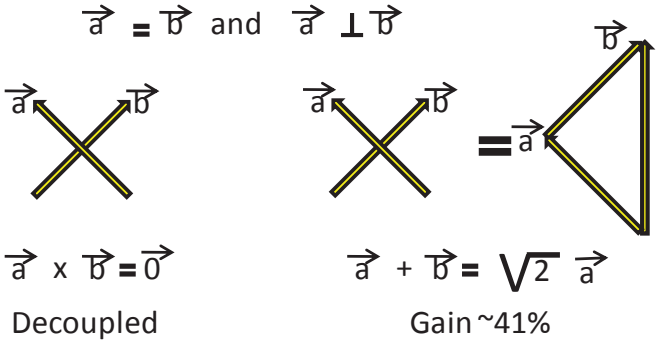

Figure II-19: *Total magnetic vector created by the two channels of a circular polarized birdcage coil*

From the calculation, we can see that if the two vectors were perfectly decoupled (phase difference is 90^o) and their magnitude are perfectly equal, we can gain 41% in signal intensity [2]. But we cannot have all the capacitances perfectly equal or perfectly positioned, and the rungs of the coil cannot be perfectly spaced, the phase difference between the two magnetic vectors will not be 90^o, and thus are not perfectly decoupled and also their magnitude are not perfectly equal. To adjust the phase difference between the two channels, we can place 2 variable capacitors as shown below:

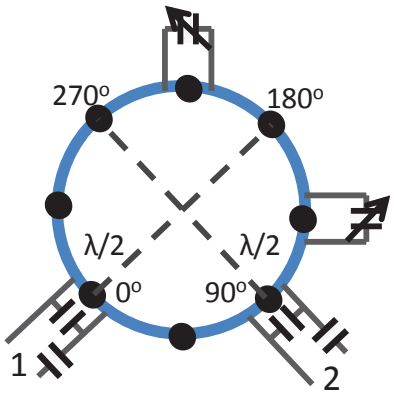

Figure II-20: *Two variable capacitors can be used to adjust the phase difference between the two channels*

By adjusting the value of the variable capacitors, we change the phase of the signal passing through the rungs of the coil and therefore adjust the phase difference between the two channels. Because the magnitude of the two vectors usually is not equal, the gain of 41% will almost never be obtained.

II.5. Quality factor (Q factor) measurement

After adding the tuning and matching unit to the coil, the first parameter that can be measured is the Q factor. Using one of the methods described in the previous chapter, we measured the Q factor of the coil unloaded and loaded to estimate the dielectric loss due to the sample:

- Q factor unloaded (Q_U)
- Q factor loaded (using a water sample) (Q_L)

The losses created by the sample can be estimated as [8]:

$$\textbf{\textit{Sample loss}} = 1 - {Q_L}/{Q_U} \qquad \text{(II-15)}$$

II.6. Homogeneity mapping

Once we determine the Q factor, we can use the imaging method described in previous chapter to characterize the homogeneity of the coil (with a 35ml syringe of Phosphate Buffered Saline – PBS doped with Gd-DTPA 5mM) using a gradient echo sequence with the following parameters:

- 3D sPGR - 250um isotrpic
- TE/TR: 10/50ms
- FA: 45
- NAv: 2
- BW: 195Hz/Pixel
- Matrix and FOV varied depending on dimension of the coil and the phantom.

After acquiring phantom images, we used the color mapping macro (see chapter I) to map the intensity of the signal of the field inside the coil and therefore map its homogeneity. We can improve the homogeneity of the coil by redistributing the value of the capacitors on the coil (lower capacitance for brighter spot and higher capacitance for darker spot).

III. The design of homogenous coils for whole mouse body in-vivo MRI

III.1. Coil design

Our projects require the study of the bio-distribution of contrast agents throughout the mouse body. For these situations, a homogenous volume coil with a large RF magnetic field coverage is needed. The birdcage structure is our premier choice because of its capacity to provide a large homogenous volume. The choice between low-pass and high-pass was done by analyzing the advantages and disadvantages of each structure. As described previously for large structure coils, the low-pass birdcage uses very small value capacitors at high field (7T, 300MHz), thus the homogeneity adjustment (redistributing the capacitors) becomes extremely difficult. Another disadvantage of the low-pass birdcage is that the capacitors are placed in the middle of the rungs and very close to the mouse body. These capacitors might create B1 field distortion that could be seen on the images. The solution to fix this problem is to place the capacitors on one side of the rungs (close to one ring as described earlier). But for longer coils (for example a mouse body coil), this solution will create another problem is the homogeneity along the length of the coil. Here's an example of a long low-pass birdcage (can cover the length of an adult mouse body) with the capacitors placed on one side of the rings:

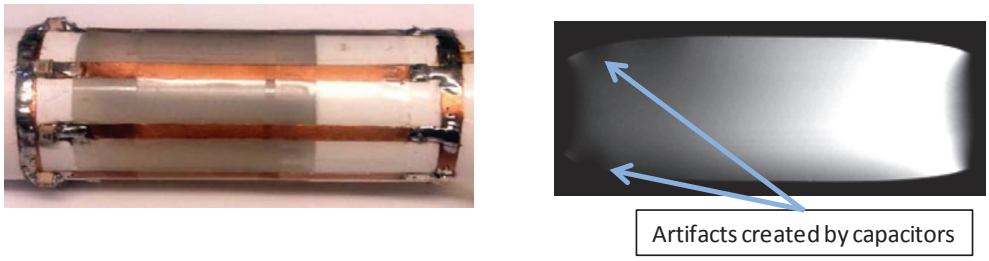

(a) (b)

Figure II-21: *a) Example of a long low-pass birdcage that could cover the whole mouse body. b) The images acquired with a Gd-DTPA phantom showed that the coil is inhomogeneous in the Z direction (along the length of the coil) and the artifacts created by the capacitors can be seen on the images.*

The value of the capacitors used on this coil is 1pF, the smallest value available in the lab thus there's no possibility to adjust the homogeneity in the axial direction of the coil. Because the structure is not homogenous in the Z direction (along the body of the mouse), it doesn't meet the requirements for whole body mouse MRI. As mentioned previously, one solution to solve this problem of homogeneity is to redistribute the capacitors on two sides of the rungs (figure II-9) [6]. But this solution is equivalent to having a high pass birdcage coil with smaller value capacitors thus more difficult to adjust the homogeneity. After assessing all these issues, a high-pass birdcage is our choice for the whole body scan. As the average length of an adult mouse body is about 6.5cm, the body coil must have a length that can cover this distance. The accessible diameter (AD) of the coil must be large enough for the mouse to be slide in or out easily, a pre-existing holder is available which has a 33mm AD and 38mm outer diameter (OD) (this will be the inner diameter of the coil – ID) and satisfies the conditions required. After placing the rungs (8 rungs equally spaced) and rings (2 end rings and 1 ground ring) using copper strips, the structure will look as follows:

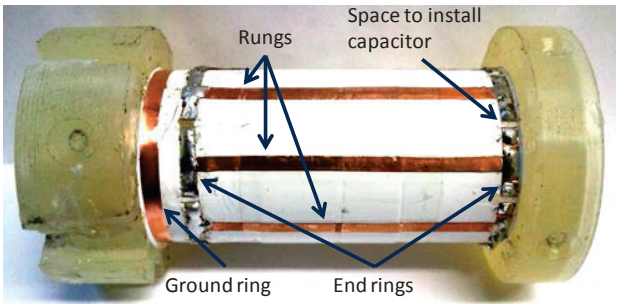

Figure II-22: *High-pass birdcage without capacitors installed*

Once the coil was constructed, we installed capacitors of 6.2pF on the coil to determine the resonant modes of the coil. Using a transmit-receive pickup coil, we could observe the resonant modes of the coil (4 modes for an 8 rung coil):

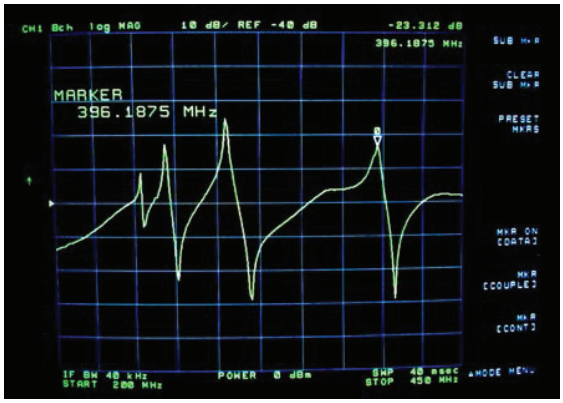

Figure II-23: *Four resonant modes of the coil with 6.2pF capacitors installed*

In this figure, we see that the homogenous mode (the highest resonant frequency) was at 396MHz. Without connecting the coil to the tuning and matching network, we need the homogenous mode to resonate at a frequency between 310MHz and 330MHz as mentioned earlier in this chapter. Taking 310Mhz as lower limit of frequency and using equation II.14, we can deduce the value of capacitors needed:

$$\mathbf{C_2 = \frac{6.2 \times 396^2}{310^2} = 9.98\ (pF)} \qquad \textbf{(II-16)}$$

With the 6.2pF installed, we need to add about 3.8pF on each of the capacitors to make the coil resonate at 310MHz. The only existing standard value of capacitors available in the lab that is close to 3.8pF is 3.0pF; we will use this value instead. With 3.0pF added, the homogenous mode is now shifted to:

$$\mathbf{F = \sqrt{\frac{6.2 \times 396}{9.2}} = 326\ (MHz)} \qquad \textbf{(II-17)}$$

326MHz is in the desired value range (in between 310MHz and 330MHz) and this frequency was confirmed by using a pickup coil and Network Analyzer:

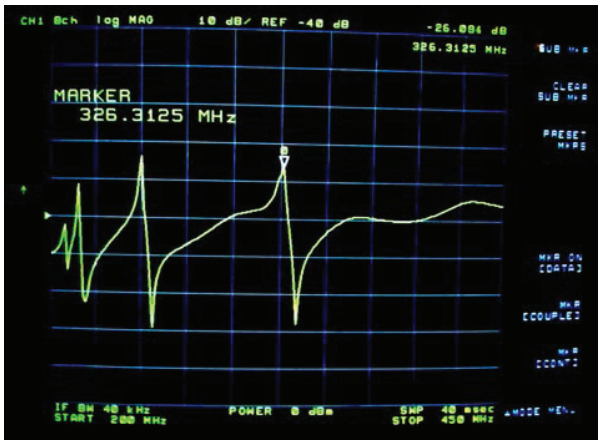

Figure II-24: *Homogenous modes of the coil shifted to 326MHz with 9.2pF capacitors installed*

As demonstrated previously, a circular polarized birdcage could help to gain about 41% of signal to noise ratio (SNR). We would like to take advantage of this configuration for our coil. In this mode, the coil will have 2 signal feeding points and the phase difference between these 2 points is 90^{o}. The advantage of the signal feeding distribution will also be used. The next step is to connect each point of signal feeding to a point on the opposite side of the coil using $\lambda/2$ coaxial cables:

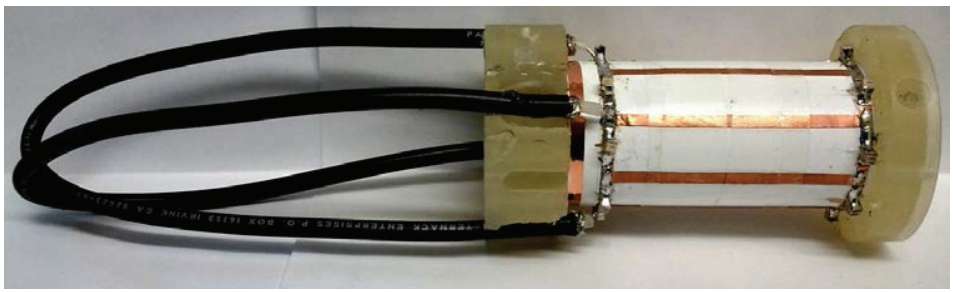

Figure II-25: *Each signal attacking point is connected to its opposite point by a $\lambda/2$ coaxial cable*

As the coaxial cable is made of conductive material, it has its own inductance. This inductance will be added to the inductance of the coil and therefore shift the frequency of the coil to a lower value than the previously determined value. This lower frequency was measured at 321.5MHz (compare to the previously determined 326MHz):

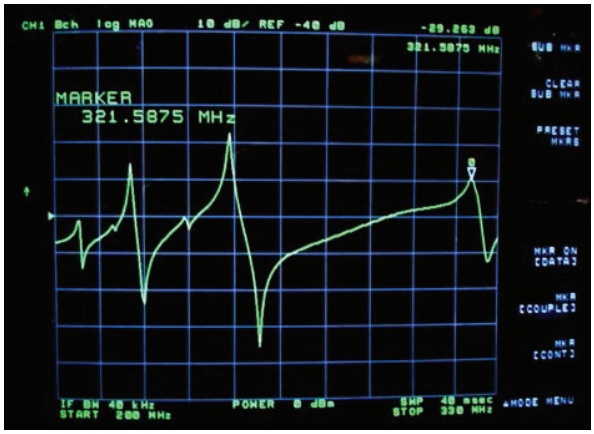

Figure II-26: *Homogenous mode shifted to a lower frequency (321.5MHz) because of the inductance induced by the coaxial cables.*

Each signal feeding point of the coil will be connected to a tuning and matching network. Each channel of the coil will be tuned to a frequency close to 300MHz (Lamor frequency at 7T) and matched to 50Ω. As explained previously, the two channels won't be completely decoupled (phased difference other than 90^{o}) because of the imperfection of the components. To measure the decoupling factor between the two channels, we will use the Network Analyzer. The RF signal will be transmitted through one channel and the returned signal will be measured through the other channel (S12 mode). Without any adjustment, the decoupling factor of the coil is:

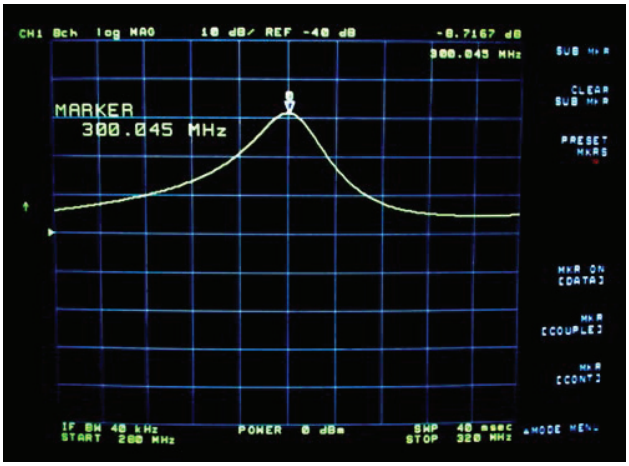

Figure II-27: *Measurement of decoupling factor of the coil using Network Analyzer*

As observed, the decoupling factor between the two channels is only -8.7dB. As is standard for commercially available coils, the two channels can be considered as

decoupled if the decoupling factor is better than -15dB [9]. To adjust the decoupling factor, we must be able to adjust the phase difference between the two channels. To do this, we use 2 variable capacitors (trimmer) installed as shown in figure II-28. By changing the value of these two trimmers, we change the phase of the 2 rungs where the trimmers were installed. The closer the phase difference is to 90°, the better decoupling factor we can attain. The iteration to have the best decoupling factor is:

- Turn one trimmer in one direction and check on the Network Analyzer if the decoupling factor improves, if not, turn it in the opposite direction till we reach the optimized value. Repeat the steps with the second trimmer.
- Retune the two channels to 300MHz and re match them to 50Ω.
- Measure the decoupling factor again, if needed, repeat from step one till the optimized decoupling factor is obtained.

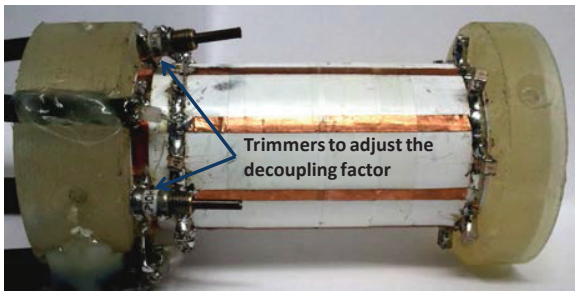

Figure II-28: *Two trimmers were used to adjust the decoupling factor between the two channels of the coil.*

Following the steps mentioned previously, we could obtain a decoupling factor with an unloaded coil that is about -19dB. Using a perfused mouse body to measure the loaded decoupling factor, we find it is about -17.6dB. The decoupling factors (unloaded and loaded) are beyond the requirement of -15dB.

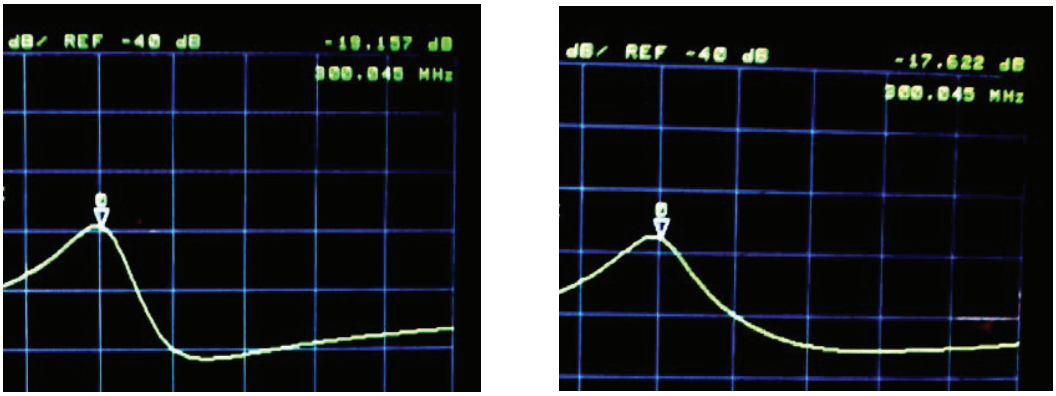

(a) (b)

Figure II-29: *a) Unloaded decoupling factor. b) Loaded decoupling factor.*

The next step is to verify the homogeneity of the coil. To do this, we use a cylindrical phantom filled with 5 mM Gd-DTPA that fits well in the coil (figure II.30).

(a) (b)

Figure II-30: *a) cylindrical plastic holder to characterize the coil's homogeneity. B) Holder fits perfectly in the coil.*

The images from the phantom were acquired using a sPGR sequence with the following parameters:

- 3D sPGR: 250um isotropic
- FOV: 9.60x3.20x3.20 cm
- Matrix: 384x128x128
- TE/TR: 5.1/18 ms
- FA: 45o
- Nav: 2
- Scanning time: 10 minutes

Using the signal intensity color mapping macro developed for ImageJ (see chapter I), we can map the homogeneity of the coil:

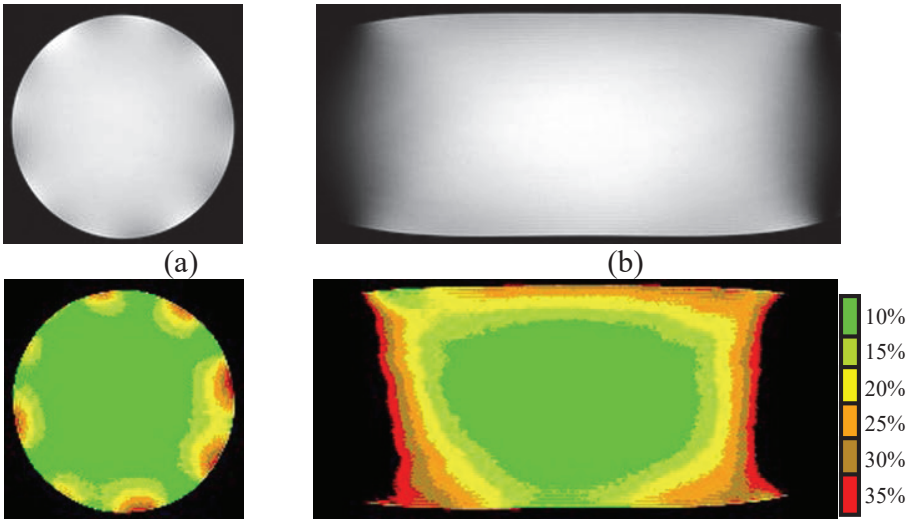

Figure II-31: *a) Cross slice (axial direction) of MRI image acquired from phantom. b) Slice along the length of the phantom (sagittal direction). c) and d) Signal intensity color map of corresponding phantom image. Green area has a signal intensity of 10% of different compared to the center of the coil (homogenous area) [3, 4].*

Even though the homogeneity of this coil cannot cover the whole adult mouse body (especially in the Z direction - along the length of the coil), for a qualitative study, the non-homogeneity of the coil is acceptable.

The effect of the sample loss was also characterized by measuring the unloaded and loaded quality factors which have the values of: 145 and 112.5 respectively (figure II-32).

From the measured values of Q factor, we can deduce the sample loss is about (equation II-15):

$$Sample\ loss = 1 - {Q_L}/{Q_U} \approx 0.224\ (\sim 22.4\%)$$

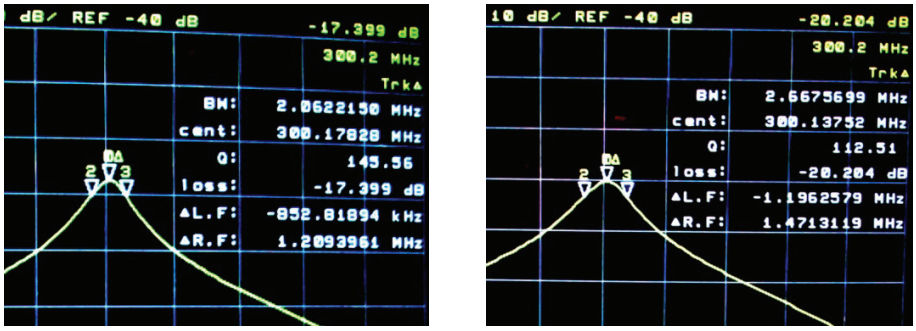

(a) (b)

Figure II-32: *a) Unloaded Q factor measurement. b) Loaded Q factor measurement*

The last step in coil characterization is to measure the CP gain. Using the same phantom and MRI sequence used previously to characterize coil homogeneity; we first acquire images of the phantom from each channel separately and from the CP mode:

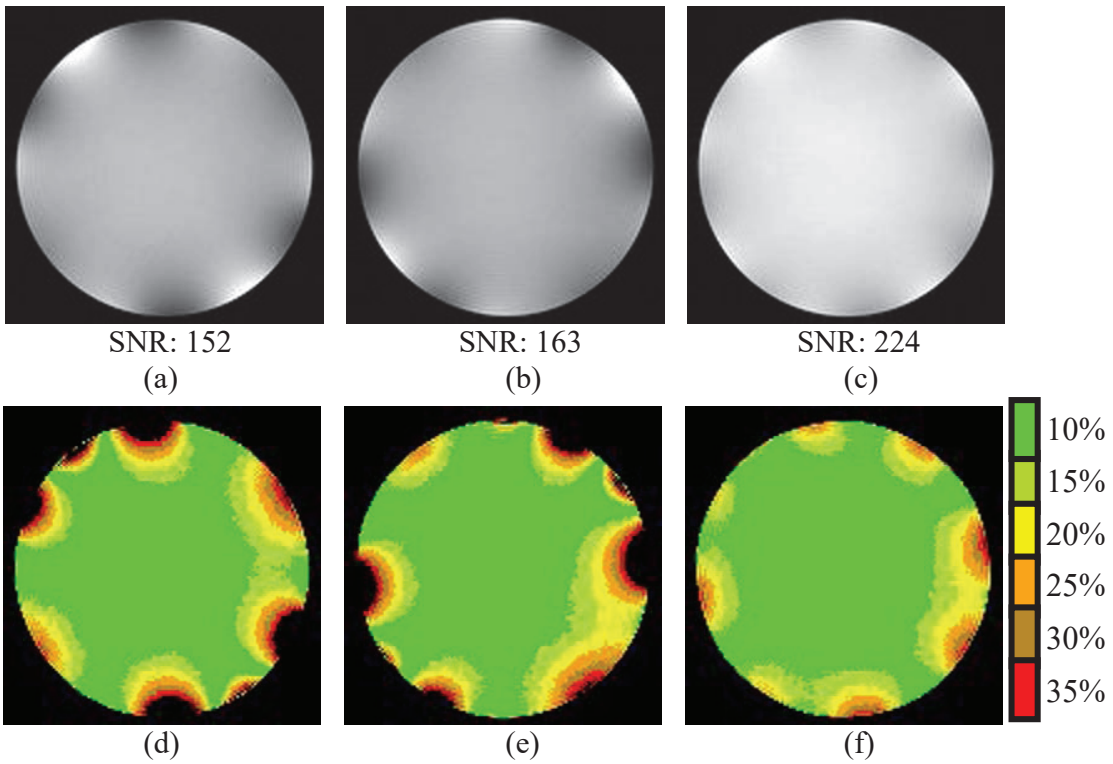

SNR: 152 SNR: 163 SNR: 224

(a) (b) (c)

(d) (e) (f)

Figure II-33: *a) channel 1 phantom image. b) channel 2. c) CP mode. d), e) and f) corresponding colored signal intensity map*

The measurement of SNR (mean of the signal/standard deviation of the noise) shows that the CP mode gives the SNR gain of 37%. We also can observe from the signal color maps that the CP mode has a better homogeneity (the effect of hot spots is less obvious and the green area is larger).

We can also observe that the gain in CP mode doesn't reach the theoretical value of 41% because of the unbalancing of the two channels and also the decoupling factor at -17dB is not entirely perfect.

III.2. Application to whole mouse body in-vivo MRI

This coil has been used in the lab to scan the whole mouse body as it was designed for. The mouse will be strapped on the sled to avoid movement and installed in the coil without any obstruction. The coil has proven its capacity to acquire MRI from "head to toe", see Figure II.34 of a whole adult mouse body:

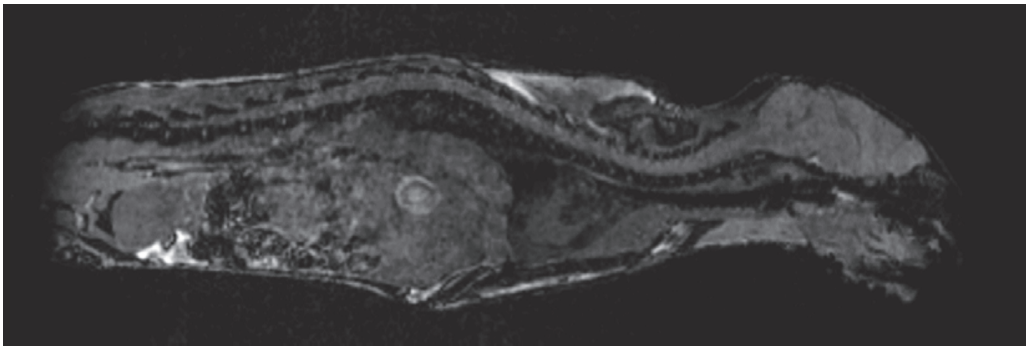

Figure II-34: *Image of a mid-section in sagittal direction of a mouse acquired using the whole body coil*

One of the projects that has taken advantage of this coil is to study the bio-distribution of contrast agents in the mouse body. The findings of this project were presented at ISMRM 2010 (Stockholm, Sweden) by our lab member Lindsay K. Hill:

Silver Nanoparticles Functionalized with High Gadolinium Chelate Payload As Effective *In Vivo* T1-Brightening Contrast Agents

Lindsay K Hill[1], Talha S Siddiqui[2], Dung Minh Hoang[1], Susan Pun[1], Marc A Walters[2] and Youssef Z Wadghiri[1]
[1]Department of Radiology, NYU School of Medicine, New York, NY, USA
[2]Department of Chemistry, New York University, New York, NY, USA

IV. *in vivo* mouse head imaging

MRI is the most efficient and non-invasive tool for in vivo studies, especially of the brain, which is very sensitive to any external perturbation. Pre-clinical studies (on small animals, more specifically on mice) with the aim of developing sequences, protocols, drug tests etc. are also important. As the mouse brain is about 3000 times smaller than the human brain, there is a tremendous need to develop instruments and MRI protocols that allow the acquiring of high-resolution images with better SNR. In our lab, we've been

working on developing coils that allow us to undertake multiple projects to study the anatomy of the mouse brain in neurodegenerative diseases such as Alzheimer's disease, or brain tumors. Among these projects, we have our focus on the study of Manganese distribution in the mouse olfactory bulb. As the region of interest is very small, we seek to design a coil that can cover this part of the mouse brain efficiently.

IV.1. In-house developed saddle coil

When designing a coil for a mouse head MRI, we must fulfill the following requirements:

- The coil must fit the mouse head as closely as possible to take advantage of the filling factor
- The homogeneity of the coil must cover the studied region of interest

This will allow us to scan in vivo a mouse head in less than 2h30minutes with 100µm isotropic resolution.

One of the simplest structures to design is a volume coil such as the Helmholtz coil. A Helmholtz coil is composed of 2 identical wire loops placed parallel to each other at a distance equal to the radius R of the loops (figure II-35) [10]:

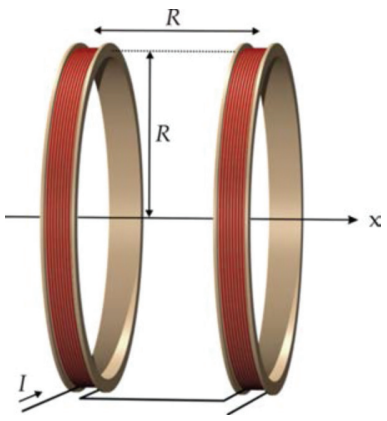

Figure II-35: *Helmholtz coil*

This coil is able to provide a very homogenous magnetic field in between the 2 loops (figure II-36). The limitations of the Helmholtz coil is the length of the coil cannot extend further than the radius of the loops and also the studied object must be positioned orthogonally to the direction of the B0 field which is not practical in most of the cases where the gradient coil is small.

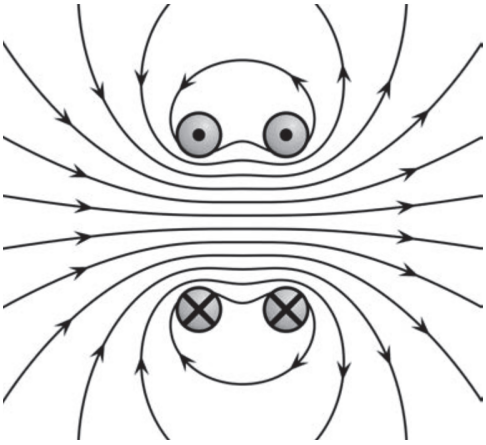

Figure II-36: *The magnetic field in between the 2 loops of a Helmholtz coil is very homogenous*

The saddle coil that is a deviation of the Helmholtz coil will allow us to bypass these limitations. The saddle coil can be constructed using one wire placed on a cylindrical support as following [11, 12]:

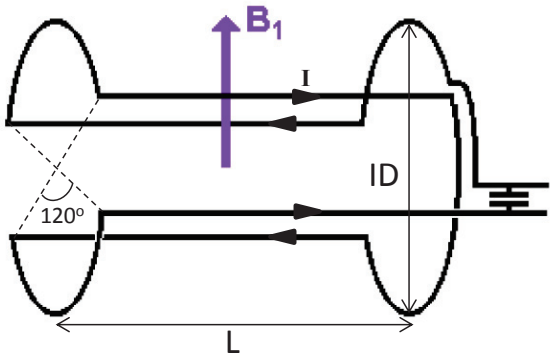

Figure II-37: *Saddle coil structure*

With this structure, we can make the diameter of the coil to best fit a mouse head (take advantage of the filling factor) and also extend the length of the coil to cover the region of interest (the whole brain normally). Thus, a coil was made in-house to use in in vivo MRI using a cylindrical plastic support which has an outer diameter of 21mm (ID of the coil), AD 19mm and the length of the coil is 22mm. To reduce the dielectric losses caused by the sample, 8 capacitors of 15pF were distributed on the coil (at the corner of each loop). The coil is connected to a remote tuning and matching network through a quarter wavelength coaxial cable.

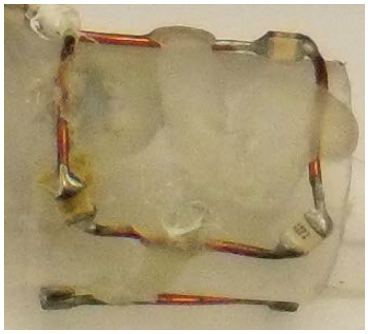

Figure II-38: *in-house developed saddle coil for mouse head imaging*

The homogeneity of the coil was characterized using a 12ml syringe filled with 5mM Gd-DTPA. To see if the homogeneity of the coil could cover the studied region of interest (the mouse brain), we scanned in vivo a mouse head with a known field of view (FOV). After acquiring the images both from the phantom and the mouse, the images were resized to the dimension of the FOV used. Then the image from the slice that passes through the largest part of the mouse head (normally placed at the center of the coil) will be superimposed on top of the color-mapped image of the phantom (also the middle slice). We obtained the following results:

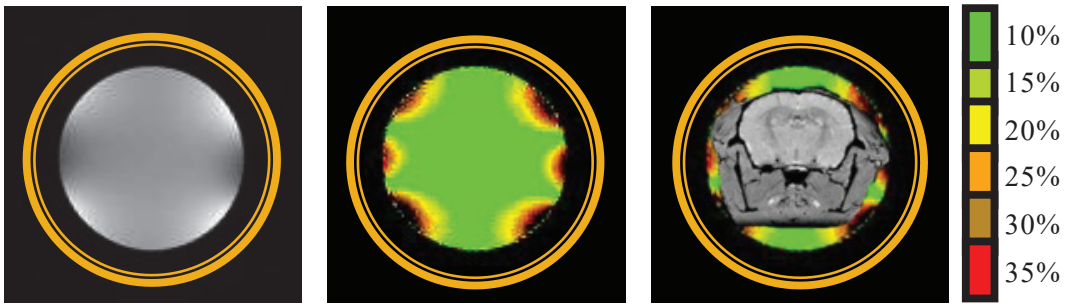

(a) (b) (c)

Figure II-39: *a) image from phantom (the circle simulates the position of the coil). b) Color mapped image. c) Superposed image of a mouse head.*

From the figure II-39 c, we can conclude that the homogeneity of the coil doesn't cover the whole brain of the mouse and need to be improved.

IV.2. Commercially available coil: Doty CP litz coil

In order to have improved homogeneity to cover the mid-section part of the mouse brain, a commercially available coil was purchased from Doty Scientific (http://www.dotynmr.com/). This coil has an ID of 28mm, AD of 26mm and L of 29mm, which could easily fit an adult mouse head:

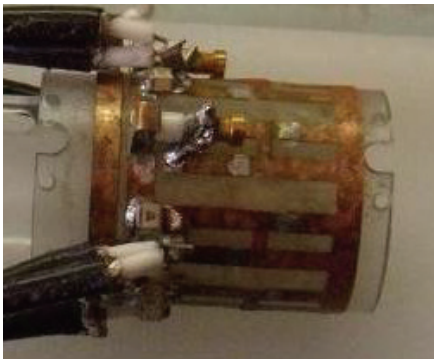

Figure II-40: *CP litz cage coil purchased from Doty Scientific.*

As its name indicated, the coil structure is a Litz cage that is a deviation from the low-pass birdcage structure. In the classic birdcage coil, each rung is one plain conductor. At high frequency, the current tends to flow in a confined layer close to its outer surface of the conductor therefore decreasing the effective cross-section of the conductor and increasing its effective resistance. This is known as the skin effect:

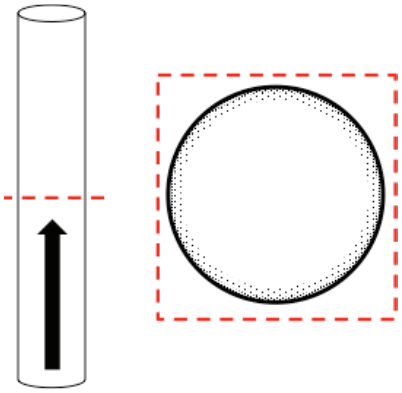

Figure II-41: *At high frequency, the current density is concentrated in a confined layer close to the surface of the conductor*

The thickness of this confined layer is usually known as depth of penetration and id dependent to the frequency:

$$\boldsymbol{\delta = \sqrt{\frac{\rho}{\pi \mu f}}} \qquad \textbf{(II-18)}$$

Where: ρ is the conductivity of the conductor in Ω.m

f is frequency in Hertz

μ is the absolute magnetic permittivity $\mu = \mu_0 \times \mu_r$ in which $\mu_0 = 4\pi \times 10^{-7} \mathrm{H.m}$

For copper, this thickness is:

$$\delta = \frac{7.6}{\sqrt{f}} \qquad \text{(II-19)}$$

The higher the frequency is, the more losses will be created by the skin effect. To transmit the higher frequency signal more efficiently, the plain conductor is replaced by multiple small wires twisted or braided into a uniform pattern, so that each strand tends to take all possible positions in the cross-section of the entire conductor. There will still be a skin effect in each small wire, but for the whole conductor, the losses are reduced because the current can be considered as flowing uniformly through its cross-section. The greater the number of small wires the conductor is made of, the less current loss caused by the skin effect. This kind of conductor has been named Litz wire where the word "Litz" is derived from the German word "Litzendraht" meaning woven wire.

In the case of a flat conductor (copper tape), instead of spreading equally on all surface of the conductor, the current flow on the two lateral edges as described in the following figure [13-16]:

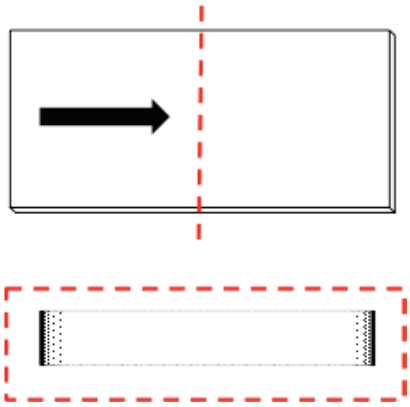

Figure II-42: *The current flows at the two edges of the flat conductor instead of spreading equally on all surfaces as in circular conductor. Noted that the thickness of the conductor is exaggerated in this figure for illustration purpose. In practice, the width of the tape is much larger compare to its thickness (20 to 30 times or even more).*

Copper tape and printed circuit board are widely used because of their ease in tailoring and placement (with help of etching machine or craft tools). If these materials were used, each rung will act as a flat conductor as described above (composed of 2 high density edgy currents). Because of this skin effect, increase the width of each rung doesn't help

spread the current density leading to no improvement in homogeneity and sample losses (reduce the voltage difference between the sample and the hotspot (created by currents flowed in each rung). To improve the distribution of current on the surface of the birdcage coil, one solution is to increase the number of rung. This solution leads to an increase of number of capacitors, therefore harder to build and to adjust the homogeneity of the coil. The Litz is introduced as a solution to improve the distribution of current while maintaining the same number of rung. This improvement can be explained as follow:

Applying this principle to a low-pass birdcage coil, Doty created a Litz cage structure where each rung of the coil is made of two parallel conductors or copper strips crossing each other at the middle of the coil [7, 9].

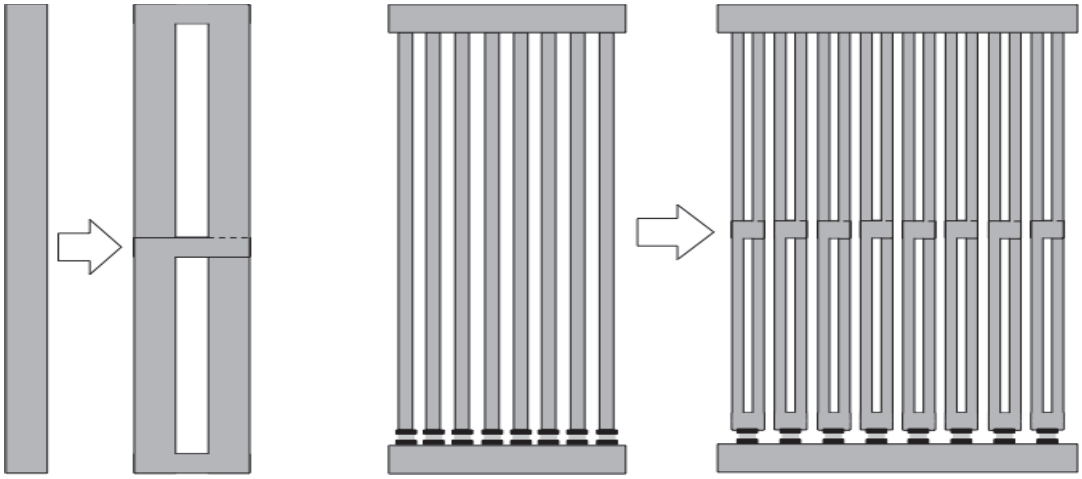

Figure II-43: *From conventional low-pass birdcage to Litz cage*

In the middle of each Litz rung, where 2 parallel conductors overlap each other, the current in these two conductors flows in opposite direction. The interaction between these currents leading to a change in behavior of the skin effect in flat conductor [15, 16]:

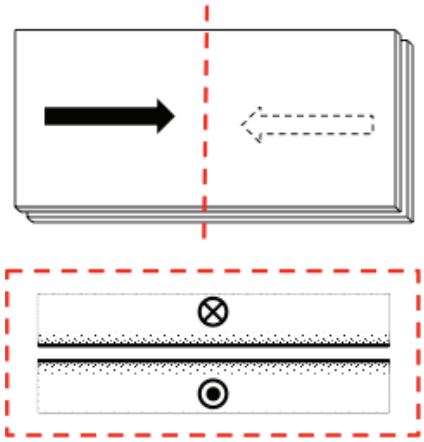

Figure II-44: *The overlapping area in the middle of each Litz rung where the currents flow in opposite direction forcing the current density to concentrate on the 2 inner surface of the conductor.*

This change in current density at the overlapping area of the Litz rung force the current divided in 4 edges instead of distributing on only two outer edges of the conductor:

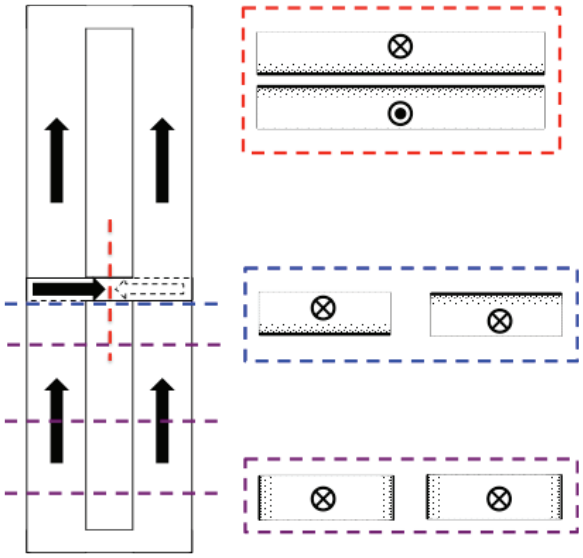

Figure II-45: *Figure illustrating the current density distribution of a Litz rung*

Compare to a classic birdcage with the same number of rung, the Litzcage structure has better current density distribution:

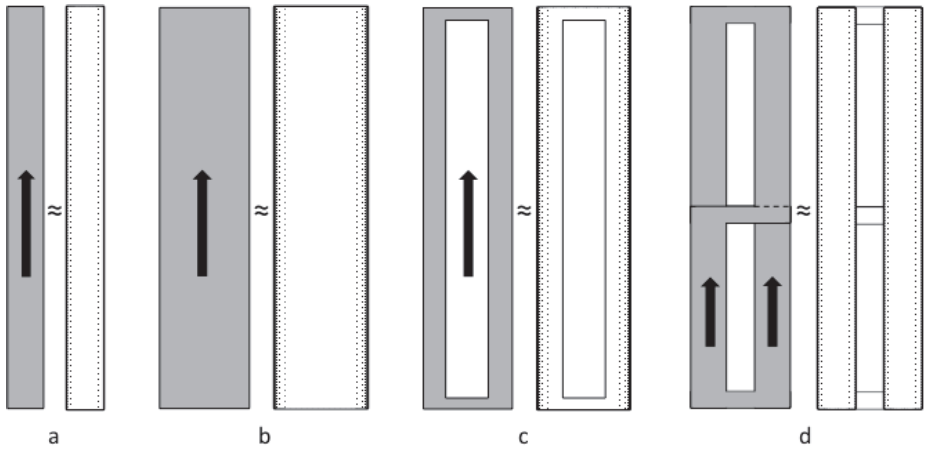

Figure II-46: *figures a) and b) illustrate the current distribution in a plain conductor flat rung of a classic birdcage. Figure c) illustrates the same current distribution same as the plain conductor even though the rung is hollow. Figure d) illustrates the current distribution improvement by using Litz effect.*

The current density distribution improvement on the surface of the coil helps to improve the homogeneity of the coil (a similar principle to increasing the number of rungs to improve the charge distribution) by remaining lower number of rung that will make the coil homogeneity adjustment easier (less of capacitors to redistribute – advantage of low-pass birdcage as mentioned previously). The expected improvement in homogeneity is about 10-30% and SNR improvement is about 15% compare to conventional CP birdcages of similar dimensions (http://www.dotynmr.com/).

Using a 30ml syringe filled with 5mM Gd- and the same protocol to characterize the CP gain as well as to color map the homogeneity of the coil, we determined that the CP gain of this coil is only 23% which is very low compared to the theoretical CP gain of 41%. This could be explained by the very low unloaded decoupling factor between the two channels of the coil – which was only -15dB and must be lower while the coil is loaded. The signal color map images of the coil were also obtained:

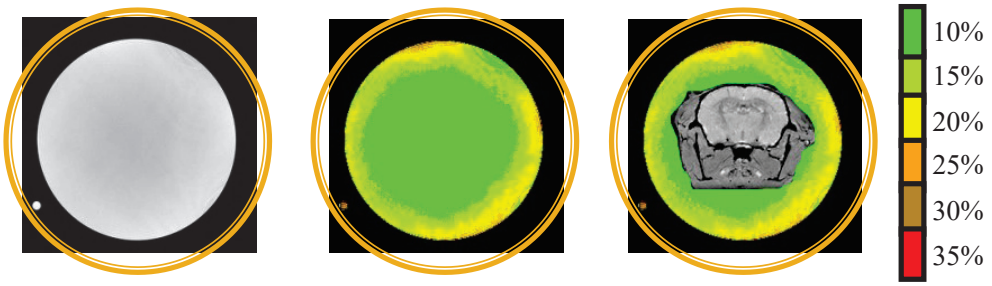

Figure II-47: *Color map of phantom image acquired with Doty Litz cage*

From this figure, we can conclude that this coil has excellent homogeneity to cover the cross-section of a mouse head. But the gap between the inner edge of the coil and the mouse head indicates that the filling factor of the coil is not optimized.

IV.3. Litz cage developed in-house

As discussed previously, the commercial coil didn't have an optimized filling factor for a mouse head, more specifically mouse olfactory bulb as required by one of our studies. Our aim was to develop a coil of customized dimensions to have a better filling factor, but we also need to assure that the homogeneity of the coil can cover the cross-section of a mouse head. As the Litz cage structure showed some improvement in homogeneity and SNR compare to the conventional birdcage (see chapter 3), we will use this design to develop our coil.

The inner diameter of the coil must be smaller than the Doty Litz cage to have a better filling factor, and must be bigger than the saddle coil previously mentioned to avoid the problem of hot spots. We used a 30ml plastic syringe as a coil support; this has an outer diameter of 23.5mm. The coil was made to have the same length of 29mm as the Doty Litz cage. Due to the thickness of the plastic support, the accessible diameter is limited to 21.5mm. Having determined the dimensions of the coil, we followed the coil designing steps (described previously) to make a coil that could be used in many in vivo projects.

Figure II-48: *Homemade Litz cage*

By varying the value of the variable capacitors installed on the coil, we can adjust the unloaded decoupling factor between the two channels of the coil to -19dB.The loaded decoupling factor was measured using an extracted mouse brain and was around -17dB.

This coil has a better decoupling factor than the Doty Litz cage and this improvement is reflected by the improved CP gain of 31%.

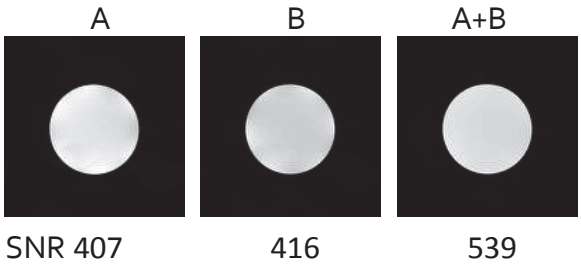

Figure II-49: *Gain in CP mode is about 31%*

As this coil is smaller than the Doty Litz cage, the distance between the coil and the sample is smaller, so we can predict that dielectric losses caused by the sample must be greater. The prediction was confirmed by measuring the unloaded and loaded Q factor of the 2 coils using the same sample (extracted brain). For the Doty coil, we have:

- Unloaded Q: 145
- Loaded Q: 143

And the dielectric losses:

$$\boldsymbol{Sample\ loss = 1 - {Q_L}/{Q_U} \approx 0.02\ (\sim 2\%)} \qquad \textbf{(II-20)}$$

For the in-house developed Litz cage:

- Unloaded Q: 165
- Loaded Q: 152

And the dielectric losses:

$$\boldsymbol{Sample\ loss = 1 - {Q_L}/{Q_U} \approx 0.08\ (\sim 8\%)} \qquad \textbf{(II-21)}$$

Even though the dielectric losses are greater than with the Doty coil, the SNR can be compensated by a greater filling factor - with the same sample, the filling factor of the in-house developed coil is 41% greater than the Doty coil. Combined with a greater loaded quality factor (6% higher) we expected a gain of 22% in SNR. The experimental result only showed a gain of 11%. This can due to the closer proximity of the sample to the hot

spots of the coil and the sample shape (not cylindrical shape) leading to a shifting of balance between the 2 channels of the circular polarized structure.

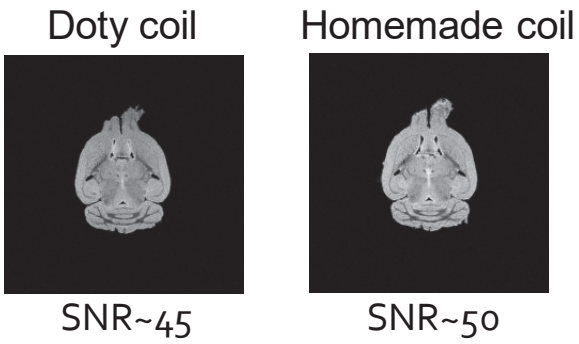

Figure II-50: *SNR comparison between the Doty coil and the homemade coil. The SNR of each coil was measure from the mean of signal obtained from ROI inside the mouse brain and the background noise (standard diviation)*

The next step is to test the homogeneity of the coil to insure a good coverage of the mouse head. Using the same protocol used with the saddle coil and the Doty coil, we obtained the results:

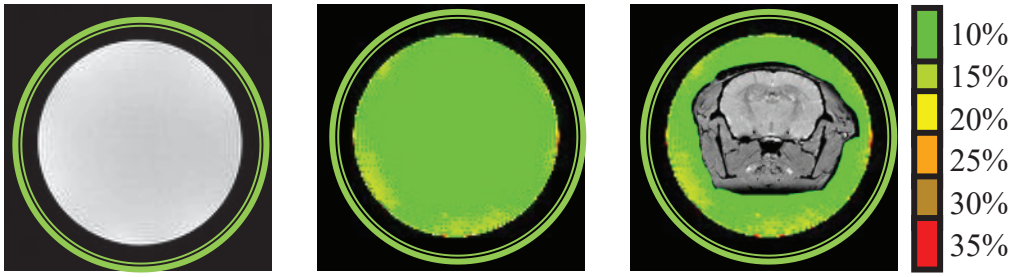

Figure II-51: *Homogeneity map of the homemade birdcage litz coil*

From this figure, we can observe that the homogeneity of the coil can cover very well the cross section of the mouse head.

In conclusion, compared to the commercial coil, the homemade coil of smaller dimensions is a tradeoff between the filling factor and the sample losses. In the end, the overall gain in filling factor help to overcome the losses that leads to a gain of 11% in SNR (equivalent to 20% less in scanning time).

After the coil was developed, we had to consider another aspect of in vivo MRI - mouse body temperature during the scan. Maintaining a stable body temperature keeps the

mouse healthy during the scan and helps the mouse to recover faster after prolonged anesthesia. To control mouse body temperature, we use 2 water-heating systems in which the mouse is heated underneath and also on top of its body.

- A warming pad is fixed on the coil setup to control mouse body temperature from underneath:

Figure II-52: *Warming pad placed on the coil holder next to the coil to control mouse body temperature from underneath.*

- Using a water pump with which we can control the temperature of the circulated water:

Figure II-53: *Water pump with built-in heating system*

- To control the temperature of the mouse body, we use a homemade warming pad which is consists of snaked plastic tubing which is glued to a curved polycarbonate support:

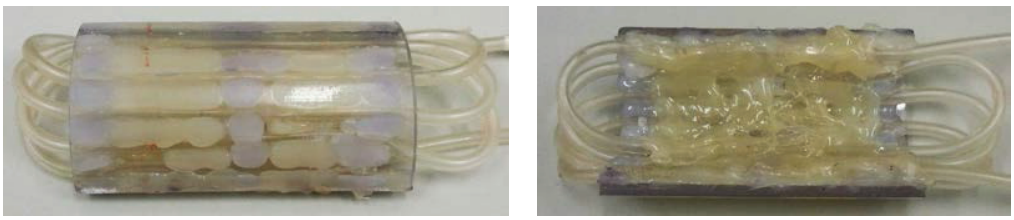

Figure II-54: *Two sides of the homemade warming pad to place on top of the mouse body*

- The water circulated through this warming pad is controlled by this pump:

Figure II-55: *Second water pump with built-in heating system to control mouse body temperature from top.*

This warming system allows us to maintain the mouse body temperature at 37°C during the whole scan. This combination of coil and warming system has been used in multiple projects to study the mouse brain anatomy, neurodegenerative diseases, and the effect of contrast agents. Our findings have been published and presented at recent international conferences:

Bertrand A, Khan U, Hoang DM, Novikov DS, Krishnamurthy P, Rajamohamed Sait HB, Little BW, Sigurdsson EM, Zaim Wadghiri Y. "**Non-invasive, in vivo monitoring of neuronal transport impairment in a mouse model of tauopathy using MEMRI**". *Neuroimage*. 2012 Aug 31, PMID: 22960250(2012).

Yang J, Zaim Wadghiri Y, Hoang DM, Tsui W, Sun Y, Chung E, Li Y, Wang A, de Leon M, Wisniewski T "**Detection of Amyloid Plaques Targeted by USPIO-Aβ1-42 in Alzheimer's Disease Transgenic Mice using Magnetic Resonance Microimaging**". *Neuroimage,* 55(4):1600-9. PMID: 21255656. (2011).

Bertrand A, Hoang DM, Khan U, Zaim Wadghiri Y "**From axonal transport to mitochondrial trafficking: What can we learn from Manganese-Enhanced MRI studies in mouse models of Alzheimer's disease?**", Current medical imaging reviews 7(1):16-27. (2011).

V. Conclusion

In this chapter, we summarized a brief theoretical study of the birdcage structure and also our practical procedure to build, characterize coils that were adapted to needs. The birdcage design proved again its capacity to provide a large homogenous RF field coverage – demonstrated by the color-maps that were generated using the in-house

developed ImageJ macro. This coil structure was used to make various coils in this study such as whole mouse body coil or low-pass birdcage for 4-brain scan (chapter 3). Our study described different methods to improve the homogeneity, sensitivity of the birdcage structure through the distribution of signal feeding, circular polarization or Litz structure (see more in chapter 3). All these improvements were applied to our homemade mouse head coil in combination with taking advantage of the filling factor by making the coil dimension fit closely the mouse's head. Our homemade head coil showed 10% improvement in SNR compare to the larger commercially available Litz coil while maintaining similar homogeneity. This coil has been used in most of our in vivo projects that are related to the mouse brain studies and led to multiples important findings that were published in international journals.

References

[1] E. C. Hayes, A. W. Edelstein, F. J. Schenck, M. O. Mueller, and M. Eash, "An Efficient, Highly Homogeneous Radiofrequency Coil for Whole-Body NMR Imaging at 1.5T," *Journal of Magnetic resonance,* vol. 63, pp. 622-8, 1985.

[2] C. N. Chen, D. I. Hoult, and N. J. Sank, "Quadrature Detection Coils. A further 2 Improvement in Sensitivity," *J. Mgn. Reson.,* vol. 54, pp. 324-327, 1983.

[3] M. Alecci, C. M. Collins, M. B. Smith, and P. Jezzard, "Radio frequency magnetic field mapping of a 3 Tesla birdcage coil: experimental and theoretical dependence on sample properties," *Magn Reson Med,* vol. 46, pp. 379-85, Aug 2001.

[4] C. M. Collins and M. B. Smith, "Calculated B1 homogeneity, SNR, and SAR vs frequency for the head in a idealized quadrature birdcage coil," *Proc ISMRM,* pp. 7-417, 1999.

[5] J.-M. Jin, *Electromagnetic analysis and design in magnetic resonance imaging*. Boca Raton: CRC Press, 1998.

[6] J. l. Mispelter, M. Lupu, and A. Briguet, *NMR probeheads for biophysical and biomedical experiments : theoretical principles & practical guidelines*. London; Hackensack, NJ: Imperial College Press; Distributed by World Scientific, 2006.

[7] F. D. Doty, G. Entzminger, J. Kulkarni, K. Pamarthy, and J. P. Staab, "Radio frequency coil technology for small-animal MRI," *NMR Biomed,* vol. 20, pp. 304-25, May 2007.

[8] P. Pimmel, "Les Antennes en resonance magnetique nucleaire : fonctionnement et realisation. Resonateurs pour l'imagerie et pour la spectroscopie in vivo," Doctorat, genie biologique et medical, Lyon 1 - Claude Bernard, Lyon, 1990.

[9] F. D. Doty, G. Entzminger, Z. Rafique, L. Holte, and T. Welsh, "The Litzcage – a High-field Circular-polarization RF Coil with Improved Tunability, B1 Homogeneity, and S/N," presented at the ENC, Asilomar, 2002.

[10] S. Serfaty, L. Darrasse, and S. Kan, "Double-bracelet resonator Helmholtz probe for NMR experiments," *Review of Scientific Instruments,* vol. 66, pp. 5522-5526, Dec 1995.

[11] D. M. Ginsberg and J. M. Melchner, "Optimum Geometry of Saddle Shaped Coils for Generating a Uniform Magnetic Field," *Review of Scientific Instruments,* vol. 41, pp. 122-3, 1969.

[12] O. L. Hoppie, "Form for supporting saddle-shaped electrical coils," 1966.

[13] F. Mesa and R. J. David, "The Danger of High-Frequency Spurious Effects on Wide Microstrip Line," *IEEE TRANSACTIONS ON MICROWAVE THEORY AND TECHNIQUES,* vol. 50, pp. 2679-89, 2002.

[14] H. T. Petersen, "A TRANSIENT SOLVER FOR CURRENT DENSITY IN THIN CONDUCTORS FOR MAGNETQUASIOSTATIC CONDITIONS," DOCTOR OF PHILOSOPHY, Department of Electical and Computer Engineering College of Engineering, KANSAS STATE UNIVERSITY, Manhattan, Kansas, 2009.

[15] A. Ducluzaux. (1983). *Extra losses caused in high current conductors by skin and proximity effects (1 ed.)*. *83*.

[16] R. Kollman. (2010). *Current distribution in high-frequency conductors*.

Chapter III: High throughput ex vivo MRI for mouse brains

Introduction

In pre-clinical MRI research, *ex vivo* MRI is a very important tool to co-register MRI with histology data. Ex vivo MRI data is more reliable than *in vivo* MRI because it has the following advantages [1, 2]:

- No motion artifacts
- No limitations in scan time (no need to worry about keeping the subject alive) that leads to higher SNR and also higher spatial resolution.

ex vivo MRI is also a crucial step for the pulse sequence development, optimization of imaging parameters to maximize signal and/or image contrast as well as for the test of newly designed protocols.

With the advances of parallel imaging, using multiple coils to scan multiple subjects at a time helps to increase tremendously the efficiency of the MRI scanner [3-6]. While parallel imaging is nowadays familiar in clinical system, it's still a novelty and consider expensive for pre-clinical research. Many MRI systems using in small animal imaging is not equipped of this technique.

With only one receiving channel system, the idea of fitting multiple samples in the same coil to reduce scanning time (reducing cost) has been introduced since more than a decade [7-9]. Despise its disadvantage in performance (up to 3 times less in SNR) compared to parallel imaging (where each sample can be fitted in one separated coil [10]), this technique still help to increase the efficiency of the MRI system.

In our case, where parallel imaging is not available and the longest *ex vivo* scanning time is limited to an overnight scan time of 8 to 10 hours, we aim to increase the throughput of the ex vivo scan, especially for extracted mouse brains. Our requirements for ex vivo MRI are the following:

- SNR over 30 (reasonable for quantitative study) for a scan time less than 8 hours (average unattended overnight scanning time)
- Homogeneity of the coil must cover the region of interest

From these requirements, we have developed several coils to increase the throughput of the ex vivo mouse brain MRI to make an overnight scan time more efficient. To characterize the efficiency of an ex vivo scan, we use the following definition [11]:

$$\boldsymbol{\eta = SNR \times \sqrt{\frac{N_{Av}}{T_{Im}}}} \qquad \textbf{(III-1)}$$

where η is the efficiency of the scan, N_{Av} is the number of averaging, T_{Im} is the scanning time. In our case, the sample contains multiple brains; thus the definition must be modified depending on the number of brains:

$$\boldsymbol{\eta = SNR \times \sqrt{\frac{N_{Av}}{T_{Im}}} \times n_{brain}} \qquad \textbf{(III-2)}$$

Using this definition, we can compare the efficiency of different coils and different numbers of brains.

I. Sample preparation protocol for mouse extracted brains

I.1. Mouse brain extraction

In our general protocol, after the in vivo scan, the mice were sacrificed by means of an intravenous (IV) injection of sodium pentobarbital (Nembutal, 200 mg/kg) and were transcardially perfused with phosphate buffered saline (PBS) solution followed by buffered 4% Paraformaldehyde in cold PBS to fix the tissue. The brain was then extracted from the skull and fixed in 4% Paraformaldehyde for at least 24 hours before the ex vivo scan [12].

I.2. Mouse brain preparation for MRI

Mouse brains post fixation could be mounted on a plastic support (made from the plunger of a syringe):

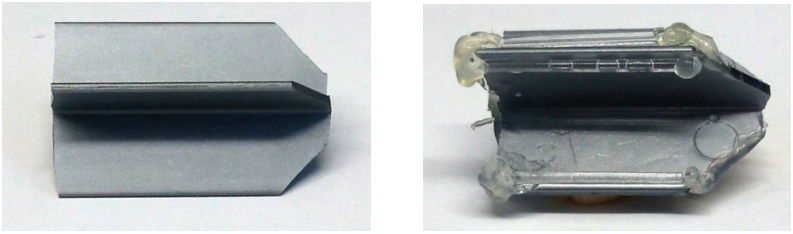

Figure III-1: *Plastic support made from syringe plunger to mount the fixed brains.*

Glass tubes filled with water were glued to the sides of the plastic support to help determine the orientation of the brain and also to differentiate between brains after the scan.

The brain was fixed on the plastic support using super glue. Because the super glue could strongly affect the magnetic field homogeneity, we have to use a very small amount on the brain and place it far away from the region of interest (normally at one end of the brain where the spinal cord is left from the extraction):

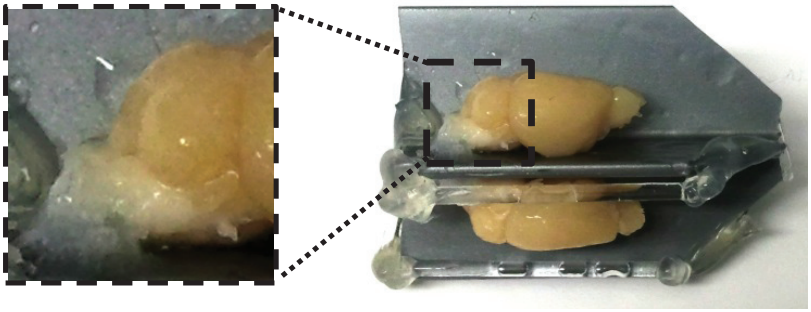

Figure III-2: *Fixed brains mounted on the plastic support using super glue. The super glue was applied far away from the region of interest to avoid artifacts.*

Once the super glue is dry (It will take about 30 minutes), we put the plastic support with mounted brain in a Luer locked syringe (the size of the syringe varies with the number of brains). The syringe will be filled with Fomblin (Perfluoro Polyether) and its plunger will be pushed in to stop the solution from leaking:

Figure III-3: *The brain setup was placed inside a syringe with a stopcock lock.*

To avoid air bubbles (another source of artifacts and signal void), we placed the whole setup with the Luer lock in the open position in a vacuum chamber for degassing:

Figure III-4: *Vacuum chamber for degassing.*

The vacuum chamber was then connected to a vacuum pump for degassing. The degassing time will depend on the size of the syringe, but normally 45 minutes is sufficient. Degassing is complete when no air bubbles can be seen in the syringe:

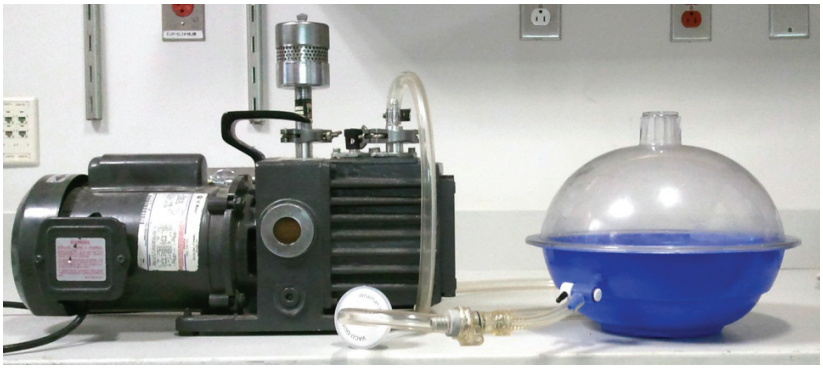

Figure III-5: *Setup of our degassing system.*

After degassing, we push the plunger further into the syringe to stop the plastic support with mounted brains from moving inside the syringe and also to extract the extra Fomblin from the syringe.

II. Existing coil for 1 or 2 brain throughput

One of our ex-vivo projects is to target Amyloid plaques using USPIO-Aβ-42 (Ultra-small Super-Paramagnetic Iron Oxide) in Alzheimer's disease transgenic mice [13]. To verify the effect of the contrast agent, and to define the injection dose, necessary circulating time in the mouse body, we first verify with ex-vivo scans the presence of iron oxide particles in the mouse brain. The Amyloid plaques are located mostly in the cortex area of the brain [14]. Our requirement for this study is that the homogeneity of the coil must cover the cross section of the cortex of the mouse brain. All our coils were first verified or designed to match this condition.

II.1. Coil for 1 brain scan

The homemade head coil was designed to tightly fit the mouse head; this allows us to take advantage of the filling factor and its homogeneity to cover the cross section of the mouse brain. Therefore this coil can be used to scan one ex vivo brain:

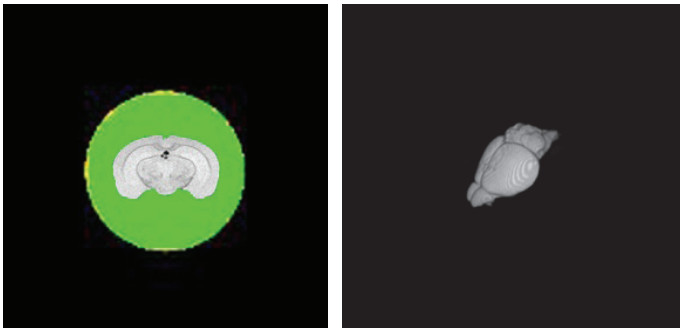

Figure III-6: *Head coil's homogeneity for 1 brain setup.*

To secure the brain, we can use a 10ml or 12ml syringe (both of these sizes have enough space to accommodate one brain). To be able to compare the efficiency between the coils, all the samples were prepared in the same way and scanned with the same sequence at the same resolution and bandwidth. Below are the parameters:

- Sequence: 3D MGE – 4 echoes – 100µm isotropic
    - FOV: 2.56 x 2.56 x 2.56 cm (5.12 x 2.56 x 2.56 cm for 8 brain scans)
    - Matrix: 256 x 256 x 256 (512 x 256 x 256 for 8 brain scan)
    - TE/TR: 4.07/50ms
    - Echo spacing: 6.7ms
    - FA: 20^{o}
    - Bandwidth: 195Hz/pixel
    - Number of Average (NA) and Scan time varies following the coil size. In the case of 1 brain scan, NA is 2 and the scan time is 110 minutes.

The 3rd echo gives us a reasonable SNR and also good contrast to differentiate amyloid plaques from the tissue; therefore, images from this echo will be used in our measurement of SNR. After the scan, the overall SNR of the scan was measured by obtaining an average value from the measurement of multiple slices. This measurement gives an average SNR of 46.

Using the formula III-2, we calculated the efficiency of this coil and obtained an efficiency of 6.2.

II.2. Coil for 2-brain scan

In order to validate the consistency of our results, we need to repeat our experiments multiple times, hence the need to scan multiple brains. In order to make the ex vivo scan time more efficient, we would like to increase the throughput of our scans. Instead of one brain, we aim to scan two brains at a time. The previous coil was too tight to fit 2 brains. To be able to do this experiment, we need a bigger coil that could fit a 30ml syringe (have enough space for 2 brains). Our solution was to use the commercially available Doty Litzcage coil mentioned in previous chapter. The brains will be fixed on 2 sides of a plastic support made from a syringe plunger as in the previous case. A glass tube is used to mark one of the brains; this helps to distinguish the brains after the scan.

Prior to the scan we need to verify the homogeneity of coil to cover the cross section of 2-brain samples. Using the color mapped images and an MRI of 2-brain samples; we can confirm that this coil matches our requirements:

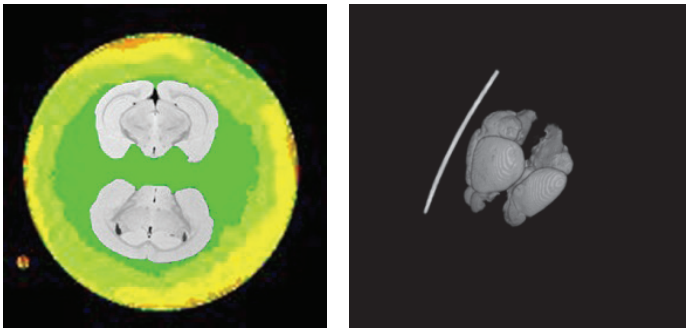

Figure III-7: *Doty Litzcage head coil for 2-brain scans.*

With this setup of coil and sample, we can use the same sequence used to scan 1 brain, because the FOV can cover 2-brain samples. Since the filling factor of this coil is lower than the homemade head coil, we can predict that the SNR will be lower than for 1-brain scan. The measurement confirmed the prediction with a SNR of: 42, which is about 10% lower compared to a SNR of 46 for the homemade head coil. Although the SNR of this scan is lower than the previous scan of one brain, the image quality still exceeds the limit of a SNR of 30 and also we can scan 2 brains at a time, thus improving our efficiency. This was proven by the calculation using formula III.2 that gave an efficiency of 11.3 (almost double the efficiency 6.2 of the head coil).

III. Design coil for 4 brain throughput

III.1. Requirements

As mentioned previously, the sample preparation requires a fair amount of time (about 1.5 hours for 2-brain samples). The preparation of 4-brain samples does not take significantly more time since 2 brains can be glued simultaneously on the same side of the plunger. If we were able to scan 4 brains at a time, the overall preparation time will be reduced by a factor of 2.

The previous experiments showed that by increasing the throughput, we increase also the efficiency of our ex vivo scanning time. In this direction, we aim to increase the scan throughput to 4 brains. We also want to insure image quality; therefore, our new coils must fit tightly inside the syringe that can accommodate 4 brains without squeezing any of them. A 35ml syringe is perfectly suited for our requirements. More conveniently, we can use the syringe holder as a coil support that fits tightly the syringe and take good advantage of the filling factor. Our first choice is a CP low-pass birdcage structure because it's easy to make and also has a wide range of tuning and matching frequency, is easy to adjust the homogeneity and the decoupling factor between the 2 channels in CP mode. Using the principles of coil design we described in previous chapter, we made a CP low-pass birdcage with the following dimensions:

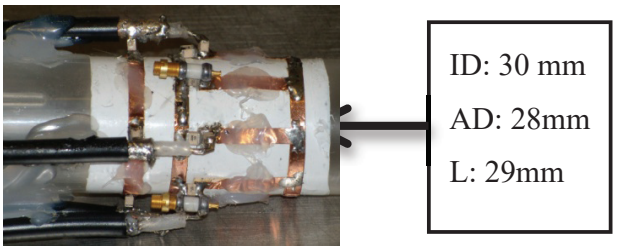

Figure III-8: *Low-pass birdcage for 4-brain scans.*

Using the procedure for coil characterization, we obtained:

- QU/QL: 124/104 (Loaded with a water phantom)
- CP decoupling factor: 21dB
- CP gain: 24%

We also need to make sure that the homogeneity of the coil satisfies our needs:

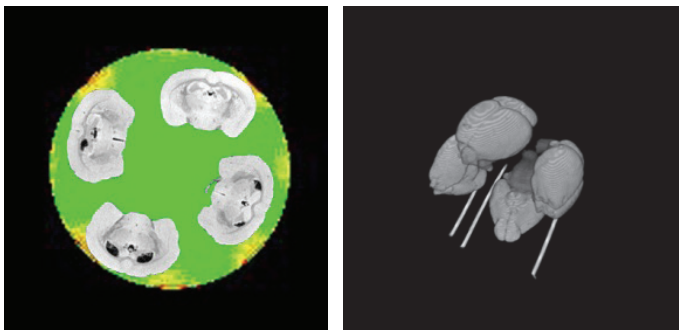

Figure III-9: *The first positioning of the brain isn't optimized for the coil homogeneity.*

From these images, we observed that the homogeneity of the coil might not be sufficient for 4 brains. But with this particular positioning of the brains, the space in the middle of the coil was unused. Therefore, we came up with another positioning of the brain to take advantage of the wasted space in the previous setup:

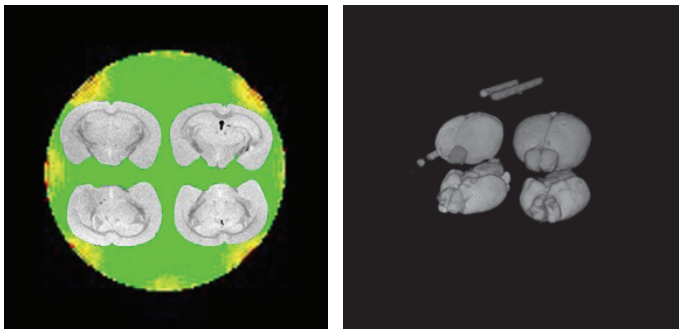

Figure III-10: *The second positioning of the brains takes advantage of the homogeneity in the coil's center and also keeps the brain further away from the hot spots.*

With this setup, the brain is positioned further away from the hot spots of the coil and occupies more of the homogeneous area. With this coil, we reach a SNR of 39.4 with 147 minutes scan time that leads to an efficiency of 22.5.

As mentioned before, Doty Scientific claims that the CP Litzcage has better homogeneity and also SNR compared to a conventional CP birdcage with similar size [15]. To be able to compare the two structures, we designed a CP Litzcage with the same dimensions of the low-pass birdcage:

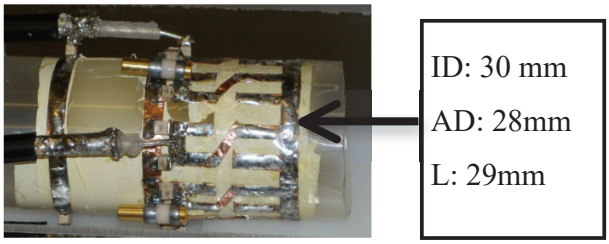

Figure III-11: *Homemade Litzcage for 4-brain scans with the same dimension as the low-pass birdcage.*

This coil has the following characteristics:

- Q_U/Q_L: 122/109 (Loaded with a water phantom)
- CP decoupling factor: 19dB
- CP gain: 40%

In our experiments this structure didn't give us a better QU factor but gave us better QL, which meant it has less sample loading effect compared to the low pass structure. This can be explained by the Litz effect (detailed in chapter 2) that reduced the capacitive loss. A signal intensity color map was also generated for this coil to validate its homogeneity:

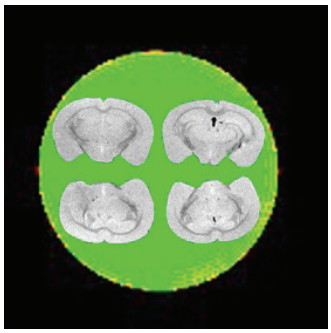

Figure III-12: *The Litz structure helped to improve the homogeneity of the coil compared to the low-pass birdcage.*

We can see here that this coil is much more homogenous compared to the low-pass birdcage; there's less effect of the hot spots on the images. This improvement was given by the Litz effect that helps to distribute the current on the surface of the coil. With the same 4-brain sample and same sequence as the low-pass birdcage, we obtained a SNR of 48.7 that corresponded to an efficiency of 27.8 for a scanning time of 147 minutes.

With this coil, we were not only improving the coil homogeneity but also coil sensitivity that led to a higher efficiency of our scanning time. The ability to scan at a higher throughput also reduced the sample preparation time (almost the same preparation time compared to 2 brain samples).

In conclusion, the Litz structure does help improve the homogeneity and sensitivity compared to a traditional low-pass birdcage while retaining the same advantages (low number of capacitors, easy CP decoupling).

IV. Homogeneity improvement for 4-brain scans

IV.1. Needs of RF homogeneity improvement

In the context of the study using USPIO to target Alzheimer plaques, we would like to apply a more quantitative method to show the effect of the contrast agent. To do this, we used a MATLAB toolbox developed specially for mouse brain studies called SPM mouse [13, 16-18]. The principal of this toolbox is to compare statistically the difference in signal intensity given by 2 groups of mouse brains. All the images acquired from the brains of the 2 groups of mice will be reshaped following a model generated by default (mask). Afterward, the brains from the 2 groups will be compared to each other and the statistical difference will be given by color-coding. This comparison is done by comparing pixel by pixel of the reshaped images; therefore, every pixel of the images must be acquired under the same condition. This means that the RF homogeneity of the coil must cover the whole of the brain (not only the cross section of the cortex area as in the qualitative study). With this new requirement, we also need to verify the homogeneity of the coils along their length.

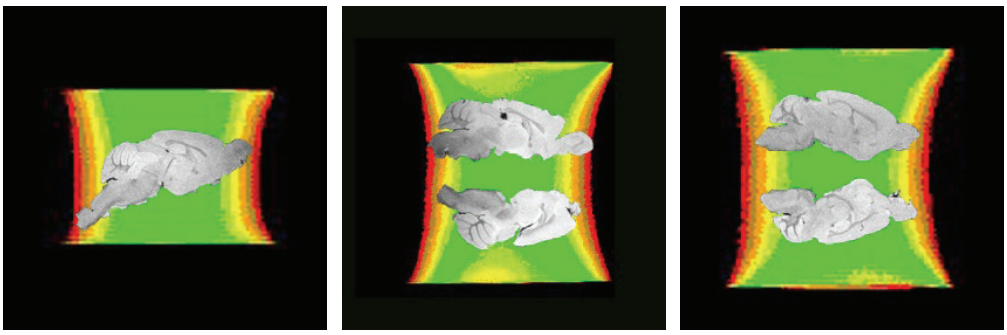

Figure III-13: *None of the coils used so far have provided sufficient homogeneity for the brain setups in the Z direction of the gradient (along the length of the coil)*

As we can see, all the coils used till this stage have not had sufficient homogeneity to cover the whole of the mouse brains. This problem might lead to errors in the statistical study in the areas that are not covered by the homogenous RF field.

IV.2. Solution

This problem forced us to find a coil with better homogeneity coverage in the Z direction of the gradient (along the length of the coil). For this, we have obtained a commercially available coil which has been used for mouse abdomen studies which has the dimension of:

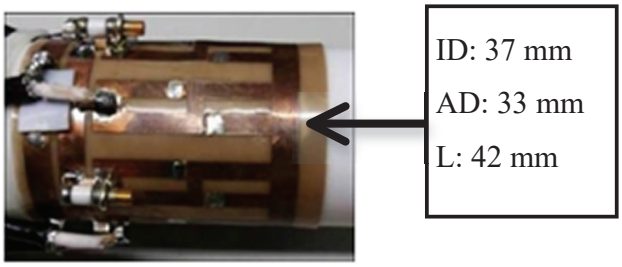

Figure III-14: *Doty abdomen coil for 4 brain scans*

This coil has excellent homogeneity coverage for 4 mouse brains in both directions:

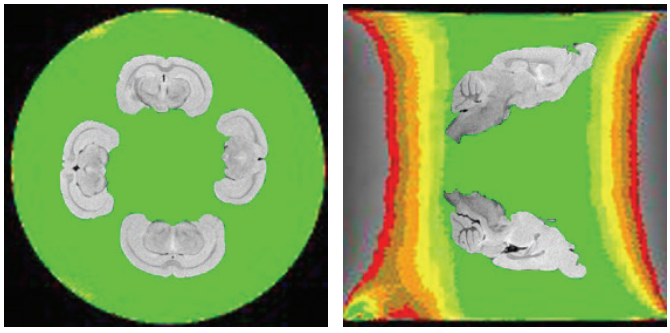

Figure III-15: *The coil provides excellent homogeneity coverage for 4 brain setups*

As observed, the homogeneity of this coil satisfied the requirements of the SPM mouse toolbox. The next step is to verify if it's sensitive enough for our 4-brain scan. We aim to have a SNR higher than 30 for the 3rd echo. As mentioned at the beginning of the chapter, our time limit is 8h (corresponding to an overnight scan time). The volume of this coil is 2.2X compared to the previous 4-brain coil that leads to a filling factor 2.2X lower. This means we need to scan twice as long to have the same level of SNR compare

to the previous coil. The measurement of SNR from the images acquired with this coil during 343 minutes (2.3 times longer than the scan used in previous experiments) is 44, which is close to the expected value of 48. The value of the measured SNR is lower than the expected value due to the larger dimension of the coil that led to having more copper strip on the coil (longer rungs and rings); therefore, the internal resistance r of the coil is higher. That reduces the QU factor of the coil and was proved by a measured value of: 115. Another factor that can affect the sensitivity of the coil is the CP gain which was only 35%, compared to 40% for the previous coil. Finally, this coil has an efficiency of 25.1 which is slightly lower than the previous homemade Litzcage coil (efficiency of 27.8)

The homogeneity and sensitivity of this coil satisfy our requirements for scanning 4 brains at a time and also the requirements of SPM Mouse toolbox. We used this coil to generate a large number of MRI images of mouse brains in different groups. These images were then analyzed statistically using SPM Mouse. The results were published with our collaborators in the following article [13] by Yang J. *et al.,* 2011.
Here are examples of two comparisons between two groups of mice that were described in the paper using this coil: Wild Type vs. APP/PS1 mice.

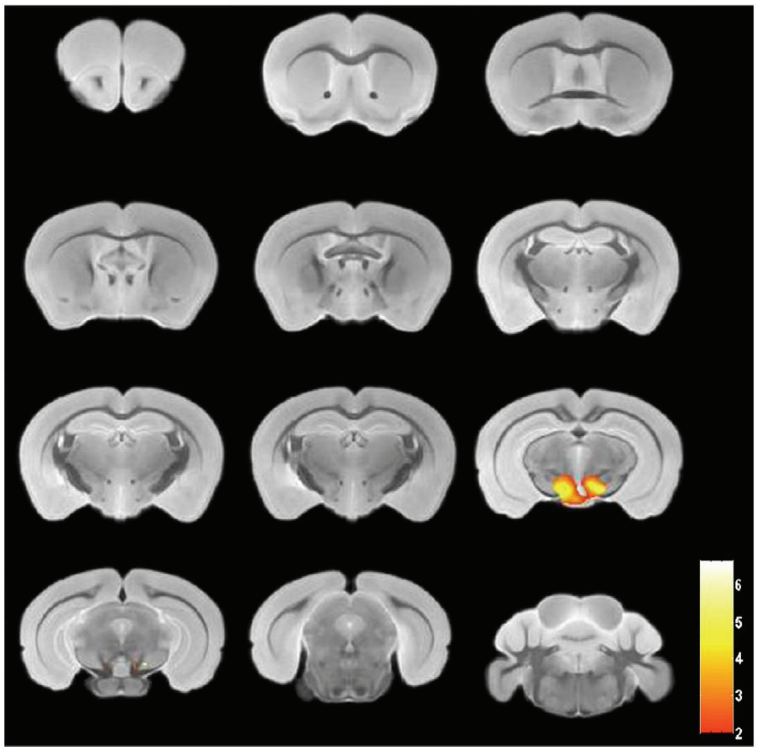

Figure III-16: *There was no difference in the cortex and hippocampus in wild-type (n=12) and APP/PS1 Tg (n=12) mice without contrast injection (p<0.01), by the voxel-based analysis of the ex vivo μMRI shown. The only region that was significantly different was in the midbrain, which is likely to be due to a slight atrophy of this area in the APP/PS1 Tg mice. Color bar units are the T-score.*

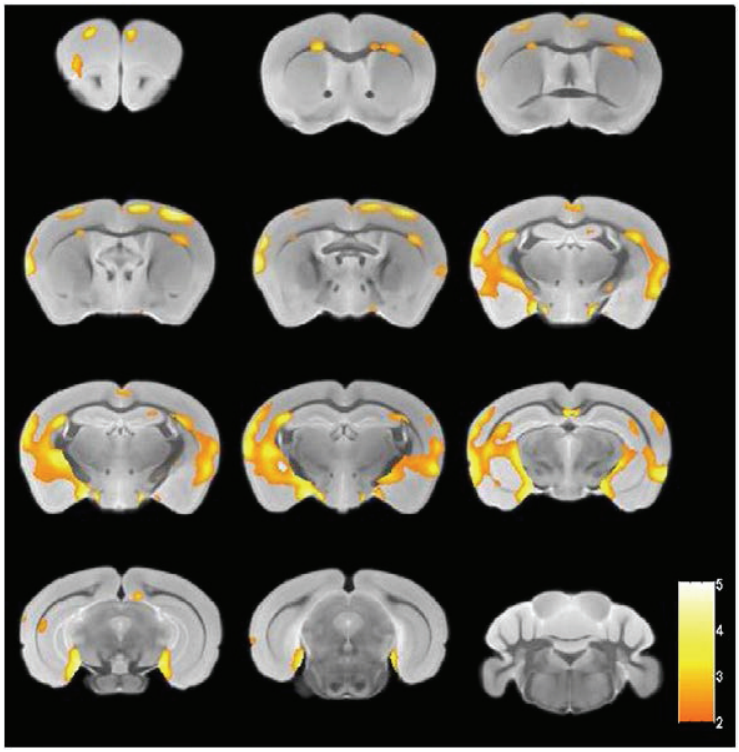

Figure III-17: *Areas of the brain are shown which differed by voxel-based analysis of ex vivo µMRI comparing USPIO-Aβ1–42 injected wild-type (n=12) and APP/PS1 Tg (n=13) mice (p<0.01). The regions of differences mirror the distribution of amyloid plaques histologically, being mainly in the cortex and hippocampus. Color bar units are the T-score.*

V. Development coil for 8-brain scans

V.1. Verification of resources

The previous coil gave us excellent results and also enabled us to scan at higher throughput (4 brains at a time). However, if we look at the signal intensity color map of the coil, we can see that the homogeneity of this coil can only cover one row of brains that corresponds to about 17 mm in the Z direction of the gradient coil. Our gradient coil has a linearity of 5cm; if we are to increase the throughput, the linearity of the gradient is sufficient to add one more row (counting the space needed between the two rows). Also, we haven't fully take advantage of the 8h overnight scan time (we only need approximately 6 hours to have a SNR higher than 40).

As we still have resources to increase throughput, we aim to develop a coil that can cover 8 brains (separated in 2 rows with 4 brains in each row):

Figure III-18: *8-brain setup for high throughput scans*

V.2. Development of a large Litzcage coil for 8-brain scans

Earlier in this chapter, we demonstrated the advantages of the Litzcage structure in terms of its improved homogeneity and sensitivity. Therefore, we will use this structure to develop a coil for 8-brain scans.

In order to cover 8 brains positioned in 2 rows, we need to increase the length of the coil. If we examine the homogeneity of a birdcage coil (or Litzcage), we see that it has the following pattern:

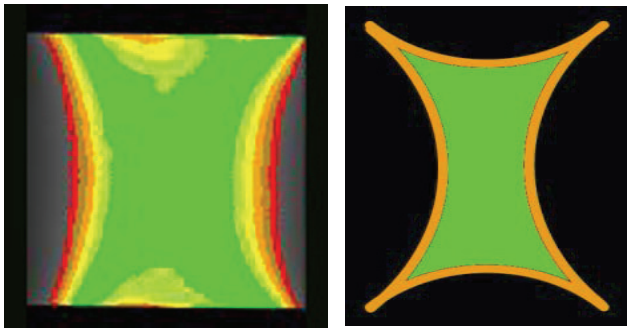

Figure III-19: *General pattern of homogeneity of a birdcage coil*

If we are to increase the length of the coil, we also need to increase its diameter in order to maintain the homogeneity in the X and Y direction (following the axes of the gradient coil). After multiple attempts, we finally come up with the following structure:

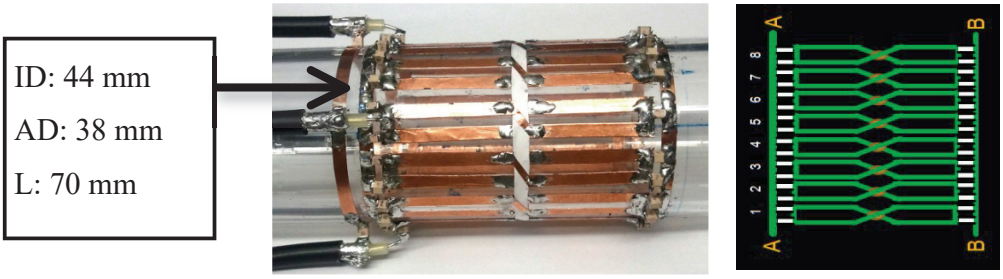

Figure III-20: *Large Litzcage coil for 8 brain scans.*

To insure coil homogeneity and reduce the effect of hot spots, we increased the number of rungs from 8 to 12. Another modification, as mentioned in chapter 2 (for low-pass birdcage), was to distribute the capacitors on 2 sides of each rung in order to be able to use higher value capacitors and also to balance the current distribution on the two end rings of the coil. The homogeneity of this coil can perfectly cover the 8-brain setup:

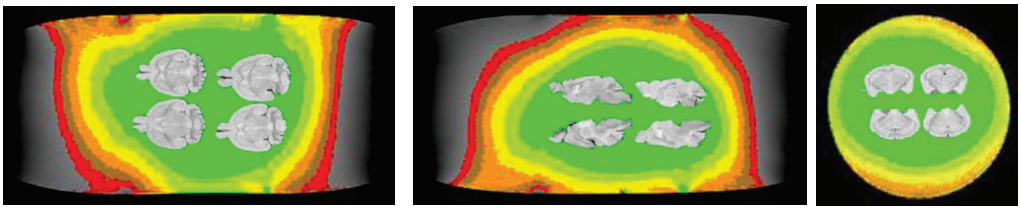

Figure III-21: *The large coil provides good homogeneity coverage for 8 brain setup*

The volume of this coil is 2.35 times larger compared to the Doty abdomen coil for 4-brain scan, which means its filling factor is very low and we expect a considerable loss in SNR. This was proven to be the case when we ran a scan of 8 brains with the same

sequence previously used and a scan time of 343 minutes. The measured SNR of the 3rd echo was only 17.6.

This SNR is insufficient for our requirements, even if we scanned for 12h, the SNR wouldn't reach the limit value of 30. Therefore we will have to design another structure with better sensitivity while maintaining the same homogeneity coverage.

The previous structure achieved excellent homogeneity for 8-brain scans but the low-filling factor led to a low sensitivity and the practical SNR is far lower than our requirements. The Doty abdomen coil has a diameter larger than needed (the homogeneity in the XY plan was sufficient) but its length is just enough to cover the length of mouse brain. Our new structure must have the length equivalent to 2 Doty abdomen coils put together while maintaining similar or smaller diameter.

After few essays, we end up with the final design:

- The coil is 23% longer than the Doty abdomen coil; therefore, the diameter must be smaller to maintain the similar filling factor. Using an existing plastic support with the diameter of 33mm, we obtained very similar filling factor to the Doty coil.
- The signal feeding is in the middle of the coil to break the pattern of the homogeneity of a classic birdcage coil (divide the curvature by two).

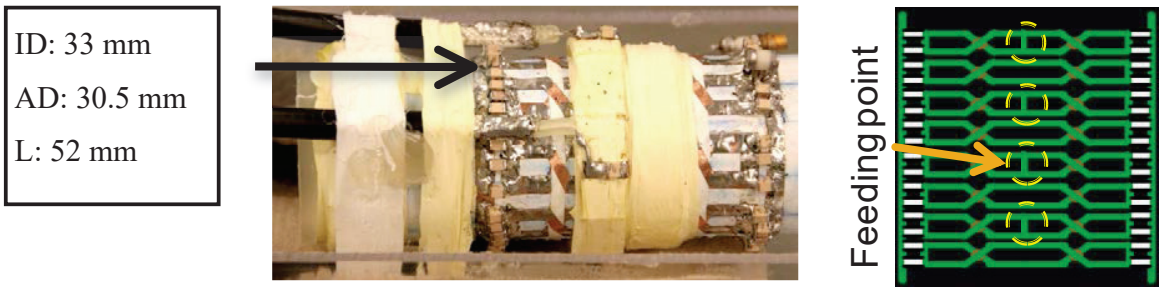

Figure III-22: *Designing a double Litzcage coil for 8 brain setup (to keep a symmetry between 2 sides of the coil).*

The first step is to verify homogenous coverage of the coil:

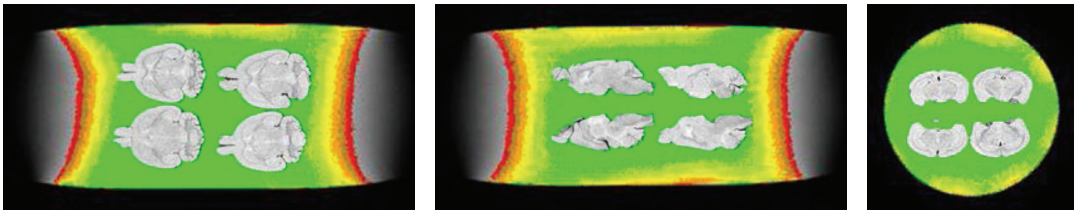

Figure III-23: *The newly designed coil also provided good homogenous coverage for 8 brains.*

As we observed, the homogeneity of this coil can also cover 8 brain setups in every direction that is matched with the requirement of SPM Mouse toolbox. The next test is to verify the sensitivity of the coil. For this, we used an 8-brain sample and scanned with the same sequence as previously used. The measurement of SNR on the third echo gave us a value of 40 that is 10% lower than the Doty abdomen coil. With a 10% lower filling factor (based on the voxel size), we expected only a 5% loss in SNR. With the increased length, the internal resistance r of the coil is expected to be higher, which means a lower Q factor. With having 4 more brain samples (8 brains versus 4 brains), there will be more capacitive loss caused by the interaction between the brain tissue and the coil. These factors contribute to the lower filling-factor resulting in a 10% loss in SNR.

Even with a 10% loss of SNR, the image quality still exceeded our requirements and gave us an efficiency of 45.7 that is almost double compared to the Doty abdomen coil (efficiency of 25.1).

This coil was recently used to study a newly designed Alzheimer's plaque or tangle targeted USPIO contrast agent. The main different between this contrast agent and the previous one (published) is its capacity to cross the blood brain barrier without using Manitol [19] which has certain level of toxicity to the mouse body. This coil helped to reduce the sample preparation time by half, doubled the efficiency of MRI scan time while insuring all requirements (homogeneity coverage, SNR higher than 30) were met.

Here are a few examples of scans generated using SPM Mouse toolbox by our collaborators:

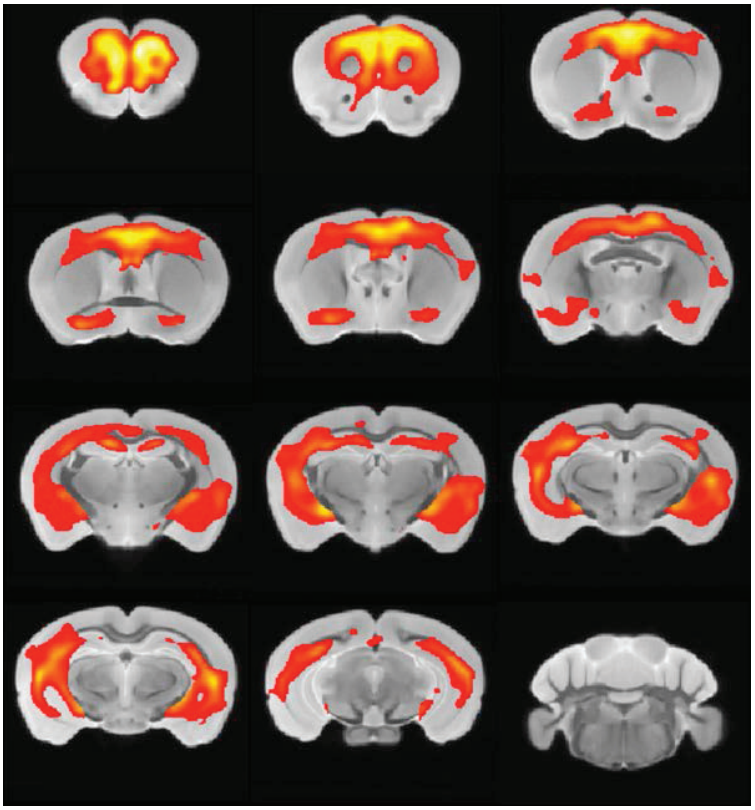

Figure III-24: *Voxel based comparison between 2 groups of mouse brains: 12 jAPP mice vs. 12 Wild-Type (WT) mice injected with PEG-USPIO. Similar to the results obtained previously with the injection of USPIO combined with Manitol, the difference between the two groups mainly shown in the areas where most of the Amyloid plaques are located.*

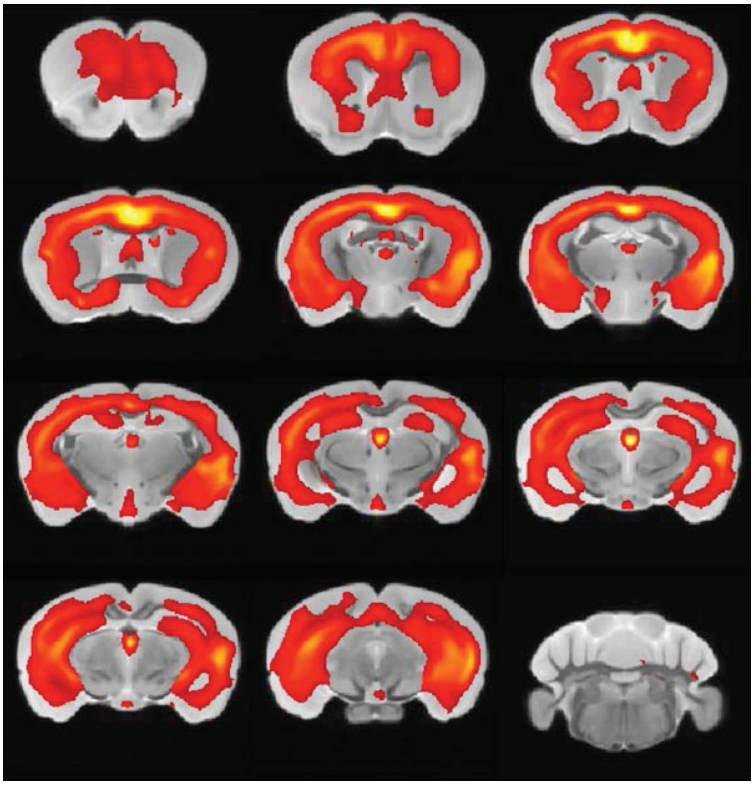

Figure III-25: *Voxel based comparison between 2 groups of mouse brains: 12 jAPP mice injected with PEG-USPIO vs. 9 tg3 mice injected with USPIO alone. The results demonstrating that the new Amyloid plaques targeting contrast agent was able to cross the Brain Blood Barrier (BBB) without using Manitol.*

VI. Increase MRI performance using low noise figure preamp

VI.1. Study the effect of noise figure on the quality of MRI images

In chapter 1, we presented an overall view of the acquisition chain of our MRI system:

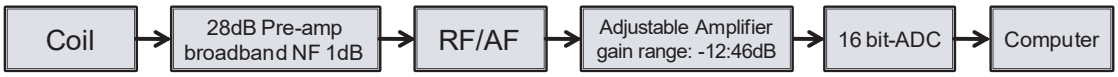

Figure III-26: *The acquisition chain of our system*

Each part of the chain has its gain and noise figure (calculated from the noise factor) which result in the SNR of the MRI images. We will examine how the gain and noise figure of each step contribute to the quality of the final images.

We use a chain of cascading amplifiers to illustrate the system:

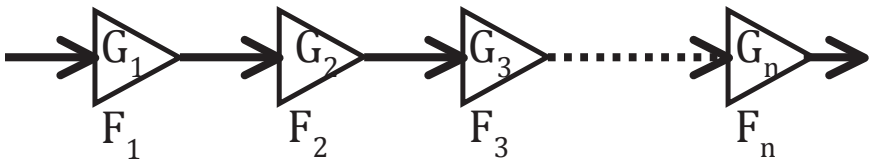

Figure III-27: *Cascaded amplifiers*

Each amplifier has a gain of G_x and a noise factor of F_x. The noise factor is defined as:

$$\mathbf{F_x = \frac{SNR_{in}}{SNR_{out}}} \qquad \textbf{(III-3)}$$

SNRin and SNRout are respectively the SNR on the input and the output of the amplifier.

The overall noise factor F of the chain is:

$$\mathbf{F = F_1 + \frac{F_2 - 1}{G_1} + \frac{F_3 - 1}{G_1 G_2} + \frac{F_4 - 1}{G_1 G_2 G_3} + \cdots + \frac{F_n - 1}{G_1 G_2 G_3 \ldots G_{n-1}}} \qquad \textbf{(III-4)}$$

From this equation, we can see that if the gain of the first stage is high enough, the noise factor of the following stages is negligible and the noise factor of the whole chain is mainly the noise factor of the first stage.

In our system, the pre-amp has a gain of 28dB that is high enough for us to neglect the effect of noise factor of the other stages. Therefore, we will focus on improving the noise factor of this stage.

VI.2. Calculation of expected SNR by cascading pre-amplifiers

The noise figure of an amplifier is defined as follows:

$$\boldsymbol{NF = 10 \log\left(\frac{SNR_{in}}{SNR_{out}}\right)} \qquad \textbf{(III-5)}$$

$\frac{\mathrm{SNR_{in}}}{\mathrm{SNR_{out}}}$ is known as noise factor (F) of amplifier. In the case of cascading amplifiers, each one has a gain G and noise factor F:

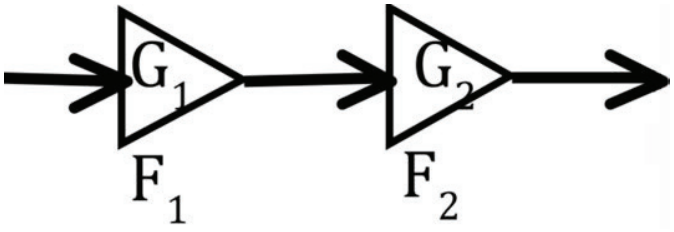

Figure III-28: *2 amplifiers in cascade*

The noise factor of the chain Fsum becomes:

$$\boldsymbol{F_{sum} = F_1 + \frac{F_2}{G_1}} \quad \text{(III-6)}$$

Because F2 is normally low (1 or 2 dB) and G1 is at least 10, we can neglect the influence of F2.

The noise figure of the first amplifier is (also imposing the NF of the system before cascading):

$$\boldsymbol{NF_1 = 10 \log\left(\frac{SNR_{in}}{SNR_{out1}}\right)} \quad \text{(III-7)}$$

By cascading 2 amplifiers and keeping the same SNR_{in}, the noise figure of the chain is (the low noise figure pre-amp is placed nearest to the coil possible, following by the pre-amp of the system, resulting in NF_2):

$$\boldsymbol{NF_2 = 10 \log\left(\frac{SNR_{in}}{SNR_{out2}}\right)} \quad \text{(III-8)}$$

By dividing (III-7) by (III-8), we obtain:

$$\boldsymbol{\frac{NF_1}{NF_2} = \frac{10 \log\left(\frac{SNR_{in}}{SNR_{out1}}\right)}{10 \log\left(\frac{SNR_{in}}{SNR_{out2}}\right)}} \quad \text{(III-9)}$$

We deduce:

$$\boldsymbol{\frac{NF_1}{NF_2} \times log\left(\frac{SNR_{in}}{SNR_{out2}}\right) = log\left(\frac{SNR_{in}}{SNR_{out1}}\right)} \quad \text{(III-10)}$$

$$\boldsymbol{<=> \quad log\left[\left(\frac{SNR_{in}}{SNR_{out2}}\right)^{\frac{NF_1}{NF_2}} \Big/ \frac{SNR_{in}}{SNR_{out1}}\right] = 0} \quad \text{(III-11)}$$

$$\boldsymbol{<=> \quad \left(\frac{SNR_{in}}{SNR_{out2}}\right)^{\frac{NF_1}{NF_2}} \Big/ \frac{SNR_{in}}{SNR_{out1}} = 1} \quad \text{(III-12)}$$

$$\boldsymbol{<=> \quad \left(\frac{SNR_{in}}{SNR_{out2}}\right)^{\frac{NF_1}{NF_2}} = \frac{SNR_{in}}{SNR_{out1}}} \quad \text{(III-13)}$$

$$<=> \quad SNR_{in}^{\frac{NF_1}{NF_2}-1} = \frac{SNR_{out2}^{\frac{NF_1}{NF_2}}}{SNR_{out1}} \qquad \text{(III-14)}$$

$$<=> \quad SNR_{out1} \times SNR_{in}^{\frac{NF_1}{NF_2}-1} = SNR_{out2}^{\frac{NF_1}{NF_2}} \qquad \text{(III-15)}$$

From equation (III.7):

$$\log\left(\frac{SNR_{in}}{SNR_{out1}}\right) = \frac{NF_1}{10} \qquad \text{(III-16)}$$

$$<=> \frac{SNR_{in}}{SNR_{out1}} = 10^{\frac{NF_1}{10}} \qquad \text{(III-17)}$$

$$<=> SNR_{in} = SNR_{out1} \times 10^{\frac{NF_1}{10}} \qquad \text{(III-18)}$$

Replace this result in the equation (III.15)

$$SNR_{out1} \times \left(SNR_{out1} \times 10^{\frac{NF_1}{10}}\right)^{\left(\frac{NF_1}{NF_2}-1\right)} = SNR_{out2}^{\frac{NF_1}{NF_2}} \qquad \text{(III-19)}$$

$$<=> SNR_{out1}^{\left(\frac{NF_1}{NF_2}\right)} \times 10^{\frac{NF_1}{10}\left(\frac{NF_1}{NF_2}-1\right)} = SNR_{out2}^{\frac{NF_1}{NF_2}} \qquad \text{(III-20)}$$

From this last equation, we have:

$$<=> \quad SNR_{out2} = \sqrt[\frac{NF_1}{NF_2}]{\left(SNR_{out1}^{\left(\frac{NF_1}{NF_2}\right)} \times 10^{\frac{NF_1}{10}\left(\frac{NF_1}{NF_2}-1\right)}\right)} \qquad \text{(III-21)}$$

This equation III-21 related the initial SNR of the original system to the new SNR could be obtained with the amplifier cascading. From this equation, if the noise figure of each amplifier is known, we could predict the SNR gain using the low noise figure pre-amplifier.

VI.3. The use of commercially available low-noise figure

In this study, we used a narrow band low noise figure (0.5dB) pre-amplifier (20dB) designed for 300MHz purchased from Advanced Receiver Research. The input and output of this pre-amp was pre-adapted to 50 ohms to optimize power transmitting:

Figure III-29: *Our low-noise figure pre-amp purchased from Advanced Receiver Research*

We replace the noise figure of each pre-amplifier into the equation (III.21) previously obtained (NF1=1dB, NF2=0.5dB). We have:

$$\boldsymbol{SNR_{out2}} = \sqrt{\left(\boldsymbol{SNR_{out1}}^2 \times \boldsymbol{10^{\frac{1}{10}(2-1)}}\right)} \qquad \text{(III-22)}$$

$$<=> \quad \boldsymbol{SNR_{out2}} = \boldsymbol{SNR_{out1}}\sqrt{\boldsymbol{10^{\frac{1}{10}}}} \qquad \text{(III-23)}$$

$$<=> \quad \boldsymbol{SNR_{out2}} \approx \boldsymbol{SNR_{out1}}\sqrt{\boldsymbol{1.259}} \qquad \text{(III-24)}$$

$$<=> \quad \boldsymbol{SNR_{out2}} \approx \boldsymbol{1.122 \times SNR_{out1}} \qquad \text{(III-25)}$$

By inserting a pre-amplifier with a NF of 0.5dB in the cascade with the preamp of the system that has a NF of 1dB, we expect a SNR gain of about 12%.

This pre-amp was first tested in our system using the homemade Litzcage head coil with 1 ex-vivo brain sample.

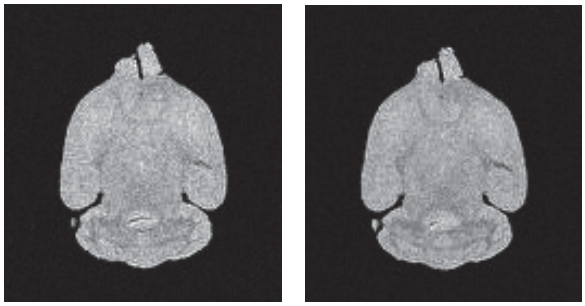

Figure III-30: *Image on the right showed improvement in image quality obtained with the low-noise pre-amplifier*

The images acquired using the low-noise figure pre-amp were clearly less noisy compared to the ones using only the pre-amp of the system. The gain in SNR obtained is about 11% that is coherent with the expected gain.

This pre-amplifier was then tested with the newly designed 8-brain coil using a 8-brain sample and compared to the images acquired from a 4-brain sample using the Doty abdomen coil (without the low-noise pre-amp). To have a fair comparison, the brains were extracted under the same conditions and on the same day.

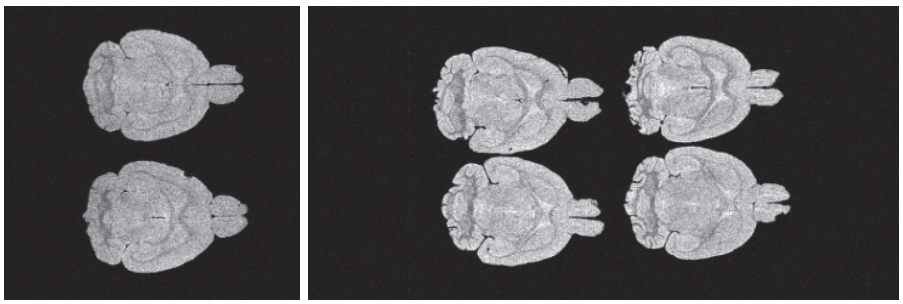

Figure III-31: *The 8-brain coil combined with the low-noise pre-amp gave us the same level of SNR compare to the Doty abdomen coil. Keep in mind that we scan 8 brains at a time instead of 4 brains.*

The SNR obtained from the Doty coil (18.1) is at the same level with the SNR from the 8-brain coil (18.2) using the pre-amp. This result is what we expected because without the pre-amp, we lost about 10% of SNR compare to the 4-brain scan with the 8-brain coil. With the pre-amp, we get back 11% of SNR that leads to about the same level of SNR of the 4-brain coil. Keep in mind that if we use the pre-amp with the 4-brain coil, we also will obtain a better SNR. But what we are interested in here is to have the same results as previous scans with higher efficiency.

In conclusion, the combination of the newly designed 8-brain coil and the low-noise pre-amp, results in the same level of SNR as previously reported while scanning twice the number of brains. This leads to double the efficiency compared to the Doty abdomen coil.

VII. Conclusion

In this study, we started with a qualitative MRI scan at low efficiency (one and two brain throughput). Progressively, we increased the throughput of our scan by developing coils

to fit multiple brains (4 brain) while insuring the same homogeneity in coverage. The quantitative statistical studies require perfect homogeneity coverage. This led us to compromise between the homogeneity of the coil and the sensitivity of the scan (lower the filling factor by increasing the volume of the coil), resulting in a lower efficiency. To take full advantage of our system and also to increase the throughput (increasing the efficiency), we designed a new structure, which has a high filling factor while insuring perfect homogeneity coverage for an 8-brain setup. Combining this coil with a low-noise figure pre-amp, we doubled the efficiency of our ex vivo MRI while taking full advantage of the unattended overnight scanning time. In conclusion, we have a wide range of coils for different needs, from qualitative studies with high SNR to quantitative studies with excellent homogeneity coverage and high efficiency:

Coil	**Dimensions** ID (mm) AD(mm) L(mm)	**Throughput** (Number of brain)	**SNR**	**Scan time** (min)	**Efficiency**
Homemade Mouse Head Coil	ID: 23.5 AD: 21.5 L: 29	1	46	110	6.2
Doty Mouse Head Litz Coil	ID: 28 AD: 26 L: 29	2	42	110	11.3
Homemade 4- brain Low-Pass Birdcage	ID: 30 AD: 28 L: 29	4	39.4	147	22.5
Homemade 4-brain Litz Coil	ID: 30 AD: 28 L: 29	4	48.7	147	27.8
Doty Abdomen Litz Coil	ID: 37 AD: 33 L: 42	4	44	343	25.1
Homemade 8-brain Dual Litz Coil	ID: 33 AD: 30.5 L: 52	8	40	343	45.7
Homemade 8-brain Dual Litz Coil With low-noise Pre-amp	ID: 33 AD: 30.5 L: 52	8	44	343	50

Figure III-32: *Table summarizing all coils available in-house for different ex vivo mouse brain MRI: from small coil for low throughput but high quality images and short scanning time to large coil with high throughput and high efficiency for an overnight scan time.*

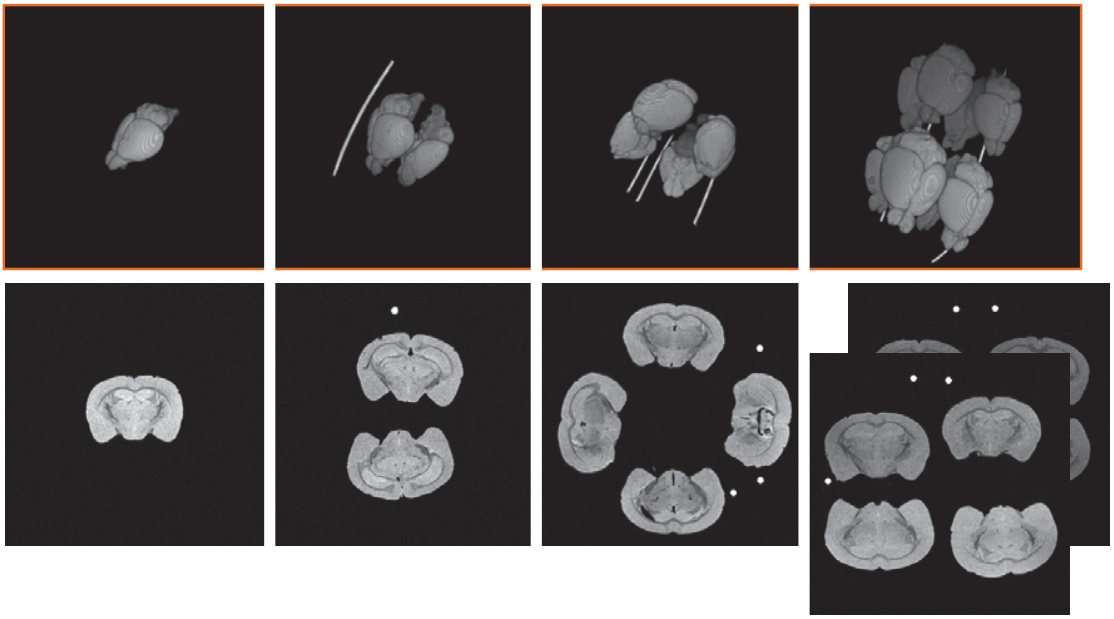

Figure III-33: *Examples of images summarizing all configurations available for ex vivo mouse brain imaging.*

References

[1] J. P. Lerch, L. Gazdzinski, J. Germann, J. G. Sled, R. M. Henkelman, and B. J. Nieman, "Wanted dead or alive? The tradeoff between in-vivo versus ex-vivo MR brain imaging in the mouse," *Front Neuroinform,* vol. 6, p. 6, 2012.

[2] A. Mackenzie-Graham, "In vivo vs. ex vivo Magnetic Resonance Imaging In Mice," *Front Neuroinform,* vol. 6, p. 19, 2012.

[3] M. S. Ramirez, S. Y. Lai, and J. A. Bankson, "A throughput-optimized array system for multiple-mouse MRI," *NMR Biomed,* Aug 10 2012.

[4] N. A. Bock, B. J. Nieman, J. B. Bishop, and R. Mark Henkelman, "In vivo multiple-mouse MRI at 7 Tesla," *Magn Reson Med,* vol. 54, pp. 1311-6, Nov 2005.

[5] T. Lanz, M. Muller, H. Barnes, S. Neubauer, and J. E. Schneider, "A high-throughput eight-channel probe head for murine MRI at 9.4 T," *Magn Reson Med,* vol. 64, pp. 80-7, Jul 2010.

[6] B. J. Nieman, J. Bishop, J. Dazai, N. A. Bock, J. P. Lerch, A. Feintuch, X. J. Chen, J. G. Sled, and R. M. Henkelman, "MR technology for biological studies in mice," *NMR Biomed,* vol. 20, pp. 291-303, May 2007.

[7] S. Xu, T. P. Gade, C. Matei, K. Zakian, A. A. Alfieri, X. Hu, E. C. Holland, S. Soghomonian, J. Tjuvajev, D. Ballon, and J. A. Koutcher, "In vivo multiple-mouse imaging at 1.5 T," *Magn Reson Med,* vol. 49, pp. 551-7, Mar 2003.

[8] P. McConville, J. B. Moody, and B. A. Moffat, "High-throughput magnetic resonance imaging in mice for phenotyping and therapeutic evaluation," *Curr Opin Chem Biol,* vol. 9, pp. 413-20, Aug 2005.

[9] S. D. Bamforth, J. E. Schneider, and S. Bhattacharya, "High-throughput analysis of mouse embryos by magnetic resonance imaging," *Cold Spring Harb Protoc,* vol. 2012, pp. 93-101, Jan 2012.

[10] X. Zhang, J. E. Schneider, S. Portnoy, S. Bhattacharya, and R. M. Henkelman, "Comparative SNR for high-throughput mouse embryo MR microscopy," *Magn Reson Med,* vol. 63, pp. 1703-7, Jun 2010.

[11] Y. Z. Wadghiri, G. Johnson, and D. H. Turnbull, "Sensitivity and performance time in MRI dephasing artifact reduction methods," *Magn Reson Med,* vol. 45, pp. 470-6, Mar 2001.

[12] Y. Z. Wadghiri, D. M. Hoang, T. Wisniewski, and E. M. Sigurdsson, "In vivo magnetic resonance imaging of amyloid-beta plaques in mice," *Methods Mol Biol,* vol. 849, pp. 435-51, 2012.

[13] J. Yang, Y. Z. Wadghiri, D. M. Hoang, W. Tsui, Y. Sun, E. Chung, Y. Li, A. Wang, M. de Leon, and T. Wisniewski, "Detection of amyloid plaques targeted by USPIO-Abeta1-42 in Alzheimer's disease transgenic mice using magnetic resonance microimaging," *Neuroimage,* vol. 55, pp. 1600-9, Apr 15 2011.

[14] J. Zhang, P. Yarowsky, M. N. Gordon, G. Di Carlo, S. Munireddy, P. C. van Zijl, and S. Mori, "Detection of amyloid plaques in mouse models of Alzheimer's disease by magnetic resonance imaging," *Magn Reson Med,* vol. 51, pp. 452-7, Mar 2004.

[15] F. D. Doty, G. Entzminger, J. Kulkarni, K. Pamarthy, and J. P. Staab, "Radio frequency coil technology for small-animal MRI," *NMR Biomed,* vol. 20, pp. 304-25, May 2007.

[16] F. G. Woermann, S. L. Free, M. J. Koepp, S. M. Sisodiya, and J. S. Duncan, "Abnormal cerebral structure in juvenile myoclonic epilepsy demonstrated with voxel-based analysis of MRI," *Brain,* vol. 122 (Pt 11), pp. 2101-8, Nov 1999.
[17] M. Suzuki, S. Nohara, H. Hagino, K. Kurokawa, T. Yotsutsuji, Y. Kawasaki, T. Takahashi, M. Matsui, N. Watanabe, H. Seto, and M. Kurachi, "Regional changes in brain gray and white matter in patients with schizophrenia demonstrated with voxel-based analysis of MRI," *Schizophr Res,* vol. 55, pp. 41-54, May 1 2002.
[18] T. W. Moorhead, V. E. Gountouna, D. E. Job, A. M. McIntosh, L. Romaniuk, G. K. Lymer, H. C. Whalley, G. D. Waiter, D. Brennan, T. S. Ahearn, J. Cavanagh, B. Condon, J. D. Steele, J. M. Wardlaw, and S. M. Lawrie, "Prospective multi-centre Voxel Based Morphometry study employing scanner specific segmentations: procedure development using CaliBrain structural MRI data," *BMC Med Imaging,* vol. 9, p. 8, 2009.
[19] J. Reith, A. Ermisch, N. H. Diemer, and A. Gjedde, "Saturable retention of vasopressin by hippocampus vessels in vivo, associated with inhibition of blood-brain transfer of large neutral amino acids," *J Neurochem,* vol. 49, pp. 1471-9, Nov 1987.

Chapter IV: Evaluation of Coils for Imaging Histological Slides: SNR and Filling Factors

Introduction

In MRI research for small animal, it is important to confirm/validate finding results. The best approach is to compare MRI data with histology of the same sample. The standard validation approach is as follow:

Despite these great advantages, the co-registration steps between MRI images and histological sections obtained through light microscopy have presented important practical challenges [1-5]. The main difficulties encountered during the validation steps stem from both the slice section misalignments and the significant difference in slice thicknesses between sub-millimetric in vivo MRI (ranging from 100-µm to 1-mm thickness) and histology sections (thicknesses commonly ranging from 5-µm to 100-µm). These limitations have been partially addressed by acquiring three-dimensional (3D) ex vivo imaging of excised and perfused organs of interest. The scanning is usually assessed over long imaging times using a dedicated coil closely fitting the sample to improve the sensitivity [6-20]. The accumulation of repeated scans results in motion free and highly resolved 3D MRI datasets enabling a precise virtual realignment of the image slice of interest to closely match the physical histology section [21-26].

However, important discrepancies remain between these two analyses [22]. These notable differences can be attributed to sample changes associated with postmortem tissue processing due to fixation and dehydration resulting in tissue deformation, as well as artifacts caused by sectioning and the chemicals used during the staining process [27-33]. These discrepancies have been addressed using time-consuming post-processing techniques when establishing 3D atlases [21-24]. But this approach may be more difficult to systematically implement for every existing transgenic mouse line or murine disease model due to limited resources or lack of image post-processing expertise.

All these differences create a great gap between MRI and histology and might lead to important mismatches. To fill this gap, we proposed to add an additional step in our

validation approach called histology MRI that allows direct MRI on histology tissue sections therefore leads to the possibility of perfect match:

In this work, we investigate the relative gain in sensitivity of five histology coils designed in-house compared to commercial mouse head coils. The coil set was tailored to house tissue sections ranging from 5 □m to1000 □m encased in either glass slides and/or coverslips. Our simulations and experimental measurements showed that although the sensitivity of this flat structure consistently underperforms relative to a birdcage head coil based on the gain expected from their respective filling factor ratios, our results demonstrate it can still provide a remarkable gain in sensitivity. The increase in filling factor achieved overcomes the losses associated with electric leaks inherent to this structure, leading to a 6.7 fold improvement in performance for the smallest structure implemented. Alternatively, the largest histology coil design exhibited equal sensitivity to the mouse head coil while nearly doubling the radiofrequency planar area coverage. Our study also describes preparation protocols for freshly excised sections, as well as pre-mounted tissue slides of both mouse and human specimens. Examples of the exceptional level of tissue detail and the near-perfect MRI to light microscopic image co-registration are provided.

I. Coil setups for histology MRI

I.1. Inductive coupling using wire loop

This coil setup was proposed by Nabuur et *al* [34]. In this design, a simple wire loop was pre-tuned to a frequency close to the functional Larmor frequency 400Mhz of the MRI scanner using a non-magnetic variable capacitor (396MHz in the case of 9.4T scanner used in this paper). Dimension of this loop was defined by the size of the tissue of interest. As the tissue sample used in this paper is of 60um thickness and about 12 x 12 mm in-plane dimension, the loop was made in square shape with edges of 15 mm. The dimension of the loop was chosen to have the length of each side 20% larger than the histological slice to avoid the B1 field inhomogeneity caused by the hot spot (the wire). This wire loop was placed closely to the histological tissue. This ensemble of tissue and surface coil was then carefully positioned to the center of a commercial birdcage coil (Bruker, ID: 25 mm). The tuning and matching of the whole system was done through the birdcage coil. The birdcage volume coil was used as transmitter in the transmitting phase and also to transmit the MR signal from the tissue to acquisition system by inductive coupling through the surface wire loop in the receiving phase.

In this setup, in the transmitting phase, the tissue is excited by the B1 RF magnetic field generated by the volume coil. During the receiving phase, the magnetic energy stored in the tissue sample will be released and convert to a current circulates inside the wire loop. This electrical energy in turn will be transferred to the acquisition through the volume coil through a mutual inductance between the 2 coils (inductive coupling).

This coil setup takes advantage of the RF homogeneity of the birdcage structure and improves the overall filling factor through the use of the surface coil. Compare to the linear birdcage volume coil by itself (used in this paper), this coil setup help to improve the sensitivity up to 3.8 fold which corresponds to a gain 15 fold in scanning time. If we are to compare this setup to a circular polarized birdcage coil (41%) more sensitive than a linear birdcage coil, this setup only help to improve about 2.7x in SNR gain.

I.2. Flat U-Shaped RF coil

The previous setup proved to gain already tremendously in sensitivity compare to a standard whole mouse head coil through the gain in filling factor using the wire loop. The surface wire loop is an open structure that has an advantage of no limitation in sample thickness. But also because of its open structure, the filling factor is difficult to be estimated and also not optimized.

Alternatively, Meadowcroft and colleagues proposed a unique RF coil design based on a flat U-shaped structure that closely matches the planar nature of a histological tissue sample providing the most optimal filling factor [35, 36]. The authors demonstrated excellent RF homogeneity throughout the region of interest (24 x 24 mm) within the coil cavity designed to house a sample encased on dual glass coverslips. The length (L) of the coil was doubled (L=48 mm) by inserting an equal-sized Teflon spacer between the two flat copper strips next to the U-shaped cavity leading to the driving port. The presence of this spacer both provided some distributed capacitance and allowed for the current to distribute throughout the strip before reaching the sample cavity from the connections to the tuning capacitor.

Although the sensitivity of this new probe design was not compared to other commonly available RF coil structures, the authors demonstrated their ability to acquire highly detailed MRI images from 60 μm sections of freshly mounted tissue encased by two coverslips. This setup enabled the accurate correlation between MRI and light microscopy by direct imaging of post-mortem tissue samples from either human Alzheimer's Disease (AD) subjects or mice of a strain exhibiting some characteristics of AD [36].

Our work is to extend the application of this coil setup to accommodate both wider and thicker tissue slides with our in-house histology MRI coil design and to compare it's performance to conventional commercially available mouse head coil (both volume and surface coil). All newly designed RF histology resonators were systemically characterized by mapping their RF homogeneity and examining how each performed against commercially available surface and whole mouse head coils. In addition, we

examined the effect of the spacer on the resulting coil sensitivity by replacing the Teflon with either air or glass as alternative insulators.

We intended to image both freshly mounted tissue and pre-mounted specimens originating from either paraffin embedding or cryo-sections having thicknesses ranging from 5 μm to 1000 μm. To this effect, our study investigated the best conditions for sample preparation for either case in order to minimize MR image artifacts.

II. Our in-house flat U-shaped RF coil design for histology MRI

A 3.2-inch wide copper adhesive tape (76555A726, McMaster.com, Robbinsville, NJ, USA) was used for the design of all coils considered in this study. To be perfectly parallel to each other the resulting copper strips were carefully cut and fixed on Plexiglas supports (Acrylite® FF 000-9 OP-3, Evonik Industries, Parsippany-Troy Hills, NJ, USA). Additional caution was taken during this step of the design in order to insure a homogenous RF field by obtaining both bubble-free even surfaces and an equidistant gap opening between the flat conductors. The specific height of the sample insertion gap was achieved by designing in-house low permittivity spacers using Teflon. For each coil, the spacer thickness was defined by using layers of Teflon tapes (7346A15, McMaster.com, Robbinsville, NJ, USA) (Figure IV-1, 2 &3). Similarly, a glass-based spacer was also fabricated in-house using layers of stacked #1 glass coverslips (individual thickness ranging from 130 μm to 170 μm) to achieve the overall desired glass height.

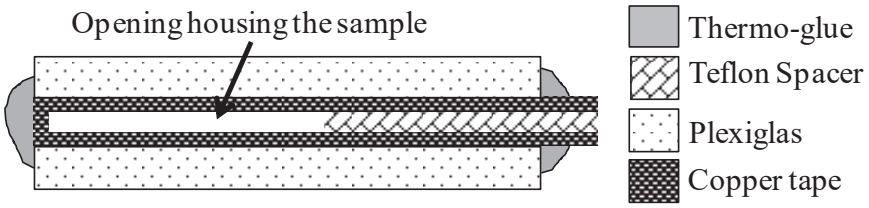

Figure IV-1: *Histology coil assembly: The schematic illustrates the simplicity of our coil assembly. The rigidity of the planar copper tape conductor is insured by taping a rectangular piece of Plexiglas in each outer side of the loop with the overall structure permanently secured using thermo-glue. The thickness of the layered Teflon spacer placed between the flat copper conductors dictates the height of the opening creating a gap to insert the sample. Neither the Plexiglas nor the thermo-glue are expected to interfere with the electrical performance of the coil structure or contribute to the MR signal.*

Prior to interfacing each coil to a dedicated turning/matching (T/M) network, all RF resonators were pre-tuned to an upper frequency using a non-magnetic fixed ceramic capacitor (ATC Corp., Huntington Station, NY, USA). The designated final Larmor operating frequency (here 301MHz) was subsequently achieved with the turning/matching (T/M) network. The homemade RF shielded T/M circuit design was based on two non-magnetic capacitive trimmers (range 0.6 to 10 pF; NMKP10HVE, Voltronics Corps., Salisbury MD, USA) (Figure IV-2) integrated within a dedicated holder [37]. Ease of histology coil interchange was achieved via a BNC connector connected to a 3-cm long double-shielded coaxial cable (RG-223/U, Alpha Wire Com., Elizabeth, NJ, USA; capacitance 101-pF/meter) to minimize cable losses with capacitance seen by the T/M circuit equivalent to ~3-pF.

The short coaxial length was chosen to minimize cable losses while enabling an adequate distance from the T/M box to prevent static magnetic field perturbation around the sample. The resonance of each histology probe was fine adjusted with a Network Analyzer (VIA Echo MRI, AEA technology, Inc., Carlsbad, CA, USA) using the reflection mode (S11) [38].

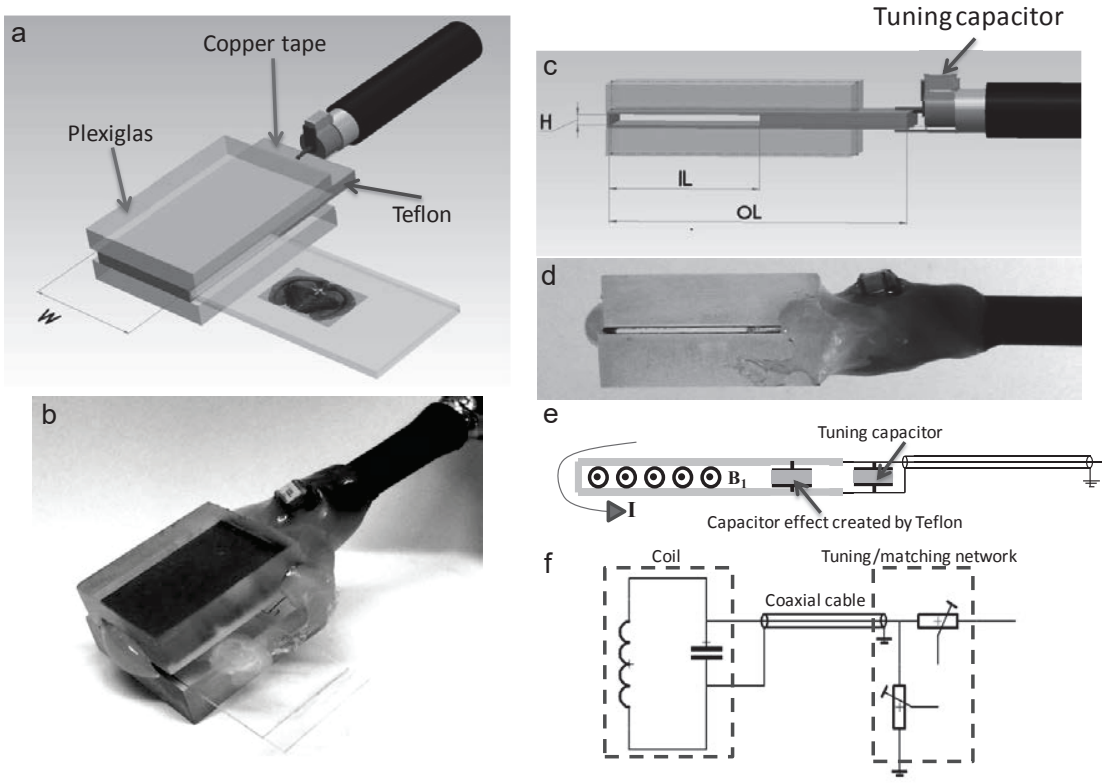

Figure IV-2: *Principle and overview of the histology slide probe: a) Schematic of the planar coil structure to accommodate histology tissue section. The choice of the width (W) defines the extent of the homogeneous RF field of interest covering the tissue sample to be imaged within a slide. b) The height (H) of the opening was chosen to insert a tissue encasing slide setup to accommodate the pairing of either a glass/coverslip (~1350 µm) or two coverslips (~450 µm). The inner length (IL) comes in two dimensions to house commercially available 12-mm width coverslips or 25 mm width slides. The resulting outer length (OL) of the probe is approximately twice the IL as prescribed by Meadowcroft et al. (2007). For the sake of simplicity of the design, the construction of the structures described in this work was made in-house using thermo-glue as in (b&d). e) The current traversing the slotted resonator induces a transverse B_1 RF field after crossing a square Teflon-based capacitive insert extending throughout the whole unused but required outer length of the coil. f) The tuning/matching (T/M) of all the probes is insured by two variable capacitors (Voltronics Corps., Salisbury MD, USA) via a double shielded coaxial cable. All probes can be easily interchanged with the same T/M circuit.*

III. Histology RF coil characterization

III.1. Filling factor (η)

As described in chapter I, the filling factor has been expressed as a ratio of the volume of the sample to the volume of the coil assuming a homogeneous coil RF field [39]. Traditionally this has been expressed as a ratio of the volume of the sample to the volume

of the coil assuming a homogeneous coil RF field [38]. In practical terms this translates into fitting the coil closely to the sample of interest to achieve a high filling factor. However, in our study the need and challenges associated with measuring the effective sample volumes were circumvented by evaluating the filling factor relative to a circularly polarized (CP) commercially available whole mouse head Litz coil (Inner Diameter (ID) =28 mm, accessible ID = 26 mm, Length (L) =29 mm, Doty Scientific, Columbia, SC, USA). Using this as a reference throughout this study eased the practical calculation of the relative filling factor η_R as the ratio between the inner volumes of each histology coil and the mouse head coil irrespective of the sample size. With this approach, we assumed that the inner volume of each coil is similar to their effective RF B_1 volume. The Doty mouse head Litz coil, providing the largest RF volume was set as our baseline, leading to a normalized unitary filling factor η_R. However, this evaluation was not feasible with the surface coil due to its open structure, shape and the inhomogeneous nature of the RF field.

III.2. Quality factor

The electrical quality factor (Q), a measure of the contribution of power losses, was systematically measured for each coil tuned at 301 MHz and matched to 50 Ω both unloaded (QU) and loaded (QL) using a 60 □m tissue section as the sample load. The Q was measured with a network analyzer (Hewlett Packard 4396A) based on the reflection mode method [38]. However, two of the commercial Bruker coils considered in this study, were equipped with dedicated RF connectors that did not permit an assessment of their characterization under the same conditions used on the other probes. Similar to η_R, the relative quality factor (Q_R) was also calculated as the ratio of Q_L in each histology coil to that of the mouse head probe. The Q_R was assessed using our comparative characterization to account for the effect of Q_L on the resulting performance of each probe.

III.3. RF Coil Sensitivity

The characterization of the sensitivity against the gain in filling factor for all the coils was assessed relative to the whole mouse head CP probe - considered as our point of

reference - with 100% sensitivity and a relative filling factor of η_R=1. This was translated experimentally using a 1-mm thick brain tissue section encased in two coverslips to provide the greatest SNR achievable for the following coils, each capable of housing this sample size: 1) the two histology coils designed to accommodate glass slides, 2) a Bruker whole mouse head CP birdcage coil (ID=24.5 mm, L=28 mm, Model No. 1P T20063V3, referred as 'Bruker head coil') and 3) a Bruker 2-channel phased array receive-only mouse head surface coil (Model No. 1P T11204V3 referred as Bruker surface coil. The latter is a rectangular shaped probe (27 mm along X-direction × 19 mm along Z-direction) curved around a cylinder (ID=25 mm). A 60 µm thick tissue section encased between two 12 mm x 24 mm coverslips was considered for the comparative performance of the three remaining histology coils. To account for the effect of quadrature detection in the commercial coils compared to the linear nature of the histology coils, the sensitivity of the volume coils and projections with η were also divided by 1.4.

III.4. Dielectric constant (ε)

The dielectric constant ε was determined using a Hewlett Packard 4396A Network Analyzer equipped with a dielectric material test fixture (Hewlett Packard 16453A) based on the following equation:

$$\varepsilon_d \approx \frac{C_d \times d_d}{A \times \varepsilon_0} \qquad \text{(IV-1)}$$

in which Cd is the measured capacitance of the spacer at 301 MHz, dd is the thickness of the spacer, and A, the overlapping area between the conductive plates. εo is known as the vacuum permittivity or electrical constant (≈8.854187817620...× 10−12 F·m−1). The calibration of the instrument was run prior to each measurement session according to the recommendations of the instrument's manufacturer using the calibration kit that includes a dielectric PTFE device of known characteristic (ε=2.1).

Several spacer slabs were produced by stacking Teflon tape (ref. #7346A15, McMaster.com, Robbinsville, NJ, USA, thickness ~50-µm) over multiple layers compressed to form thicknesses ranging from 450-µm (~10 layers) to 1,350-µm (~30

layers). This resulted in a lower dielectric constant measurements ranging from 1.7 - 1.9. These values near foam Teflon characteristics (ε~1.6) [40] suggesting the likely contribution of air within the compressed layers.

When examining commercial glass slides (ref: 12-550-15, FisherBrand®) or coverslips (ref.:3312, Gold Seal® or ref.:12-548-5M, Fisherfinest® Premium), both surface-treated with a moisture resistance coating, the measurement led to ε=4.7 ±0.2 for a 1-mm thick glass slide and ε=2.9 ±0.3 for coverslips ranging from 130-µm to 170-µm thicknesses. Stacking 3-coverslip resulted in ε=2.7±0.2. Comparatively, conventional borosilicate glass widely used for laboratory glassware and standard slides has dielectric properties ranging from 4.9 to 5.3 when non-treated [41] and nearing ε~3.0-3.5 for carbon-doped [42, 43] or Fluorine-doped [44, 45] silica. The dielectric constants measurements of the various glass materials used in our study were reproducible with less than 10% variation showing an important difference between glass slides and coverslips (~38%). This difference may be due to the nature of the glass and coating. In contrast, we measured very little effect (less than 7%) when stacking coverslips suggesting the small contribution of the air present between glass layers.

III.5. RF homogeneity evaluation

VII.1.1 Phantom preparation:

The phantoms used in this study to qualitatively assess the overall RF homogeneity of each coil were based on an adhesive film for micro-plate (3501, Thermo Electron Corporation, Milford, MA, USA). While a simple square cut was sufficient for the smallest coil, larger phantoms required equally spaced punched holes to insure the even spread of the 5mM Gd-DTPA doped water throughout the surface of the RF coil coverage.

VII.1.2 Signal intensity mapping:

The homogeneity of the RF field for each coil was qualitatively assessed with the Gd-doped water phantom described above and using an ImageJ macro developed in-house to map color-coded contour profiles of the signal intensity. The pixel-based color map was

calculated experimentally as the relative deviation of the signal intensity of a gradient echo sequence normalized to the average signal measured from an ROI at of the center of the coil or in its vicinity when not possible. Based on common practice, the uniformity of the coil (mapped in green) was defined within 10% of the signal intensity at the center of the coil [46]. Signals deviating by more than 10% from the center were binned by 5% increment and mapped accordingly using the color scale depicted in figure 2.

IV. Sample preparation protocol

IV.1. Fresh tissue sectioning and mounting:

For samples obtained from freshly excised tissue, all C57 black wild type mice were sacrificed by means of an intravenous (IV) injection of sodium pentobarbital (Nembutal, 200-mg/kg) prior to transcardial perfusion with phosphate buffered saline (PBS) solution followed by buffered 4% paraformaldehyde in cold PBS to fix the tissue. Whole organs were extracted, fixed in buffered 4% paraformaldehyde for 24-hours and then placed in PBS for more than 8 weeks to minimize the variability of the physicochemical properties of the fixed tissues and the corresponding tissue relaxivities [47]. Samples were then immersed in graded sucrose solutions for progressive dehydration over 48-hours. Cryo-sections were obtained using a LEICA CM3050S cryostat with slice thicknesses ranging from 30-µm to 60-µm. All slices were stored in Cryo-Protectant [48] under −80oC for long term preservation.

Sections were brought to room temperature 2 hours prior to imaging. This time allowed for sample rehydration using a buffer solution and final sample preparation. The buffer solution used for tissue rehydration was first degassed in a 5 cm Petri dish placed in a small vacuum chamber for 30-minutes. Sectioned tissue samples were then immersed in the degassed buffer solution placed under a 1.5-Hz shaker for an additional 30 minutes. This step proved crucial to wash out the impurities within the tissue, thus minimizing the formation of micro-bubbles that can be detrimental to the MR image quality. The degassed tissue was mounted on a coverslip or glass slide and surrounded whenever space allowed with Fomblin (Solvay Solexis Inc., Thorofare, NJ, USA) as a hydrophobic

interface to contain the water within the rehydrated tissue. Fomblin was also chosen for its excellent susceptibility while minimizing the MR background signal.

A second coverslip was used to sandwich and seal the tissue, thereby preventing dehydration during MR imaging. The overall resulting sample thickness was less than 400 µm for a 100-µm tissue section encased between two coverslips and less than 1250-µm for a glass slide/coverslip combination. The overall glass encasing was fixed together using a small amount of super glue gel (Loctite, Henkel Consumer Adhesives Inc., Bridgewater, NJ, USA) on the 4 corners of the slides, away from the sample, to prevent perturbing the main magnetic field in the vicinity of the tissue.

Large tissue samples that covered much of the slide precluded the use of Fomblin. Instead a thick solution of DePeX mounting medium Gurr® (VWR Int'l Ltd., Ballycoolin, Dublin 15, Ireland) was spread around the extremities of the encasing as an alternative to insure effective sealing.

IV.2. Pre-mounted tissue

Tissue sections that were already mounted within a coverslip/glass slide setup required additional steps for sample preparation. The glass slide was first removed by soaking sample in Xylene (Ref.: X3P-1GAL, Fisher Chemical, Pittsburgh, PA, USA) for three days. The resulting unprotected section remained mounted on the glass slide and was then immersed and rehydrated in degassed PBS for 1-hour before protective re-encasing with a #1 coverslip using the identical steps to the fresh tissue mounting protocol.

V. MRI data acquisition

V.1. MRI system

All MRI scans were performed on a 7T micro-MRI system consisting of a 7-Telsa 200-mm horizontal bore magnet (Magnex Scientific Ltd, Yarnton, UK) equipped with an actively shielded gradient coil (BGA-9S; ID 90-mm, 770-mT/m gradient strength, 100-µs rise time) interfaced to a Bruker Biospec console.

V.2. MRI pulse sequences:

For the rapid and qualitative evaluation of the RF homogeneity using the doped water phantoms, a 2D spoiled gradient recalled (2D-SPGR) sequence with 100-µm resolution was used with the following parameters: TR/TE=50 ms/10 ms, FOV=5.12 cm x 5.12 cm, matrix=512 x 512, NA= 16, Flip Angle (FA)= 50o and imaging time of 6 min., 49 sec.

A 2D multi-gradient echo (2D-MGE) was used to acquire an echo train within the same TR and generate a T2*-weighted data set through four echo-averages with the following parameters: TR=100 ms, TE=3.2 ms. Echo spacing (ES) was varied to maximize tissue contrast based on the properties of the sample examined. The bandwidth (BW) was set to 293 Hz/pixel. The FA was adjusted to maximize SNR by reaching the empirical Ernst angle (EA) [49] in each experiment to account for the sample preparation and tissue shelf life. When faced with duty cycle limitations for T_2*-weighted imaging with the highest spatial resolution, a single echo 2D-FLASH was used instead to sequentially acquire the varying TEs empirically imposed by the tissue sample. For T1-weighted MRI, keeping all parameters constant (TR=100-ms, BW: 293Hz/pixel.), TE was set to the minimum and FA was empirically adjusted to maximize the tissue contrast while ensuring an overall SNR over the entire tissue of greater than 40 (SNR measurement described in the data analysis). This was achievable by acquiring a series of low spatial resolution images (200-µm in-plane) followed by a ROI-based analysis to accordingly adjust the number of averages (N_{Av}) for a 10-hour imaging time for an overnight unattended scan.

Both matrix and FOV settings were varied depending on the dimensions of the samples leading to an in-plane resolution ranging from 30-µm to 100-µm.

VI. Histology

All the histological images were acquired using a Leica BM 5000 B microscope (Buffalo Grove, IL, USA) equipped with 5× magnification apochromatic zoom lens. The images were captured using a CX 9000 CCD digital camera (MBF, Williston, VT ,USA) interfaced to a PC graphic workstation using the Picture Frame software (Optronics, Santa Barbara, CA, USA). The images were stitched together using Photoshop CS5 (Adobe, Seattle, WA, USA).

VII. Data analysis:

All the acquired images were examined and analyzed using ImageJ freeware (NIH, Bethesda, MD, USA). The SNR was calculated as the ratio between the mean signal intensity of a region of interest (ROI manually defined by the user) and the standard deviation of the background noise (ROI drawn in the corner of the image away from any ghosting artifacts).

VIII. Results

VIII.1. In-house developed histology RF coil set

The design of our histology coil was based on off-the-shelve materials requiring a simple construction as depicted in Figure IV-2. The assembly was made in-house using Plexiglas as a support, copper tape to conduct the current, and thermo-glue to keep the structure together as shown in Figures IV-2 b and d. The size of the resulting planar coil structure was dictated by the size of the tissue sections examined, as well as by the width and thickness of the glass support available. For samples encased by two coverslips, a coil with an opening height of 450 µm housed sections as thick as 130 µm. The surface area covering the imaging of the tissue depended on the width (W) of the flat copper strip (Figure IV-2 a).

For this work, three widths (W=12 mm; 26 mm and 52 mm) were chosen to image a variety of tissue sections ranging from organ sub-sections from the mouse olfactory bulb to large samples such as whole mouse organ slices or human specimens. The 150 µm thick glass coverslips used in our study were either 12 mm or 24 mm wide resulting in the design of coils with the same corresponding inner length of the insert (IL=12 mm and 24 mm) in order to accommodate the encased samples (figure IV-2 c). The U-shaped slotted resonator outer length (OL) was extended by an adequate length of the Teflon-based capacitor to ensure the even spread of the surface current within the copper tape before reaching the edge of the opening. The choice of a capacitor of equal length to the IL of the insert was based on Meadowcroft et al.'s simulation [35]. The adjustment of the resonance frequency was achieved by a homemade tuning/matching (T/M) circuit based on two variable capacitors (Voltronics Corps., Salisbury MD, USA) (Figure IV-2 f). Our

setup was designed to ensure that all of our probes could easily interface the same T/M circuit via a RG223 double-shielded coaxial cable using a BNC connector.

The combination of the various dimensions (W, IL, OL and H) led to the design of five distinct histology coils comprised of three planar coil dimensions (W x IL, referred to as Small: 12-mmx12-mm; Medium: 26-mmx24-mm; and Large: 52-mmx24-mm respectively) as depicted in Figure IV-3 a.

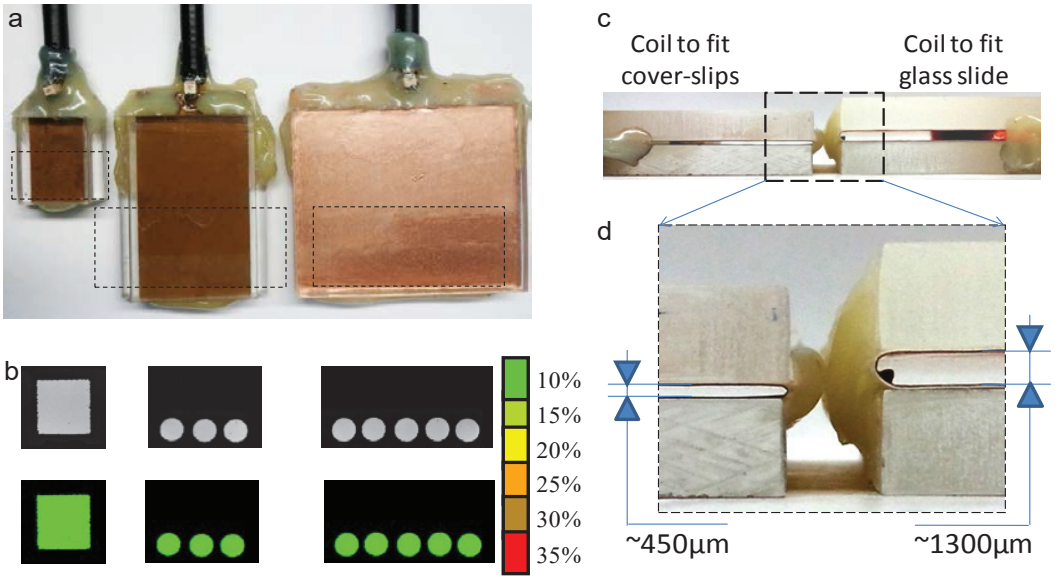

Figure IV-3: *A set of five histological slide coils were developed to accommodate both different sample sizes and slide setup. a) The coils were designed in three sizes to house encasing based on dual coverslips for tissue sections up to 100 µm thick (insert H≈450 µm). The smallest coil (left: W=IL=12 mm, OL=24 mm) was designed to insert 24 mm x 12 mm coverslips. The middle coil shown is of similar size (W=26 mm, IL=24 mm, OL=48 mm) to the structure previously reported (35) to enable the partial examination of standard size slides (50 mm x 24 mm). The larger structure (W=52 mm, IL=24 mm, OL=48 mm) shown at right permits the full coverage of slides of the same size. b) Another two coils with identical size to the two largest probes were additionally designed with a greater height (H≈1350 µm instead of H≈450 µm) to fit the coverslip/glass slide set up. c) All the coils proved to have an excellent RF planar homogeneity assessed experimentally using MRI with a phantom composed by a thin layer of water doped with 2.5 mM Gd-DTPA sandwiched between two coverslips. As indicated in the color scale, the green level represents less than 10% deviation from the average signal intensity measured by the ROI outlined in the map (white dashed line).*

The systematic choice of OL= 2xIL demonstrated a homogeneous RF field coverage throughout the cavity housing the tissue sample for all the coils (Figure IV-3 b). Two

opening heights (H=450-µm and 1350-µm) were included in the coil set to enable the insertion of either two type of encasing (slide or dual coverslip) covering tissue thicknesses ranging from 5-□m to 1000-□m (Figure IV-3 c-d).

VIII.2. Characterization and Sensitivity of the histology coils

In order to gauge the gain in performance of all the MRI probes designed for this study relative to a standard small animal coil setup such as a mouse head imaging setup, we systematically characterized the η_R, Q_U, Q_L and Q_R for each RF resonator when possible and conducted a comparative evaluation of their relative sensitivity SR as summarized in Figure IV-4. The S_R evaluation was made by calculating the effective SNR ratio between each coil and the reference head coil described previously (see above) using the same sample and normalized to 100% sensitivity for filling factor of unity. A 6.7 fold gain in sensitivity was obtained with the smallest histology structure, which accommodated tissue sections ranging in thickness from 5-µm to 100-µm. This significant performance enhancement was achieved predominantly thanks to the gain in filling factor and a marginal improvement of the Q factor in comparison to larger histology structures.

RF MRI Probe	η_R (Relative to commercial mouse head coil)	Q_u (Unloaded - Air)	Q_L (Loaded with Mouse Brain tissue section)	Q_R (Relative to commercial mouse head coil)	Sensitivity (S_R) (Measured SNR ratio relative to commercial mouse head coil)
Doty Mouse whole Head Probe (Doty Scientific Inc.) ID=28-mm, L=29-mm	1.0	145.0	145.0	100%	100%
Bruker Mouse whole Head Probe (Bruker Biospin) Bircage CP coil ID=24.5-mm, L=28-mm, Model No. 1P T20063V3	1.3	*	*	*	111%
Bruker Mouse Head Surface Probe (Bruker Biospin) 2-ch phased array Coil (Model No. 1P T11204V3) W_X=27-mm, L_Z=19-mm,curvature ID=25-mm.	**	*	*	*	226%
Large Glass Slide coil Insert: W=52-mm, IL=24-mm,H=1,350□m. Overall Length: W=52-mm, OL=48-mm.	5.6	83.0	83.0	57%	117%
Medium Glass Slide coil Insert: W=26-mm, IL=24-mm,H=1,350□m. Overall Length: W=26-mm, OL=48-mm.	12.2	102.0	102.0	70%	199%
Large coverslip coil Insert: W=52-mm, IL=24-mm,H=450□m. Overall Length: W=52-mm, OL=48-mm.	14.7	86.0	86.0	59%	208%
Medium coverslip coil Insert: W=26-mm, IL=24-mm,H=450□m. Overall Length: W=26-mm, OL=48-mm.	31.8	104.0	104.0	72%	321%
Medium coverslip coil (Glass spacer) Insert: W=26-mm, IL=24-mm,H=450□m. Overall Length: W=26-mm, OL=48-mm.	31.8	98.0	98.0	68%	238%
Medium coverslip coil (Air gap spacer) Insert: W=26-mm, IL=24-mm,H=450□m. Overall Length: W=26-mm, OL=48-mm.	31.8	106.0	106.0	73%	308%
Small coverslip coil Insert: W=12-mm, IL=12-mm,H=450□m. Overall Length: W=12-mm, OL=24-mm.	132.3	115.0	112.0	77%	670%

Figure IV-4: *Summary of the main physical coil dimensions, the geometrical sample matching via the relative filling factor* η_R *as well as the RF characteristics* (Q_U, Q_L and Q_R) *of all the coils considered in this study. The measured sensitivity of each resonator is reported relative to a commercial coil (here a mouse head coil from Doty Scientific, Inc) used as a reference. Some of the characteristics for the commercial Bruker coils are not reported due to our inability to measure the corresponding parameters under the same conditions due to the electrical circuit setup (*) or to the open nature of the surface structure generating an inhomogeneous RF field (**).*

A comparison of the S_R sensitivity for all the probes relative to their filling factor was also established as a plot in Figure IV-5. The continuous line shows the theoretical increase in sensitivity that would result from the reference head coil (filled circle, η_R =1, S_R=100%) relative to the gain in filling factor η_R projected for this structure. The η_R was varied within the achievable range by the various RF histology coils constructed. The resulting plot was inferred using eq. I-2 (sensitivity factor of MR/MR coil $S_{RF} = K\times\sqrt{\eta\times Q}$, chapter I) and the assumption that the Q factor effect remained unchanged.

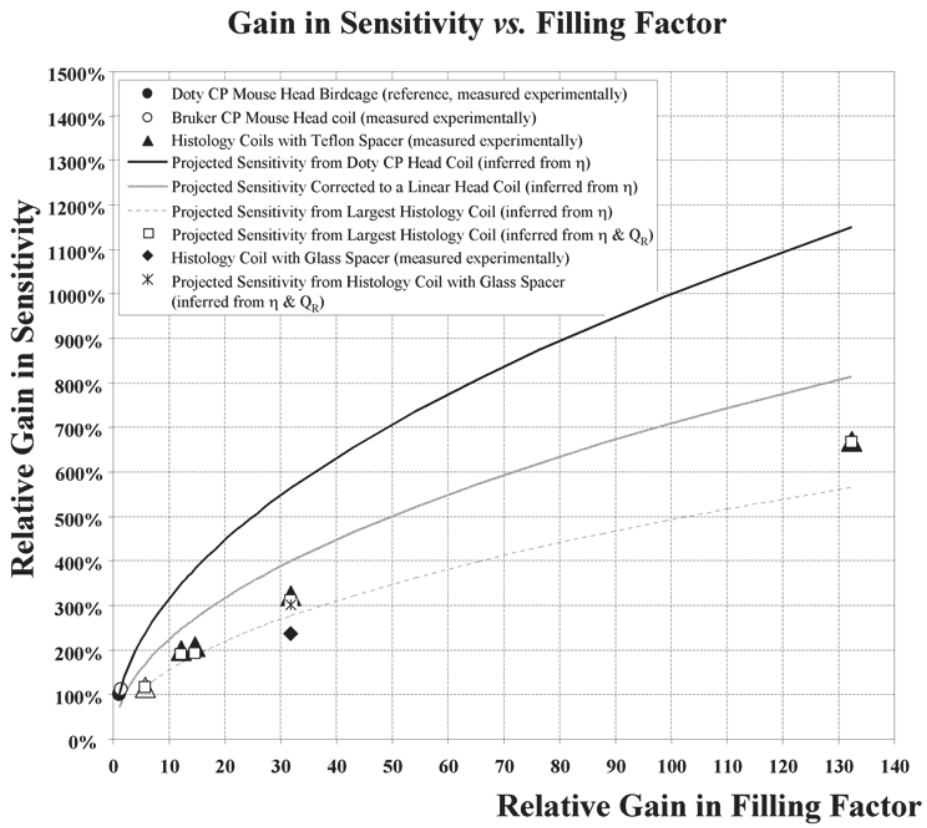

Figure IV-5: *Summary of the sensitivity of all the coils utilized in this study (Commercial Birdcage coils: open & filled circles, Histology coils: open & filled triangles and diamond) as a ratio of the effective SNR to that of a commercial mouse head RF coil used as our reference (filled circle) using the same sample for all coils. The solid black line depicts the projected increase in sensitivity of the reference CP birdcage coil that would result from the gain in filling factor achievable by the various RF histology coil using equation 1 (here Q is unaccounted for). The grey line is the sensitivity scaled down by 1.4 in the case of a linear birdcage coil structure. The difference between the grey line and triangles illustrates the systematic underperformance of the histology coils by a factor up to 1.4 fold compared to the linear birdcage coil structure. Similarly the dashed line plot was inferred using the measured sensitivity of the largest histology coil (open triangle) as the baseline. All lines were calculated with the assumption that the effect of the Q factor remained unchanged. The dashed line curve showed also a deviation from the measured values (triangles) but this time the flat histology coil structures exhibited improved performance as the measured Q increased as their size decreased. Using equation of sensitivity in chapter I (eq. I-2), this difference was accounted for by incorporating the relative experimentally-measured Q_R, resulting in values (open squares) in good agreement with measured SNR (open and filled triangles). The substitution of the Teflon spacer by a three-layer glass insert while maintaining the identical filling factor resulted in a 26% measured loss of relative sensitivity (filled diamond). However, the corresponding Q factor relative to the Teflon spacer exhibited only a 6% decrease that should lead to only a 3% drop (star) according to Equation 1 leaving 23% loss unaccounted for. In contrast the replacement of the Teflon with an air gap insert led to a negligible change (not shown).*

In comparison, the experimental measurement of the Bruker head coil demonstrated ~10% better performance (open circle) than expected due to its slightly smaller size. When examining the largest histology coil (W=52 mm, IL=24 mm, H= 1350 μm), a structure that can accommodate a glass histology slide with the widest RF coverage, the resulting sensitivity measured experimentally (SNRR ~117%, open triangle) underperformed by nearly twofold relative to the performance expected by the quadrature coil (SNRR ~238%, black line). This sensitivity loss amounts to ~1.4 than what was expected (SNRR ~170%, grey line) when accounting the linear nature of the histology resonator based on a corresponding ~5.63×ηR improvement. Similarly, the rest of the histology coils underperformed in a comparable fashion by a 1.77 factor in sensitivity (closed triangle) relative to the projected gain in filling factor for the quadrature coil (black curve) and by 1.26 when correcting for the linear detection outlined by the grey curve. The dashed line projects the theoretical sensitivity that would be gained by the largest histology coil (open triangle) when varying the gain in filling factor within the same range. Since this theoretical curve takes into account the electric loss inherent to the largest histology coil, the resulting improved performance measured with smaller structures reflects the expected decrease in losses as the coil size is reduced. This improvement is reinforced by the observed improvement of the Q factor measurements summarized in Figure IV-4 as the coil size is decreased.

These Q measurements were also accounted for in Figure IV-5 using I-2 by combining the contributions from both the sensitivity inferred from the η_R (dashed line) and the corresponding Q_R measured for each coil and outlined in Figure IV-4. The Q_R–corrected sensitivity (open squares) demonstrated a close match with the measured experimental values for each histology coil (open and filled triangles).

To assess the role of the spacer and its effect on the performance of the coils, the layered Teflon insert (measured dielectric constant $\varepsilon \approx 1.78$) was replaced with a three-coverglass-stacked insulator (measured $\varepsilon \approx 2.69$) for the medium histology coil (W=26-mm, IL=24-mm, OL=48-mm). This latter coil is similar in size to the one initially designed by Meadowcroft et al. [35] and dedicated to samples encased between two coverslips. This substitution resulted in a 26% relative loss in the measured sensitivity - decreasing from

321% for the Teflon spacer (Figure 4, filled triangle) to 238% for the glass spacer (filled diamond). This substantial loss cannot be explained solely by the alteration of their quality factor ratio Q_L(Glass spacer)/Q_L(Teflon spacer). Using equation I-2, this Q_R decrease would have led to a marginal 3% reduction in sensitivity relative to the Teflon-based structure (Figure IV-5, star), leaving a 23% loss unaccounted for. In contrast, the replacement of the spacer with an air gap interface unexpectedly resulted in a similar performance to the Teflon-based spacer (data not shown).

VIII.3. Examples of near perfect correlation: Histology MRI - Optical imaging

Examples of MRI data acquired with our various RF histology coils and thin mouse and human tissue sections that perfectly matched with their corresponding light microscopic images are shown in Figures IV-6 to 8. The sensitivity of the medium size histology coil (W=26 mm, IL=24 mm, OL=48 mm, H=450 μm) was exemplified by the acquisition of images with 50 μm in-plane resolution from 60 μm thick tissue sections of freshly excised mouse brain and kidney using a less than 6-hour imaging time (Figure IV-6).

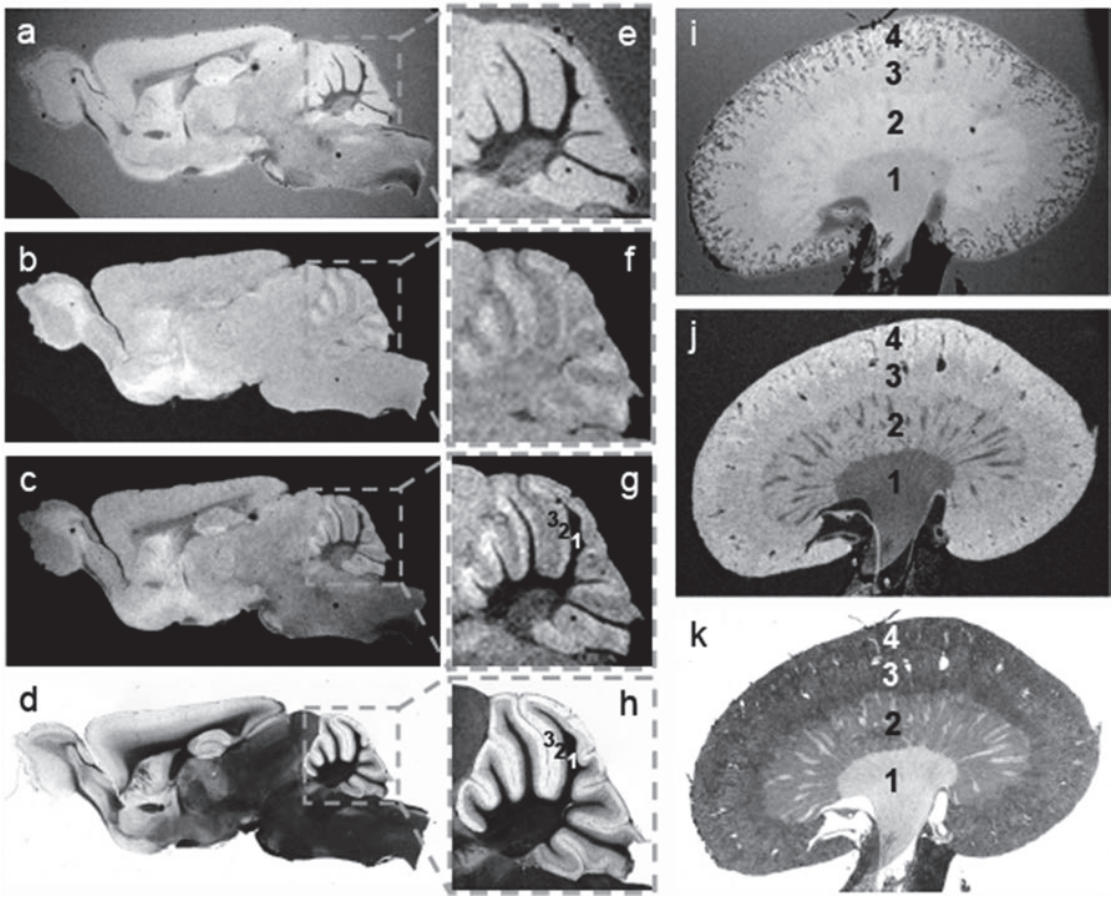

Figure IV-6: *Examples of T2*-weighted (a) and T1 weighted (b) images from 60 µm mid-sagittal section of a whole brain obtained from a wild type mouse were acquired with the medium size histology coil (W=26 mm, IL=24 mm, OL=48 mm, H=450 µm). Each image contrast was acquired with a 50 µm in-plane resolution image in less than 6 hours (totaling 12 hours). The overlaying of both MRI contrast (c) help identify some of the anatomical details seen with the near perfectly matched light microscopy (d). This can be better appreciated with the boxed view at the cerebellar level respectively (e, f, g, h) in which the various cell layers (1: Cerebellar white matter, 2: Molecular cell layer and 3: Granular cell layer) are better seen when combining T2*- and T1-weighting contrast. The same procedure was repeated for a 60 µm mouse kidney sample using both a T2*-weighted (i) and a T1-weighted (j) contrast where the main anatomical areas of this organ can be identified (1: Pelvis, 2: Medulla, 3: Cortex and 4: Capsule) and perfectly co-registered with histology (k).*

The smallest and most sensitive dual-coverslip histology coil (W=12 mm, IL=12 mm, OL=24 mm, H=450 µm) can accommodate tissue portions or small organs to give the highest anatomical detail as illustrated in Figure IV-7. The examples shown in (a) and (b) correspond to T2*-weighted and T1-weighted images from a excised 60 µm mouse

olfactory bulb mounted on dual coverslips, respectively. These results convincingly matched with their corresponding light microscopic images (c). Highly detailed coronal mouse brain sections (50μm in-plane resolution) were also observed using a 60 μm thick section acquired in less than 12 hours as shown in (d) T2*- and (e) T1-weighted scans. This also was in perfect alignment with (f) light microscopic imaging.

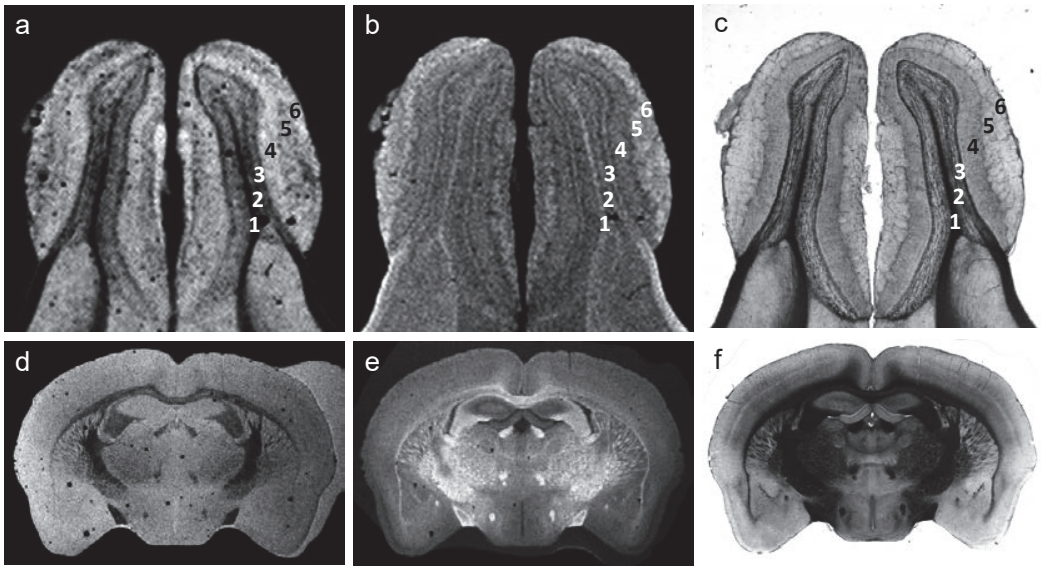

Figure IV-7: *The highly detailed image examples shown were obtained from 60 μm tissue sections using the smallest and most sensitive coverslip histology coil designed in this study (W=12 mm, IL=12 mm, OL=24 mm, H=450 μm). The first image set (a) and (b) correspond respectively to T2*-weighted and T1-weighted images with 30 μm in-plane resolution obtained from the mouse olfactory bulb co-registered with the corresponding light microscopy (c). The MRI contrast on both images helps identify the following cell layers: 1) olfactory ventricle, 2) combines the internal plexiform layer, granule cell layer and ependymal layer, 3) mitral cell layer, 4) external plexiform layer, 5) glomerular layer, 6) olfactory nerve layer. The coil can also accommodate coronal mouse brain sections depicted by the example of a 50μm in-plane MRI showing clearly the white matter track and different small tissue structures in (d) T2*- and (e) T1-weighted images in perfect alignment with (f) histology.*

The largest coils designed in this study (W=52 mm, IL=24 mm, OL=48 mm) could be used for high throughput acquisitions by scanning multiple sections at once (a-f) or to image large sized tissue (g-h). When imaging conventional pre-mounted tissues on glass slides, sections occupying a large area (up to 30 mm wide), required an opening nearly three times the size (H=1350 μm) as that needed for the dual-coverslip setup (H=450 μm). This widening translated into a three-fold reduction in the filling factor (η) resulting

in 57% effective coil sensitivity depicted by the comparison between both coils using the same sample (Figure IV-8, a & b).

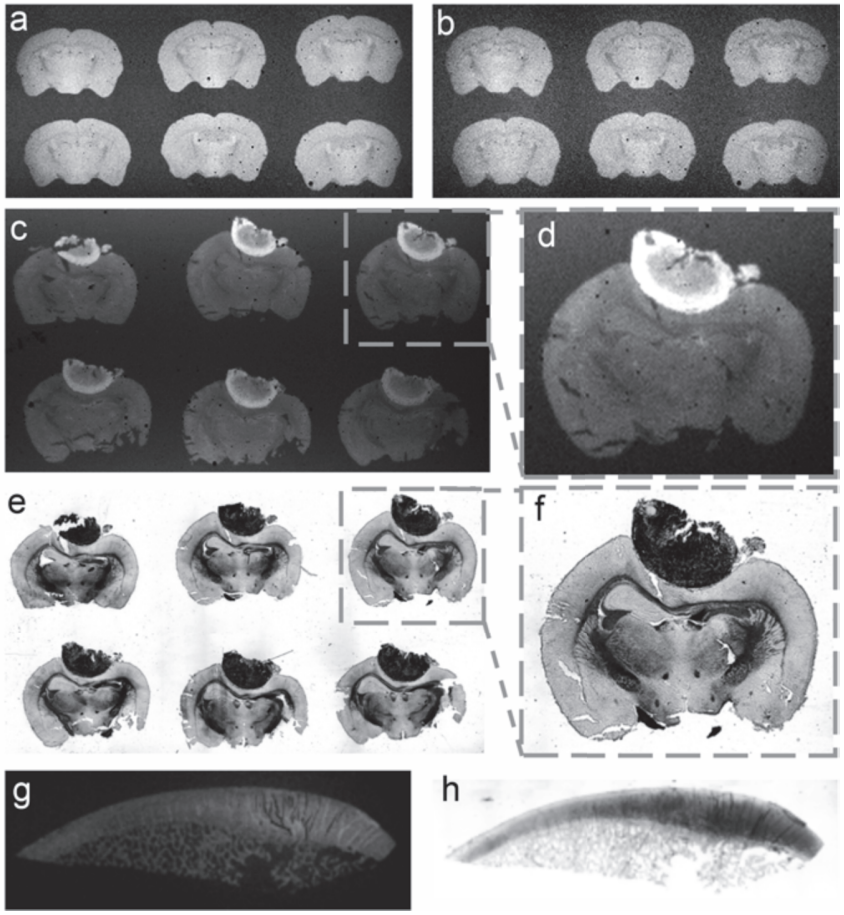

Figure IV-8: *Both large coverslip and glass-slide coils can be used for high throughput acquisitions by scanning simultaneously multiple tissue sections (a-f). This setup can also accommodate large size samples (g-h). The difference in SNR between T2*-weighted brain images acquired in (a) SNR=47 and (b) SNR=28 illustrates the 3′ greater filling factor of the dual coverslip coil (W=52 mm, IL=24 mm, OL=48 mm, H=450 µm) compared to the identical structure but capable of housing samples embedded in traditional coverslip/glass slide setup that are much thicker (coil with equal dimensions but H=1350-µm). The example shown in (c) depicts the T1-brightening of a melanoma tumor in a set of 6 × 40 µm mouse brain sections pre-mounted in a glass slide and acquired with a 60-µm in-plane resolution where (d) corresponds to a magnification of the boxed area in (c) and (e and f) the matched histology. The image example in g) corresponds to a 100µm in-plane gradient echo image of a 5 µm human trochlear cartilage (SNR=33 for an 8 h scanning time) and h) histology of the same sample using Alcian blue dye to stain glycosaminoglycans and help identify the loss of in cartilage integrity highlighted by the contrast from both imaging modality depicted by the arrows in g & h.*

IX. Discussion

Despite the simplicity of our in-house slide coil design, its construction required extra precautions due to the close proximity of the sample to the surface of the copper strip. Specifically, the presence of defects within the conducting tape was visible in the MRI images as field distortions or signal voids. Our successful designs, reflected by the excellent RF homogeneity shown in figure IV-3, were achieved by preventing the formation of air bubble traps or the presence of unwanted impurities. The incorporation of an interchangeable T/M circuit was easy to use and exceptionally cost-effective, yet consistently resulted in very reproducible performance.

The sample preparation was crucial to obtaining artifact free MR images. Both tissue rehydration and degassing was key - especially for previously mounted samples subjected to unknown conditions. In contrast, freshly excised tissue provided the opportunity to better control the sample preparation and to achieve the greatest MRI sensitivity and the best η conditions when two coverslips were used for the setup. Importantly, the dual-coverslip design demonstrated a 1.7 gain in sensitivity under equal coil dimensions at the cost of a narrower opening preventing the insertion of glass slides as outlined in Figure IV-3 and illustrated by the examples in Figure IV-8, a and b.

The largest planar shaped structure constructed (W=52 mm, IL=24 mm) showed an unprecedented homogeneous RF geometric ratio combining a thin RF layer confined within a 450-□m opening while laterally spreading over a very large width – up to ~115 times greater than its thickness. This translated into a planar RF coverage of nearly twice the size of the largest dimensions of our mouse head reference coil (ID=28 mm, L=29 mm) yet providing comparable sensitivity. The relatively small size of all the samples examined led to negligible loading effects reflected by the unaffected Q factors for all of the probes but the smallest histology coil in Figure IV-4. The loading effect measurable in the smallest histology antenna (W=12 mm, IL=12 mm) can be explained by the sample volume becoming non-negligible relative to the size of the RF resonator. This allowed for a significant gain in ηR (higher than 4 fold) relative to the nearest coil size design (medium coil: W=26-mm, IL=24-mm). Despite being only linear in polarization, the

considerable η_R increase (higher than 132 fold factor) achieved by the histology probe resulted in an exceptional 6.7 gain in sensitivity relative to the whole mouse CP reference head coil. This would translate into a 9.4 gain in sensitivity compared to a linear birdcage mouse head coil. In comparison, the study performed by Nabuurs et al. [34] at 400MHz reported a 3.8 fold gain in sensitivity when inserting a self-resonant squared loop (15×15 mm2) inductively coupled within a linear mouse head coil (accessible ID=25-mm, L not reported) that we assume is approximately similar in size to our reference coil.

Our smallest histology probe exceeded the sensitivity of a commercially available mouse head two-channel phased surface array coil by a 3.3 fold. In contrast, a superconducting replica of the structure commercially available by the same manufacturer (Bruker) was reported to outperform by only a factor ranging from 1.9 to 2.5 relative to its copper room temperature counterpart depending on the operating Larmor frequency [50-54].

The RF sensitivity factor S_{RF}, which combines both η and Q proved to be reliably predictive of the SNR when accounting for the changes in coil dimensions among the histology coils designed for this study. This was illustrated in Figure IV-5 by the negligible deviations between the effective sensitivity of each coil measured experimentally (triangle plots) and the Q_R–corrected performance inferred from the gain in η (square plots). It must be noted that this was only observed when these structures were identical both in design and components.

In contrast, the same S_{RF} equation (eq. I-2) failed to predict the difference in performance between the commercial volume coils and the histology coils, even when accounting for quadrature vs. linear polarization by dividing the commercial coil results and extrapolations by 1.4. Based on the projected gain in η_R, a systematic difference in performance (up to 1.4 fold) was observed between the sensitivity inferred from the mouse head birdcage (Figure IV-5, grey line plot) and the one effectively measured in each homemade coil (Figure IV-5, triangle plot). Importantly, this difference only marginally translated into changes in their corresponding Q factors and may partly reflect the deviation of the current via the spacer inherent to this capacitor-like structure. This

was further investigated by replacing the Teflon spacer with a glass substrate for the same histology probe. Despite the 26% experimental SNR loss observed by this substitution (difference between triangle and diamond in Figure IV-5) only a 3% deviation was predicted by the measured change of the Q_{Glass} factor. Notably, a residual 23% deviation remained unaccounted for by the S_{RF} equation. The relatively low performance of the glass-filled coil might be attributed to larger current deviated through the glass substrate resulting in less current flowing around the imaging compartment. Unlike in the sample compartment where the electrical properties are imposed by the nature of the tissue and the encasing, we investigated the possible improvement that may be achieved within the spacer compartment. Ideally, the layered Teflon spacer (dielectric constant measured $\varepsilon \approx 1.78$) could be replaced by an air-based insert ($\varepsilon = 1$) as a potential solution to substantially reduce the spacer-driven current deviation. Instead, this was practically implemented by incorporating an air-gap spacer that we predicted would mimic the dielectric properties of vacuum ($\varepsilon \approx 1$). Our results were comparable to the performance of the Teflon spacer (data now shown). This may suggest a practical difficulty in controlling ε_{air} that may be subject to fluctuations in air composition. These findings exhibit the practical utility of the Teflon spacer initially suggested by Meadowcroft et *al.* [35] as a robust insulator. In this type of configuration where a spacer is required to obtain a wide RF homogeneity, Teflon will help reduce electric losses while preventing eventual dielectric fluctuations that may occur irrespective of the experimental conditions.

X. Conclusion

Our results demonstrate that the flat coils designed for this study are unique structures for the direct imaging of histology slides by offering an unrivaled trade-offs between an excellent homogenous RF coverage and an optimal filling factor. The resulting geometric efficiency was important enough to prevail over the relatively reduced electrical performance inherent to the design. The considerable gain in sensitivity (up to 6.7 fold) obtained relative to any conventional CP coil allowed for the acquisition of highly resolved images using tissue section thicknesses commonly used for histology within their standard mounting. This provided the unique opportunity to obtain

unparalleled image co-registration between MRI and light microscopy that would be otherwise unachievable using conventional resonators. Our results highlight the role of the Teflon spacer as a stable insulator. Its insertion between the input port and the imaging region permitted the continuous and even distribution of the currents to insure a homogenous RF coverage of the sample. Our findings also helped assess the extent of the losses associated with the coil's electrical inefficiency unaccounted for by the equation modeling the RF sensitivity.

References

[1] A. S. Choe, Y. Gao, X. Li, B. K. Compton, I. Stepniewska, and W. A. Anderson, "Accuracy of image registration between MRI and light microscopy in the ex-vivo brain," *Magnetic Resonance Imaging,* vol. 29, pp. 683-692, 2011.

[2] M. M. Chakravarty, G. Bertrand, C. P. Hodge, A. F. Sadikot, and D. L. Collins, "The creation of a brain atlas for image guided neurosurgery using serial histological data," *Neuroimage,* vol. 30, pp. 359-76, Apr 1 2006.

[3] C. Chang and T. Jang, "Magnetic resonance microscopy of hamster olfactory bulb: a histological correlation," *Anat Rec,* vol. 242, pp. 132-5, May 1995.

[4] X. Li, T. E. Yankeelov, G. D. Rosen, J. C. Gore, and B. M. Dawant, "Enhancement of histological volumes through averaging and their use for the analysis of magnetic resonance images," *Magn Reson Imaging,* vol. 27, pp. 401-16, Apr 2009.

[5] T. Schormann, A. Dabringhaus, and K. Zilles, "Statistics of deformations in histology and application to improved alignment with MRI," *IEEE Trans Med Imaging,* vol. 14, pp. 25-35, 1995.

[6] H. Benveniste, K. Kim, L. Zhang, and G. A. Johnson, "Magnetic resonance microscopy of the C57BL mouse brain," *Neuroimage,* vol. 11, pp. 601-11, Jun 2000.

[7] G. A. Johnson, G. P. Cofer, B. Fubara, S. L. Gewalt, L. W. Hedlund, and R. R. Maronpot, "Magnetic resonance histology for morphologic phenotyping," *J Magn Reson Imaging,* vol. 16, pp. 423-9, Oct 2002.

[8] G. A. Johnson, M. B. Thompson, and B. P. Drayer, "Three-dimensional MRI microscopy of the normal rat brain," *Magn Reson Med,* vol. 4, pp. 351-65, Apr 1987.

[9] G. A. M. B. T. S. G. C. E. H. Johnson, "Nuclear Magnetic Resonance Imaging at Microscopic Resolution," *Journal of magnetic resonance,* vol. 68, pp. 129-137, 1986.

[10] Y. Ma, P. R. Hof, S. C. Grant, S. J. Blackband, R. Bennett, L. Slatest*, et al.*, "A three-dimensional digital atlas database of the adult C57BL/6J mouse brain by magnetic resonance microscopy," *Neuroscience,* vol. 135, pp. 1203-15, 2005.

[11] Y. Ma, D. Smith, P. R. Hof, B. Foerster, S. Hamilton, S. J. Blackband*, et al.*, "In Vivo 3D Digital Atlas Database of the Adult C57BL/6J Mouse Brain by Magnetic Resonance Microscopy," *Front Neuroanat,* vol. 2, p. 1, 2008.

[12] N. Wu, T. L. Peck, A. G. Webb, R. L. Magin, and J. V. Sweedler, "1H-NMR Spectroscopy on the Nanoliter Scale for Static and Online Measurements," *Analytical Chemistry,* vol. 66, pp. 3849-3857, 1994/11/01 1994.

[13] N. Wu, T. L. Peck, A. G. Webb, R. L. Magin, and J. V. Sweedler, "Nanoliter Volume Sample cells for 1H NMR: Application to Online Detection in Capillary Electrophoresis," *Journal of the American Chemical Society,* vol. 116, pp. 7929-7930, 1994/08/01 1994.

[14] D. L. Olson, M. E. Lacey, and J. V. Sweedler, "High-resolution microcoil NMR for analysis of mass-limited, nanoliter samples," *Anal Chem,* vol. 70, pp. 645-50, Feb 1 1998.

[15] T. L. Peck, R. L. Magin, and P. C. Lauterbur, "Design and analysis of microcoils for NMR microscopy," *J Magn Reson B,* vol. 108, pp. 114-24, Aug 1995.

[16] A. G. Webb and S. C. Grant, "Signal-to-noise and magnetic susceptibility trade-offs in solenoidal microcoils for NMR," *J Magn Reson B,* vol. 113, pp. 83-7, Oct 1996.
[17] J. E. Stocker, T. L. Peck, A. G. Webb, M. Feng, and R. L. Magin, "Nanoliter volume, high-resolution NMR microspectroscopy using a 60-micron planar microcoil," *IEEE Trans Biomed Eng,* vol. 44, pp. 1122-7, Nov 1997.
[18] V. Demas, A. Bernhardt, V. Malba, K. L. Adams, L. Evans, C. Harvey*, et al.*, "Electronic characterization of lithographically patterned microcoils for high sensitivity NMR detection," *J Magn Reson,* vol. 200, pp. 56-63, Sep 2009.
[19] M. E. Lacey, R. Subramanian, D. L. Olson, A. G. Webb, and J. V. Sweedler, "High-Resolution NMR Spectroscopy of Sample Volumes from 1 nL to 10 &mgr;L," *Chem Rev,* vol. 99, pp. 3133-3152, Oct 13 1999.
[20] A. G. Webb, "Radiofrequency microcoils for magnetic resonance imaging and spectroscopy," *J Magn Reson,* vol. 229, pp. 55-66, Apr 2013.
[21] J. Dauguet, T. Delzescaux, F. Conde, J. F. Mangin, N. Ayache, P. Hantraye*, et al.*, "Three-dimensional reconstruction of stained histological slices and 3D non-linear registration with in-vivo MRI for whole baboon brain," *J Neurosci Methods,* vol. 164, pp. 191-204, Aug 15 2007.
[22] J. Lebenberg, A. S. Herard, A. Dubois, J. Dauguet, V. Frouin, M. Dhenain*, et al.*, "Validation of MRI-based 3D digital atlas registration with histological and autoradiographic volumes: an anatomofunctional transgenic mouse brain imaging study," *Neuroimage,* vol. 51, pp. 1037-46, Jul 1 2010.
[23] S. Prima, S. Ourselin, and N. Ayache, "Computation of the mid-sagittal plane in 3-D brain images," *IEEE Trans Med Imaging,* vol. 21, pp. 122-38, Feb 2002.
[24] J. Yelnik, E. Bardinet, D. Dormont, G. Malandain, S. Ourselin, D. Tande*, et al.*, "A three-dimensional, histological and deformable atlas of the human basal ganglia. I. Atlas construction based on immunohistochemical and MRI data," *Neuroimage,* vol. 34, pp. 618-38, Jan 15 2007.
[25] N. A. Bock, N. Kovacevic, T. V. Lipina, J. C. Roder, S. L. Ackerman, and R. M. Henkelman, "In vivo magnetic resonance imaging and semiautomated image analysis extend the brain phenotype for cdf/cdf mice," *J Neurosci,* vol. 26, pp. 4455-9, Apr 26 2006.
[26] R. M. Henkelman, "Systems biology through mouse imaging centers: experience and new directions," *Annu Rev Biomed Eng,* vol. 12, pp. 143-66, Aug 15 2010.
[27] B. Durgun-Yucel, D. Hopwood, and A. H. Yucel, "The effects of mercaptoethanol-formaldehyde on tissue fixation and protein retention," *Histochem J,* vol. 28, pp. 375-83, May 1996.
[28] S. Tsunoda and C. J. Martin, "Lung tissue shrinkage after freeze substitution for histologic study," *Am Rev Respir Dis,* vol. 107, pp. 876-8, May 1973.
[29] H. Lum and W. Mitzner, "Effects of 10% formalin fixation on fixed lung volume and lung tissue shrinkage. A comparison of eleven laboratory species," *Am Rev Respir Dis,* vol. 132, pp. 1078-83, Nov 1985.
[30] S. Jonmarker, A. Valdman, A. Lindberg, M. Hellstrom, and L. Egevad, "Tissue shrinkage after fixation with formalin injection of prostatectomy specimens," *Virchows Arch,* vol. 449, pp. 297-301, Sep 2006.

[31] C. Blasdale, F. G. Charlton, S. C. Weatherhead, P. Ormond, and C. M. Lawrence, "Effect of tissue shrinkage on histological tumour-free margin after excision of basal cell carcinoma," *Br J Dermatol,* vol. 162, pp. 607-10, Mar 2010.
[32] A. Cutts, "Shrinkage of muscle fibres during the fixation of cadaveric tissue," *J Anat,* vol. 160, pp. 75-8, Oct 1988.
[33] H. Fukaya and C. J. Martin, "Lung tissue shrinkage for histologic preparations," *Am Rev Respir Dis,* vol. 99, pp. 946-8, Jun 1969.
[34] R. J. Nabuurs, I. Hegeman, R. Natte, S. G. van Duinen, M. A. van Buchem, L. van der Weerd*, et al.*, "High-field MRI of single histological slices using an inductively coupled, self-resonant microcoil: application to ex vivo samples of patients with Alzheimer's disease," *NMR Biomed,* vol. 24, pp. 351-7, May 2011.
[35] M. D. Meadowcroft, S. Zhang, W. Liu, B. S. Park, J. R. Connor, C. M. Collins*, et al.*, "Direct magnetic resonance imaging of histological tissue samples at 3.0T," *Magn Reson Med,* vol. 57, pp. 835-41, May 2007.
[36] M. D. Meadowcroft, J. R. Connor, M. B. Smith, and Q. X. Yang, "MRI and histological analysis of beta-amyloid plaques in both human Alzheimer's disease and APP/PS1 transgenic mice," *J Magn Reson Imaging,* vol. 29, pp. 997-1007, May 2009.
[37] P. Styles, C. A. Scott, and G. K. Radda, "A method for localizing high-resolution NMR spectra from human subjects," *Magn Reson Med,* vol. 2, pp. 402-9, Aug 1985.
[38] J. Mispelter, M. Lupu, and A. Briguet, *NMR Probeheads for biophysical and biomedical experiments*: Imperial College Press, 2006.
[39] D. I. Hoult and R. E. Richard, "The Signal-to-Noise Ratio of the Nuclear Magnetic Resonant Experiment," *Journal of magnetic resonance,* vol. 24, pp. 71-85, 1983.
[40] K. L. Kaiser, *Electromagnetic compatibility handbook*, 1 ed.: CRC Press, 2004.
[41] G. Cho, M. Shin, J. W. Jeong, J. Kim, B. Hong, J. Koo*, et al.*, "Glass tube of high dielectric constant and low dielectric loss for external electrode fluorescent lamps," *Journal of Applied Physics,* vol. 102, pp. 113307-7, 12/01/ 2007.
[42] A. Grill and V. Patel "Interaction of Hydrogen Plasma with Extreme Low-k SiCOH Dielectrics," *Journal of The Electrochemical Society,* vol. 151, pp. F133-F134, June 1, 2004 2004.
[43] Y. Lin, T. Y. Tsui, and J. J. Vlassak, "Octamethylcyclotetrasiloxane-Based, Low-Permittivity Organosilicate Coatings: Composition, Structure, and Polarizability," *Journal of The Electrochemical Society,* vol. 153, pp. F144-F152, July 1, 2006 2006.
[44] H. Kitoh, M. Muroyama, M. Sasaki, M. Iwasawa, and H. Kimura, "Formation of SiOF Films by Plasma-Enhanced Chemical Vapor Deposition Using "(C_2H_5O)_3SiF," *Japanese Journal of Applied Physics,* vol. 35, pp. 1464-1467, 1996.
[45] J. P. Reynard, C. Verove, E. Sabouret, P. Motte, B. Descouts, C. Chaton*, et al.*, "Integration of fluorine-doped silicon oxide in copper pilot line for 0.12-µm technology," *Microelectronic Engineering,* vol. 60, pp. 113-118, 1// 2002.
[46] M. Alecci, C. M. Collins, M. B. Smith, and P. Jezzard, "Radio frequency magnetic field mapping of a 3 Tesla birdcage coil: experimental and theoretical

dependence on sample properties," *Magn Reson Med,* vol. 46, pp. 379-85, Aug 2001.
[47] Y. Z. Wadghiri, E. M. Sigurdsson, M. Sadowski, J. I. Elliott, Y. Li, H. Scholtzova*, et al.*, "Detection of Alzheimer's amyloid in transgenic mice using magnetic resonance microimaging," *Magn Reson Med,* vol. 50, pp. 293-302, Aug 2003.
[48] G. E. Hoffman and W. W. Le, "Just cool it! Cryoprotectant anti-freeze in immunocytochemistry and in situ hybridization," *Peptides,* vol. 25, pp. 425-431, 2004.
[49] R. R. Ernst and W. A. Anderson, "Application of Fourier transform spectroscopy to magnetic resonance," *Rev Sci Instrum,* vol. 37, pp. 93 -102, 1966.
[50] C. Baltes, N. Radzwill, S. Bosshard, D. Marek, and M. Rudin, "Micro MRI of the mouse brain using a novel 400 MHz cryogenic quadrature RF probe," *NMR Biomed,* vol. 22, pp. 834-42, Oct 2009.
[51] J. C. Nouls, M. G. Izenson, H. P. Greeley, and G. A. Johnson, "Design of a superconducting volume coil for magnetic resonance microscopy of the mouse brain," *J Magn Reson,* vol. 191, pp. 231-8, Apr 2008.
[52] D. Ratering, C. Baltes, J. Nordmeyer-Massner, D. Marek, and M. Rudin, "Performance of a 200-MHz cryogenic RF probe designed for MRI and MRS of the murine brain," *Magn Reson Med,* vol. 59, pp. 1440-7, Jun 2008.
[53] B. Wagenhaus, A. Pohlmann, M. A. Dieringer, A. Els, H. Waiczies, S. Waiczies*, et al.*, "Functional and morphological cardiac magnetic resonance imaging of mice using a cryogenic quadrature radiofrequency coil," *PLoS One,* vol. 7, p. e42383, 2012.
[54] H. Waiczies, J. M. Millward, S. Lepore, C. Infante-Duarte, A. Pohlmann, T. Niendorf*, et al.*, "Identification of cellular infiltrates during early stages of brain inflammation with magnetic resonance microscopy," *PLoS One,* vol. 7, p. e32796, 2012.

General conclusion

In this thesis we have described our protocol to characterize available MR coils that is similar to the techniques used by coil developers include pick-up coil, measurement of quality factor, estimation of filling factor. Additionally, we also developed our own software to characterize coil homogeneity. The macro developed is simple to use and can be easily installed with NIH ImageJ software. The results generated from this software were part of our publication in the journal Magnetic Resonance in Medicine. We have continued to characterize other coils we have developed and used in our recent studies.

A fundamental characteristic of MRI that makes it widely used in biomedical research and clinical practice is its ability to visualize events *in vivo*. The use of animal models of disease allows us to test ideas that may eventually result in human application. As well as using different MRI sequences to have the desired image enhancement, contrast agents are also commonly used in MRI to target certain areas of the body and to highlight these parts in the images generated. To test the bio-distribution of contrast agents developed by our collaborators we have developed a high-pass birdcage coil to allow optimal imaging of the mouse body. The probe designed satisfied the requirement of large RF coverage and was suitable for a qualitative study.

Along with our studies on imaging the mouse body, we have also developed protocols to image smaller parts of the mouse anatomy such as the mouse brain, with a particular impassion the olfactory bulb. For small regions of interest, it's preferable to use a small coil to limit the field of view and take advantage of the filling factor. Hence, we developed a mouse head coil that is significantly smaller in size than a commercially available coil. While a gain in SNR is in the expected range, the similarity in RF field homogeneity with the commercial coil was a welcome bonus, thanks in part to the way the birdcage structure functions. This coil has been extensively utilized in all our *in vivo* imaging projects, including studying contrast agents targeting Alzheimer's disease plaques, the effect of aging on the vasculature system in mice and Manganese track tracing in the mouse olfactory bulb. The results from these studies have been presented at several conferences and published recently.

ex vivo imaging provides an intermediary step between MRI and histological analysis, allowing co-registration between the images. It has several advantages compare to *in vivo* MRI. The major advantage being the need to keeping the subject alive is no longer a requirement. Additionally, the scanning time can be extended as long as necessary and allows for higher image resolution, and higher SNR. And the fact that the subject is immobile means that the motion artifact is no longer a limitation. Because live animal needs to be surveyed and operators are needed for this purpose, we dedicated normal business hours to *in vivo* imaging. The unattended overnight period (up to 12h) can be used for *ex vivo* MRI where the operators only need to calibrate and start the scan and leave the system to complete the rest of the experiment. Our goal is to take advantage of this schedule efficiently which means to scan as many samples as possible while keeping the image quality above a minimum standard (SNR above 30). To achieve this, we first used a commercial coil to scan 4 mouse brains within 8 hours with excellent SNR and homogenous coverage. As the number of brains was increased we modified our coil structure to a form that could accommodate 8 brains at a time while insuring the image quality was unchanged for the duration of the scan time. Our newly developed dual-litzcage coil with a feeding point in the middle of the coil showed excellent homogeneity in coverage, which satisfied the requirements for the quantitative studies using SPMMouse toolbox (a voxel based comparison between groups of mice). Even though we were able to scan twice as many brains, the filling factors only decreased by 20%, therefore maintaining a high level of SNR for 8 hours scan time, and only 10% lower than a 4-brain scan with a commercial coil. In combination with a low noise figure preamp, the image quality can reach the same level as for a 4-brain scan with twice the number of samples, which results in a doubling of the overnight scan efficiency. The resulting setup greatly eased our time for sample preparation and reduced scanning time.

While *ex vivo* imaging has proven its advantages compared to *in vivo* imaging, the ability to match MRI images and histologically obtained images remains difficult. Several approaches have been attempted to obtain a direct MRI from histological tissue. All of the methods were based on improving the filling factor for a thin tissue sample while maintaining good homogeneity coverage. Our work has focused on the flat u-shaped coil structure as suggested by Meadowcroft and colleagues. This design proved to have

excellent filling factor and homogeneity to match the requirements mentioned above. However, there is no reference test to assess the performance of this coil structure. We constructed in-house a set of histology coils using the suggested design with simple materials that could be easily purchased from available distributors. The performance of this coil set was compared to two standard commercial whole mouse head coils and one commercial mouse head surface coil. Our results showed that the histology coils underperformed with respect to the gain in filling factor, even though this was corrected by the measured quality factor. This led to the conclusion that our model of filling factor and quality factor to predict coil performance, can only be used with the caveat that coils must be made of the same structure and components. The initial design recommended the use of Teflon, and this proved to be a robust material for the spacer that could prevent air composition fluctuation while maintaining a low dielectric constant. Overall, the gain in filling factor of this design helped to overcome the dielectric losses created by the capacitor like shape of the coil leading to a 6.7 fold gain in SNR compared to the whole mouse head coils. The largest coil that could accommodate a traditional histology glass slide provided a similar SNR compared to the mouse head coils but had a much wider RF homogeneity coverage.

In this thesis, we have described practical aspects to improve the development of small animal imaging protocol, especially for mouse MRI. The improvements gained in each step of our validated approach helped to save time, manpower and also improve the image quality.

Appendix

Coil homogeneity assessment through signal intensity mapping

The MR coil homogeneity mapping usually has been done by B_1 field mapping. The mapping of the magnetic field requires a lot of calculation, simulation and measurement. To ease the process of our coil characterization, we developed in-house a macro that can color map the signal intensity from any gray level image.

1. Signal intensity color-mapping using ImageJ

MRI images are acquired in gray level (2D or 3D stack usually in 16 to 32 bit). In order to compare the signal intensity of each pixel to a region of interest ROI (used as reference) and then color-coded following the range difference (for example: light green for 5% of variation, dark green for 10%, etc.…), we developed a macro that can be easily integrated with ImageJ freeware for this purpose. The principle of this macro is very simple as follow:

- Determine the ROI (automatically or manually by user)
- Calculate the mean of the signal intensity in the ROI (average of signal intensity of all the pixel inside the ROI
- Iteratively calculate the ratio between the signal intensity of each pixel and assign a color to this pixel following the range of variation.
- Created a new image (or stack) that is the color-map obtained from the previous iteration.

2. Coil homogeneity mapping using color-map macro

As mentioned previously, the homogeneity of the coil is very important because most of the errors in quantitative studies are caused by the filed inhomogeneity. The inhomogeneity of the coil might cause different signal intensities for the 2 ROIs with the same nature leads to discrepancies in quantification. Different coil structures will provide different B1 field homogeneity. For a volume coil, the reference of the signal is usually the center of the coil. A region of the coil is considered as homogeneous when the

difference of magnetic signals generated by the coil in this region is not greater than an allowed variation compared to a area of reference (usually less than 10% or 12% when compared to the center of the coil).

In this study, we will present a practical method to evaluate the homogeneity of the coil using an imaging method.

For the evaluation works accurately, the sample must fit tightly the accessible volume of the coil (diameter of the sample ideally equal to inner diameter – ID of the coil) so as to avoid space that might cause a loss of information about the homogeneity of the coil. The sample also needs to be centered in the coil:

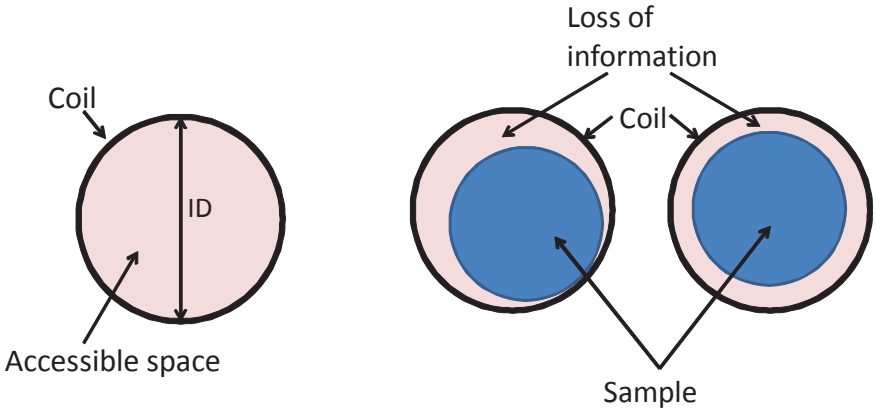

Figure 0-1: *Loss of information when sample is not well positioned in the coil*

Considering the sample is a cylindrical container filled with a homogenous liquid (oil, doped water, etc.), a 3D MRI image stack of the sample can be acquired with different sequences (Gradient Echo GE, Spin Echo SE…). Once acquired, the images can be easily visualized with ImageJ (freeware). This software is based on the Java language and also includes a Macro language. The macro language allows for the executing of almost all the existing functions pre-built into ImageJ. To evaluate the homogeneity of the coils, we used the macro described above:

- Once a stack of images (could be 2D image) is opened, the macro will
    - Check if the stack is 32bit?
    - If not, the macro will convert the stack to 32bit
    - If it is, we can continue to the next step

- On a 2D image, the macro will create a ROI of size 10x10 pixels. The user can also choose to use a self-defined ROI:

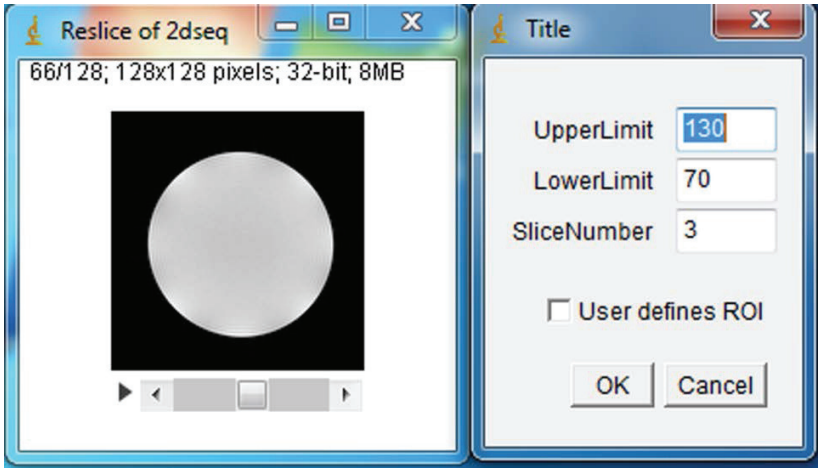

Figure 0-2: *Example of MRI of sample and ImageJ signal intensity color mapping macro*

- The macro will use a function of ImageJ to calculate the mean of the signal in the ROI.
- Then, for each pixel of the image, the signal intensity will be compared to the mean of the signal in the ROI.
- The different in signal intensity can then be converted to a percentage and each range of difference will be coded in a chosen color.
- For a 3D stack, the user can chose the number of images in the center of the stack to create a 3D ROI. The size of the ROI can be defined automatically (10x10) or user-defined. Similar to the case of a 2D image, the mean of the 3D ROI will be obtained and the signal intensity of each pixel of the stack will be compared to the mean of this ROI. Then the whole 3D volume will be color coded with respect to the difference in signal intensity.
- This macro allows a vision of the homogeneous volume of the coil and also calculates quantitatively the size of the volume (based on the number of pixels within a certain range)

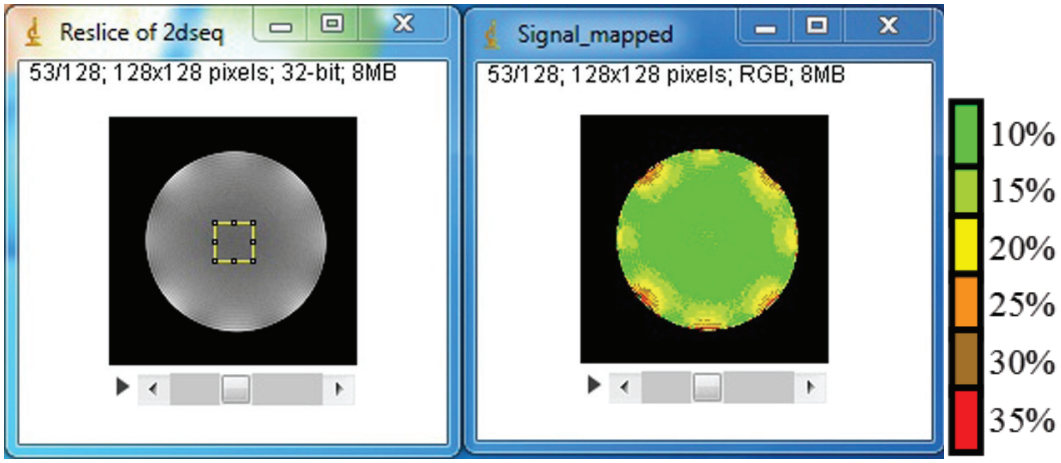

Figure 0-3: *Example of color map given by the ImageJ signal intensity color mapping macro*